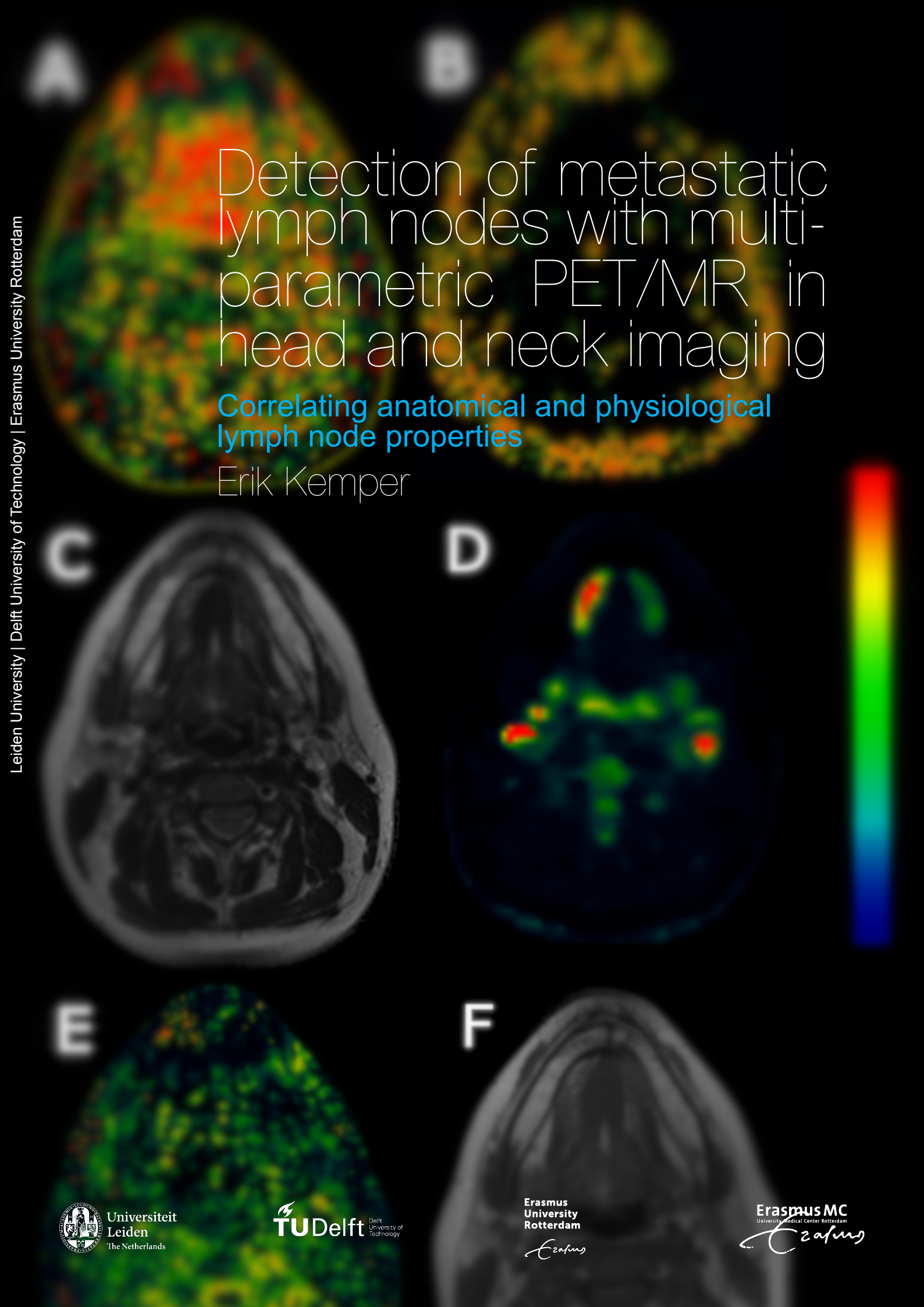

Detection of metastatic lymph nodes with multi-parametric PET/MR in head and neck imaging

Correlating anatomical and physiological lymph node properties

Erik Kemper

Leiden University | Delft University of Technology | Erasmus University Rotterdam

Universiteit Leiden The Netherlands
TU Delft Delft University of Technology
Erasmus University Rotterdam
Erasmus MC University Medical Center Rotterdam

Detection of metastatic lymph nodes with multi-parametric PET/MR in head and neck imaging

Correlating anatomical and physiological lymph node properties

Kemper, Erik

Student number: 4548221

12-01-2023

Thesis in partial fulfilment of the requirements for the joint degree of Master of Science in

Technical Medicine

Leiden University | Delft University of Technology | Erasmus University Rotterdam

Master thesis project (TM30004 : 35 ECTS)

Dept. of Radiology and Nuclear Medicine, ERASMUS MC
February 2022 – January 2023
Supervisors:
Dr. A. A. Harteveld
Prof. dr. F. A. Verburg
Ir. M. Segbers

Thesis committee members:

Prof. dr. F. A. Verburg, Erasmus MC (chair)
Dr. A. A. Harteveld, Erasmus MC
Prof. dr. ir. M. Staring, LUMC

Universiteit Leiden The Netherlands

TU Delft Delft University of Technology

Erasmus University Rotterdam

Erasmus MC University Medical Center Rotterdam

Summary

Detection of lymph node involvement has a significant negative impact on the treatment outcome for patients with head and neck squamous-cell carcinomas (SCC). Metastatic lymph nodes can be detected with high sensitivity by ^{18}F-fluorodeoxyglucose (^{18}F-FDG) positron emission tomography (PET). However, ^{18}F-FDG uptake is not only increased in metastasis. For example, inflammation in irradiated regions have increased ^{18}F-FDG uptake obscuring possible residual tumour. Additional imaging might improve the specificity of the ^{18}F-FDG PET images.

Magnetic resonance imaging (MRI) is currently used in head and neck imaging to provide anatomical reference for the ^{18}F-FDG PET. However, early detection of metastatic lymph nodes based on anatomical MRI is difficult. Physiological MRI uses sequences that allow for the measurement of physiological processes within a tissue. Changes of these physiological processes within lymph nodes might indicate a metastasis. Two types of physiological MRI were of interest for this study, diffusion weighted imaging-intravoxel incoherent motion (DWI-IVIM) and dynamic contrast enhanced (DCE)-MRI. Quantified data from these physiological MRI acquisition might provided added predictive value in head and neck PET/MR for the detection of metastatic SCCs lymph nodes.

Optimisation of the physiological MRI sequences was required since the DWI-IVIM and DCE-MRI were not previously preformed for head and neck on the PET/MR system at the Erasmus Medical Centre. Based on the profiles from the Quantitative Imaging Biomarkers Alliance the DWI-IVIM and DCE-MRI sequences have been optimised. The final DWI-IVIM and DCE-MRI sequence parameters were an optimal balance for sufficient image signal of lymph nodes and practical scan time for the study.

For the prospective study, subjects were included between September and December 2022 scheduled for a standard diagnostic PET/MR exam of the head and neck region with (suspected) SCC. The DWI-IVIM and DCE-MRI sequences were additionally acquired during the standard diagnostic PET/MR. Lymph nodes identified by an experienced radiologist or nuclear medicine physician were included for processing and analysis. Metastatic lymph nodes were determined based on the pathology results. Each included lymph was described non-suspect, suspect or pathological based on the standard PET/MR images.

Masks of only the lymph node region of interests were used for processing of the DWI-IVIM and DCE-MRI images. From the DWI-IVIM model diffusion D and pseudodiffusion D^* were calculated. Quantitative permeability parameters for DCE-MRI were modelled with the extended Tofts pharmacokinetic model. The outcome measures included permeability K^{trans}, K_{ep} and volume fraction V_p. Descriptive parameters were calculated for each lymph node from each quantitative parameter map.

In total 14 subjects were scanned with the additional physiological MRI sequences, of which ten were included with 41 analysed lymph nodes. Pathology was acquired for 13 lymph nodes, three malignant and ten non-malignant. Significant differences were found between the malignant and non-malignant lymph nodes for quantitative parameters of DWI-IVIM D, DWI-IVIM D^*, ^{18}F-FDG SUV, DCE-MRI K^{trans} and DCE-MRI K_{ep}. Furthermore, six of the ten non-malignant lymph nodes were suspected based on the standard PET/MR images.

The physiological MRI showed multiple quantitative parameters correlating to malignancy. Moreover, the relatively high number of suspected non-malignant lymph nodes depicts the potential specificity improvement physiological MRI can provide for head and neck PET/MR imaging. However, a larger database of analysed lymph nodes is required to determine more concrete correlations.

Contents

List of abbreviations **iv**

1 Introduction **1**

2 MRI optimisation **4**
2.1 Methods . . . 4
2.1.1 DWI-IVIM . . . 5
2.1.2 DCE-MRI . . . 6
2.2 Results . . . 7
2.3 Discussion . . . 8

3 H&M study **10**
3.1 Methods . . . 10
3.1.1 Patient population . . . 10
3.1.2 Image acquisition . . . 10
3.1.3 Lymph node selection . . . 11
3.1.4 Processing . . . 11
3.1.5 Analysis . . . 15
3.2 Results . . . 16
3.2.1 Quantitative PET/MR measurements . . . 17
3.2.2 PET/MR image findings . . . 17
3.2.3 Classification by multiparametric PET/MR . . . 19
3.3 Discussion . . . 19

A PET and multiparametric MRI for Head and Neck Cancer, Literature review **30**

B Supplementary Tables and Figures **28**

List of abbreviations

Notation	Description
^{18}F-FDG	^{18}F-fluorodeoxyglucose.
A/P	anterior/posterior.
AC	attenuation correction.
ADC	apparent diffusion coefficient.
AIF	arterial input function.
CT	computed tomography.
DCE-MRI	dynamic contrast enhanced-MRI.
DISCO	differential sub-sampling with Cartesian ordering.
DWI	diffusion weighted imaging.
DWI-IVIM	DWI-Intravoxel incoherent motion.
EES	extravascular-extracellular space.
FA	flip angle.
FNAC	fine needle aspiration cytology.
FOV	field-of-View.
FRFSE	fast relaxation fast spin echo.
FSE	fast spin echo.
FSL	Functional Magnetic Resonance Imaging of the Brain software library.
Gd	gadolinium.
HNC	head and neck cancer.
IDEAL	iterative decomposition of water and fat with echo asymmetry and least-squares estimation.
KNN	K-Nearest Neighbour.
MRI	magnetic resonance imaging.
NEX	number of excitations.
PET	positron emission tomography.
QIBA	Quantitative Imaging Biomarkers Alliance.
ROI	region of interest.
SCC	squamous-cell carcinoma.
SE-EPI	single-shot spin-echo echo-planar imaging.
SLNB	sentinel lymph node biopsy.
SNR	Signal-to-Noise Ratio.
T_1w	T_1-weighted.
T_2w	T_2-weighted.
TE	echo time.
TR	repetition time.
VFA	variable flip angle.

1

Introduction

Approximately 900.000 new cases and 450.000 deaths are described annually worldwide for head and neck cancers (HNCs) [1]. Four percent of all new cancer cases in Europe are HNC [2]. Treatment of a head or neck squamous-cell carcinoma (SCC) at an early stage by surgery, radiotherapy or both has a high curement rate. However, only 30% to 40% of patients present with an early stage I or II cancer [3]. Late stage III or IV tumours are associated with lymph node involvement or distant metastasis negatively impacting the prognosis. Lymph node metastasis significantly increase chances of recurrence. Whereas, distant metastasis lower the 5-year overall survival of SCCs to <50% [4]. Lymph node metastases are described as one of the main prognostic factors for head and neck tumour progression, especially after dissection of the tumour [5]. Therefore, accurate identification of possible metastatic lymph nodes is of high importance to determine the tumour stage and treatment planning.

Several techniques are available for detection of metastatic lymph nodes. These include imaging, cytology, biopsy, and dissection. The first step in the diagnostic work-up to determine the extent of HNC is often ^{18}F-fluorodeoxyglucose (^{18}F-FDG) positron emission tomography (PET) imaging. A high sensitivity is achieved by PET ^{18}F-FDG imaging for metastatic lymph node detection [6, 7]. However, false-positive metastatic lymph nodes occur relatively often. Not all lymph nodes with an increased ^{18}F-FDG uptake are metastatic. For example, inflammation can cause an increase in ^{18}F-FDG uptake not related to tumour cells [8]. To increase the specificity of ^{18}F-FDG PET imaging, additional computed tomography (CT), magnetic resonance imaging (MRI), ultrasound guided fine needle aspiration cytology (FNAC), neck dissection or sentinel lymph node biopsy (SLNB) can be performed on the PET ^{18}F-FDG suspected nodes.

SLNB is recently verified for clinical use in HNC [9, 10]. SLNB assumes a predictable drainage of tumour cells through the lymphatic system. Thus, when no tumour cells are found in the sentinel node, the HNC has probably not yet spread from its primary location. The lymph node metastasis status could be determined with the sentinel node in >95% of cases [11, 12]. Overall, a sensitivity of 82,7 % and specificity of 98,1 % has been found for detection of metastatic sentinel lymph nodes using SLNB [13]. Neck dissection (elective) is not performed for diagnosis of HNC, it is a HNC treatment. However, pathology is performed on the dissected tissue for verification. If lymph node metastasis have been found or a high suspicion exists for local infiltration of the tumour exists, neck dissection of unilateral or bilateral lymph node levels can be performed. Lymph nodes are dissected by neck level as depicted in Figure 1.1a. Pathology of the dissected lymph nodes will determine the presence of tumour in the nodes and possible unclean excisions of the tumour or lymph nodes. Incorrect conclusions of the lymph nodes status by pathology for HNC are made in approximately 2-3% of cases [14].

A less invasive method to determine the status of suspected nodes is FNAC. The sensitivity and specificity of FNAC for detection of metastatic lymph nodes has been found to be 94,2 % and 96,9% before treatment and reduces to 69,1 % and 84,2 % respectively for recurrent or persistent metastatic regional head and neck cancers [17, 18]. Thus, the combination of imaging and cytology, biopsy or dissection provides a relatively high diagnostic accuracy in detecting the presence and number of lymph node

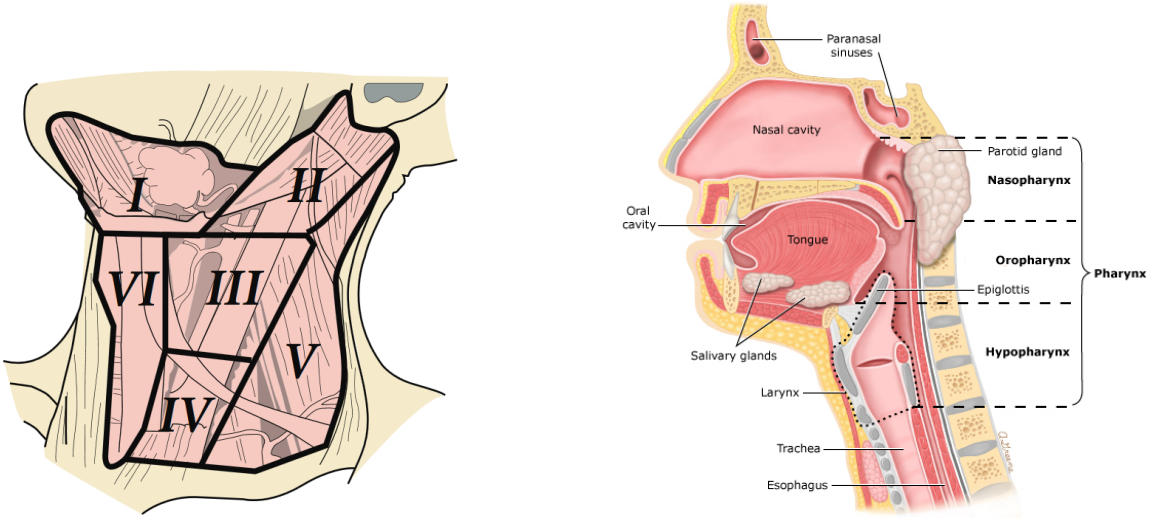

(a) **(b)**

Figure 1.1. Anatomical categorisations in head and neck cancers. ***(a)*** **Anatomical grouping of lymph nodes in the neck by levels: Level I, submental and submandibular group; Level II, upper jugular group; Level III, middle jugular group; Level IV, lower jugular group; Level V, posterior triangle group; Level VI, anterior compartment. Adapted from: Deschler Daniel G, Moore Michael G, and Smith Richard V [15]*** *(b)* **Anatomy of the head and neck. Adapted from: Overview of the diagnosis and staging of head and neck cancer (2022). UpToDate ®[16].**

metastasis. However, they are invasive methods and cytology and biopsy have the associated risk of seeding the punctured tumour tissue [19]. Furthermore, accuracy significantly decreases for recurring tumours.

Additional imaging can provide a non-invasive alternative to FNAC or SLNB, improving the specificity in metastatic lymph node detection of the PET ^{18}F-FDG. Fused PET with CT imaging is commonly used to aid the detection of metastatic lymph nodes. The CT imaging provides anatomical information and localisation of the regions with high ^{18}F-FDG uptake. Basic characteristics of the lymph node can be described by the CT [20]. However, lymph nodes mainly reside in body fat and soft tissue regions. Thus, limited contrast between a lymph node and its surroundings is provided by the CT. Anatomical MRI, such as T_1-weighted (T_1w) or T_2-weighted (T_2w) imaging, have shown to provide a similar diagnostic accuracy combined with PET as PET-CT in the detection of metastatic lymph nodes [21, 22, 23]. The soft tissue contrast of the different MRI sequences provides sufficient contrast to visualise individual lymph nodes within the head and neck region. Unfortunately, with the visualisation of lymph nodes, early detection of metastasis is difficult. Enlarged size, rounded shape and the presence of necrosis are clear indications of metastatic lymph node and are visible on MRI. However, these features only become apparent at a much later stage of the metastatic development. Some metastatic lymph nodes do not even show these features. Additional information of mainly small lymph nodes which are suspected for metastasis based on the PET ^{18}F-FDG would be beneficial.

The use of physiological MRI sequences may provide this missing information. Physiological MRI sequences use techniques that allow for the measurement of physiological processes within a tissue. Most physiological MRI sequences have an origin in brain imaging, but their use is spreading to other disciplines. For HNC the application of physiological MRI is still limited. In HNC, diffusion weighted imaging (DWI) and dynamic contrast enhanced-MRI (DCE-MRI) have been investigated most often.

The DWI acquisition standard used in clinical practice calculates an apparent diffusion coefficient (ADC) which represents an approximation of the diffusion in the tissue. Other processes, such as the microcirculation of a tissue influence the ADC. DWI-Intravoxel incoherent motion (DWI-IVIM) tries to minimise the effect of other processes, resulting in a diffusion measure which should better represent the actual tissue diffusion. DCE-MRI is a dynamically acquired T_1w imaging during contrast injection. From the

contrast curve over time measured on the MR images various quantitative permeability parameters can be calculated.

Detection of HNC using DWI(-IVIM) and DCE-MRI have been shown. [24, 21, 22, 25, 26, 27, 28, 29]. Distinctions between normal and malignant tissue could be made by multiple DWI-IVIM and DCE-MRI quantitative parameters. Also, differentiation of malignancy from inflammation has been found to be possible by both DWI-IVIM and DCE-MRI parameters, indicating a clear opportunity for possible improvement in the detection of metastatic lymph nodes in addition to PET ^{18}F-FDG [30, 31, 32, 33, 33].

Not all performed studies detecting metastatic lymph nodes in HNC patients have described the same results. Multiple studies have found no correlations between DWI(-IVIM), DCE-MRI and HNC. Furthermore, most studies have used relatively small study populations providing limited evidence. The imaging for studies correlating ^{18}F-FDG and physiological MRI to HNC were mainly acquired on a dedicated PET-CT and MRI scanner. Which required registration of the images to determine the combined PET and MRI values. Accurate registration of the head and neck MRI and PET images is challenging because of the non-rigidity of the neck. Integrated PET/MR imaging reduces the amount of motion possible between PET and MRI acquisitions. Thereby, the amount of registration required is limited, improving the fusion of the different acquisitions. Especially, for small lymph nodes, accurate fusion of the images is essential to be able to accurately determine the quantitative parameters within the lymph nodes.

Therefore, the purpose of this study was to determine the added predictive value of quantitative physiological MRI in head and neck PET/MR for the detection of metastatic SCCs lymph nodes.

2

MRI optimisation

MRI provides a wide variety of options and parameters to alter the imaging sequence and improve the output images. Inherent to the MRI is the non quantitative character of the signal intensities from a certain tissue [34]. This is caused by multiple factors such as inhomogeneities in the magnetic field or slight inaccuracies in the pulse sequence performance. Each MRI system provides slight variations in imaging results of the same subject and even over time within one system. Therefore, sequence parameters used at one MRI system will not produce identical output images on another system. Optimisation of an MRI sequence is required to achieve optimal results for a specific MRI sequence and MRI system combination. The DWI-IVIM and DCE-MRI sequences used in this study, were not previously preformed on the 3T Signa PET/MR system (GE Healthcare. Illinois, USA) at the Erasmus Medical Centre. The purpose of the MRI optimisation was to tailor the DWI-IVIM and DCE-MRI sequences on this system for head and neck lymph node imaging and ensure sufficient image quality for usability in the patient study.

2.1. Methods

Optimisation was performed on the DWI-IVIM and DCE-MRI sequences. Those were the physiological MRI sequences of interest in the patient study. The DWI-IVIM and DCE-MRI sequences needed to be optimised for application in the head and neck region. Specifically, to provide optimal imaging of lymph nodes within this region. Of course, extremely long and extensive protocols will provide the best imaging results. However, when imaging patients a compromise needs to be found between image quality and patient comfort. Often head and neck cancer patients already undergo multiple lengthy imaging exams, such as the PET/MR imaging. Therefore, each minute spend imaging should be defensible with a clinically relevant increase in imaging quality.

To achieve this balance, several main factors for optimisation have been selected. These included: spatial and temporal resolution, repetition time (TR), echo time (TE), number of excitations (NEX), overall scanning time, field-of-View (FOV), Signal-to-Noise Ratio (SNR), the number of artefacts in the image and goodness of fit of the DWI and DCE-MRI parameters. For each MRI sequence specific goals were defined for the factors based on the related Quantitative Imaging Biomarkers Alliance (QIBA) profile or similarly performed imaging described in literature.

Multiple healthy volunteers were scanned on the PET/MR system to alter and improve the initial imaging parameters of the DCE and DWI sequences. Before each scan session possible alterations of the current MRI sequence were selected based on similar sequences found in literature and the ideal parameter values as described above. After each scan session image quality of each alteration of the sequence was determined and compared with the other alterations and earlier imaging. Further iterations of the parameters were performed on the best performing sequence. The selection of the final set of parameters was done considering all imaging quality measures and the specific goal of imaging lymph nodes.

Considerations of scan parameters that were optimised for the DCE-MRI and DWI-IVIM sequences are

described in the next paragraphs.

2.1.1. DWI-IVIM

DWI-IVIM is a bi-exponential decay quantification method of DWI. For the calculation of the ADC a DWI is acquired at two or three different diffusion gradient settings. By acquiring DWI at additional diffusion gradient settings a finer model can calculated to differentiate actual tissue diffusion from microcirculation. The result is a diffusion parameter D and a pseudodiffusion parameter D^* representing the microcirculation of the tissue. Additional details on the DWI-IVIM sequences can be found in Appendix A

DWI has been part of the head and neck diagnostic MRI protocol at the Erasmus MC in the past. However, the DWI images were only limited consulted in the evaluation of head and neck tumours. Therefore, DWI was at some point removed from the diagnostic scan protocol. In recent work of N. Sijtsema et al.[cite] DWI-IVIM in the head and neck region has been tested. This study sought to find the optimal b-values for measuring IVIM in the head and neck region. The results from this study formed the bases for optimisation of the DWI-IVIM sequence on the PET-MRI system.

Optimisation of DWI-IVIM was focused on the following scan parameters: slice thickness, TR, TE, NEX, FOV and scan time (see Table 2.1). The parameter values were based on the QIBA DWI profile of the brain [35], since no specific head and neck profile has been determined. Therefore, additional considerations have been made to specify the parameter settings for the research purpose of imaging head and neck lymph nodes.

Slice thickness

Currently in clinical practice, prediction of metastatic involvement in lymph nodes is mainly based on lymph node size. Measurement of the lymph node size can be done in multiple ways. The axial short-axis diameter of the node is commonly used to determine lymph node size. A lymph node is suspect with a diameter of ≥10 mm for neck lymph nodes or ≥5mm for retropharyngeal located lymph nodes [36, 37, 38]. A slice thickness of 5-7 mm should provide enough resolution to image the enlarged lymph node. However, smaller lymph nodes in the range of 5 mm will be partially covered by the voxel. Thereby only limited voxels will contain exclusively lymph node data. Ideally a thickness of less than 5 mm would be beneficial to increase the amount of lymph node specific data points for both enlarged and normal sized lymph nodes. SNR needs to be considered when increasing the acquired resolution. The image should still provide sufficient signal from the lymph nodes instead of noise.

TR, TE and NEX

TR and TE were mainly determined by the capabilities of the PET/MR system and head-neck coil. A long TR can improve the SNR. However, at a certain length the signal strength improvement is limited compared to the additional time required for the acquisition. The PET/MR system provides internal calibration for the TR which was used to determine a sufficient balance of image signal and scan time. The TE was always the minimal time capable by the PET/MR system. A NEX of two is conventional. Higher NEX reduces noise, while increasing scan time. Identical to the TR, the noise reduction is evaluated compared to the scan time increase required, determining a sufficient compromise.

FOV

The lymph node levels in the head and neck region (see Figure 1.1a) describe lymph nodes between the base of the skull at the jugular fossa superior until the clavicle. A FOV of 220-240mm should cover all or most of these node levels [39]. Additional height can be used to fully include the nasal cavity in larger subjects or lymph node stations subclavicular. Suspected lymph nodes can fall outside of the FOV when a smaller FOV will be used. Enlarging the FOV might provide additional information but is not required for answering the objective of this clinical study. Therefore, it will be an unnecessarily increase of the scan time.

Scan time

An overall scan time of 4-6 minutes was selected to limit the amount of motion within the sequence while providing adequate time to retrieve signal within the entire FOV. Longer scan times could provide higher SNR but will not be implemented easily in clinical practice because of time constrains per patient.

Quality evaluation
From the resulting DWI images, artefacts and the goodness of fit of the quantitative diffusion parameters were determined and used for evaluation of the overall image quality. SNR was calculated according to Equation 2.1[40].

$$SNR = \frac{\mu_{sig}}{\sigma_{sig}} \tag{2.1}$$

μ_{sig} = mean pixel value of parotid gland

σ_{sig} = background standard deviation

Artefacts present in DWI images often include, ghosting, eddy currents, insufficient fat suppression and geometric distortions. The presence and severity of these artefacts were visually reviewed and graded. Reduction in artefacts was determined by visual comparison of the image with imaging from previous scan sessions. Geometric distortion of the image is a known issue with DWI. The single-shot spin-echo echo-planar imaging (SE-EPI) acquisition sequence is used most often for DWI. The high sensitivity of SE-EPI to sharp signal intensity transitions in the image causes the distortions. Distortions mainly occur in the phase encoding direction of the image. Two methods to reduce the effect of geometric distortion were available for testing:

Method 1. The GE Healthcare PET/MR system provides a build in distortion correction method based on MRI gradient field nonlinearity to reduce distortion during image acquisition. Further details on the method are undisclosed [41, 42].

Method 2. The Functional Magnetic Resonance Imaging of the Brain software library (FSL) offers a method to estimate and correct susceptibility induced distortions. A pair of DW images has to be acquired. One of the pair is a standard DWI. For the other, referred to as the pepolar image, the phase encoding direction and thus the direction of distortion is reversed. The pair of the standard and pepolar DW images are combined as described by Andersson, Skare, and Ashburner [43] to determine a single corrected DW image using FSL [44].

Table 2.1. DWI-IVIM scan parameter targets [35].

Scan parameter	Target	Ideal
Slice thickness (mm)	5-7	<5
TR (ms)	3000-5000	>5000
TE (ms)	minimum TE	<60
NEX	2	>2
FOV (mm)	220-240	>220
Scan time (min)	4-6	<4

2.1.2. DCE-MRI

With a DCE-MRI acquisition, only semi-quantitative parameters can be determined. To obtain quantitative parameters of permeability, T_1 and B_1 maps have to be included in the scan protocol as well. The T_1 map provides a quantified T_1 image. The B_1 map captures the B-field inhomogeneities. A pharmacokinetic model was used to calculate tissue permeability described by multiple quantitative parameters. The permeability from the plasma to the extravascular-extracellular space (EES) is described by K^{trans}. K_{ep} describes the permeability from the EES to the plasma. V_p is a measure of the fraction of plasma volume per voxel. Additional details on DCE-MRI can be found in the literature review available in the Appendix A.

Fast dynamic imaging is essential to accurately capture the wash-in and wash-out of the contrast in a tissue. Accurate and often measurements of the chance in contrast intensity of a tissue improve the accuracy of the pharmacokinetic model. With the introduction of the differential sub-sampling with Cartesian ordering (DISCO) method [45] for DCE-MRI, a faster method to perform the DCE-MRI acquisitions became available for GE MR systems. Within the Erasmus MC the DISCO method has already

been optimised for the application in the knee and hip region. This DCE-MRI sequence formed the basis for further optimisation in the head and neck region for the current project.

The scan parameter targets were based on the QIBA DCE-MRI Quantification profile [46]. Slight variations in target and ideal scan parameter values exists because of differences between the used scanner hardware. Literature studies performing DCE-MRI in the head and neck region were consulted when specifying the scan parameters. Specific scan parameters for these sequences included the flip angles and the temporal resolution and scan time of the dynamic imaging. Other scan parameters included for optimisation were: slice thickness, FOV, scan time, NEX, TR and TE.

Slice thickness, TR, TE, NEX, FOV and scan time

The size and time constrains for the DWI-IVIM acquisition also apply for the DCE-MRI. Therefore, the targets for slice thickness, TR, TE, NEX, FOV and scan time were determined identically to the DWI-IVIM targets (see Table 2.2).

Flip angles

The flip angles for the T_1 map and dynamic T_1w images were determined based on the T_1 relaxation times of (metastatic) lymph nodes [47, 48]. For the T_1 mapping at least five baseline images (phases) should be acquired of each flip angle (FA).

Temporal resolution

Because of the relatively high perfusion rate of the neck a temporal resolution of five seconds or lower is preferred to accurately capture the MRI contrast peak and arrival. A balance between temporal resolution and SNR should be found. Scan times of the dynamic imaging should be 4-6 min to image contrast wash-out from the tissue. Preferably longer to increase the accuracy of the permeability measure of the quantification model.

Quality evaluation

Artefacts for DCE-MRI include motion artefacts, inflow effect and geometric distortions. Artefacts visible in the images were determined by visual comparison between different scan parameter settings. The risk of motion artefacts can be reduced by a higher temporal resolution. The inflow effect is an increase of the signal in arteries caused by their blood flow. Arteries lined up with the slice selection direction will have inflow of new blood from outside of the FOV after pulse excitation. This new non-excited blood increases the measured return signal of the artery compared to arteries with only pulse excited blood.

Table 2.2. DCE-MRI scan parameter targets [46]

Scan parameter	Target	Ideal
Slice thickness (mm)	5.1-6	<5
FOV (mm)	220-240	>220
NEX	2	>2
TR (ms)	3-5	<3
TE (ms)	1.5-2.0	<1.5
Temporal Resolution (sec)	5-10	<5
Scan time (min)	4-6	>6

2.2. Results

Six volunteer scan sessions and one phantom scan were performed on the PET/MR system. The resulting set of parameters for the DWI-IVIM is described in Table 2.3. The b-values used for the DWI-IVIM acquisition were acquired interleaved similar as the method described by Sijtsema et al [cite] and shown in Table 2.4. From the two methods of distortion correction described for DWI-IVIM, FSL provided the best results. Therefore, the FSL method was selected to perform the geometric distortions correction.

For the T_1 map, a variable flip angle (VFA) acquisition was performed. This included three T_1w acquisitions with a flip angle of 2, 8 and 12 degrees (Table 2.5). Each acquisition consisted of six phases.

Table 2.3. Acquisition parameter DWI-IVIM

Sequence	TR (ms)	TE (ms)	Frequency direction	Matrix	Resolution (mm^3)	NEX	b-values	Geometric correction
EPI	2500	71.1	R/L	128x128	2.2x2.2x4.0	2	15	FSL
pepolar-EPI	2500	71.1	R/L	128x128	2.2x2.2x4.0	2	1	FSL

Table 2.4. Interleaved b-values for DWI-IVIM

phase	b-value	phase	b-value	phase	b-value
1	0	6	10	11	270
2	10	7	350	12	50
3	820	8	40	13	140
4	10	9	340	14	90
5	820	10	50	15	130

For the T_1w acquisition of FA 12 the first 6 phases of the dynamic DISCO sequence was used. The MRI contrast was injected 15 sec after start of the dynamic imaging to ensure no contrast was visible in the first 6 phases of the acquisition. The dynamic DISCO sequence consisted of 91 phases with a temporal resolution of 3.3 seconds resulting in a scan time of 5 minutes. Lymph nodes often reside in fat, therefore the water only dynamic DISCO images (DISCO Flex) improved the delineation of the lymph nodes.

Table 2.5. Acquisition parameter DCE MRI

Sequence	TR (ms)	TE (ms)	FA (deg)	Frequency direction	Matrix	Resolution (mm^3)	Temporal resolution (sec)	Phases (#)
T_1 map	5.0	1.7	2/8	R/L	128x128	2.2x2.2x3.0	3.3	6
B_1 map	5.0	1.7	10	R/L	128x128	2.2x2.2x10.0	N/A	9
DISCO Flex	5.0	1.7	12	R/L	128x128	2.2x2.2x3.0	3.3	91

2.3. Discussion

The final scan parameters produced DWI-IVIM and DCE-MRI images of sufficient quality taking into account the study considerations. The main limitation reducing the image quality was the overall time available for the acquisition. For a practical implementation of the sequences in the daily practice, the full set of acquisitions could not take longer than 15 minutes.

Still a significant amount of noise is present in the DWI-IVIM images. With 15 b-values, each individual DW image at a specific b-value is relatively short. Higher b-values naturally have higher noise levels, and therefore some additional scan time would have been beneficial for the SNR. The main limitation of the DCE-MRI was the presence of artefacts caused by inflow effects. Changing the phase-encoding direction would have reduced the artefacts. However, it would have significantly increased motion artefacts and decreased overall image quality. Inflow effects reduce the accuracy of the arterial input function (AIF) required as an input for the pharmacokinetic model. Instead of using a subject-based AIF, a population based AIF can be used. Previous studies have shown that a population-based AIF can be used as a viable alternative to the personal AIF [49]. Therefore, it was chosen to permit the inflow effect.

The final spatial resolution of 2.2x2.2x4.0mm^3 is smaller than the targeted 5.0mm. The goal of this study was to measure the physiological parameters of suspected lymph nodes. A smaller voxels size increases the number of voxels with only lymph node data. Furthermore, suspected lymph nodes often have a smaller size. At 2.2x2.2mm^2 DWI-IVIM and DCE-MRI provide sufficient SNR. However, as

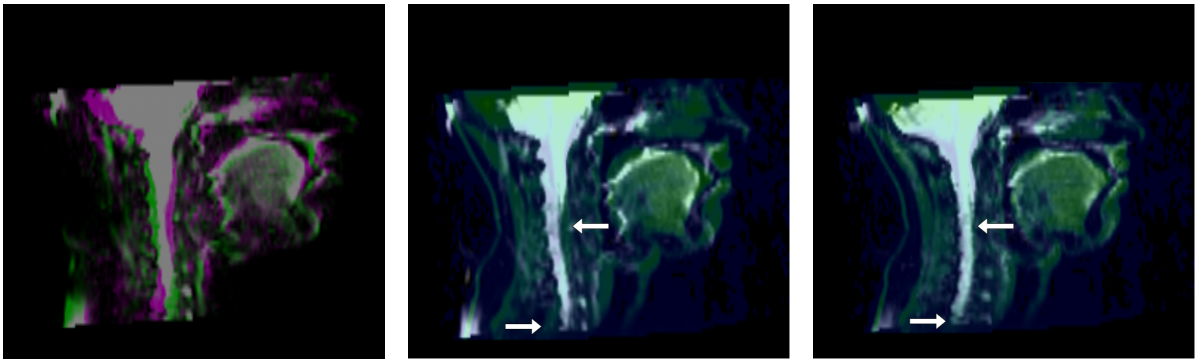

(a) (b) (c)

Figure 2.1. Comparison of geometric distortion correction DWI by GE Healthcare build-in method 1 and FSL method 2. ***(a)*** **DWI geometric distortion corrected image by GE Healthcare method 1 (green) overlayed on geometric distortion correct image by FSL method 2 (purple).** ***(b)*** **DWI distortion corrected image by GE Healthcare method 1 (grey-scale) compared to T_1w image (blue/green-scale). Arrows show the distortion of the spinal cord in the DWI (grey) and T_1w (green) image.** ***(c)*** **DWI distortion corrected image by FSL method 2 (grey-scale) compared to T_1w image (blue/green-scale). Arrows show the close relation of the spinal cord in the DWI (grey) and T_1w (green) image.**

described, the SNR of the DWI-IVIM at higher b-values was relatively low. Therefore, a slice thickness of 4mm was used for DWI-IVIM compared to the 3mm for DCE-MRI, to increase the SNR.

To improve the comparability between scanned subjects, a predefined TR and TE have been selected near the value determined by the PET/MR system. Those values were the minimum values capable by the PET/MR system for the specific health volunteers. The predefined TR and TE were rounded up to compensate for the variation between subjects and thereby the minimal capable values for TR and TE per subject.

DWI-IVIM is prone for artefacts. Ghosting, geometric distortions and insufficient fat suppression were often visible during testing. The final acquisition parameters have shown to minimise the number of artefacts in the images. A larger FOV reduced ghosting effects. The use of additional shimming of the shoulders improved the fat suppression. Geometric distortions were best corrected by the FSL method using the pepolar image (see Figure 2.1). Still, DWI-IVIM had a higher sensitivity for artefacts caused by motion and metal during imaging compared to other MRI sequences.

The final set of DWI-IVIM and DCE-MRI acquisitions have been carefully selected and optimised for imaging of lymph nodes in the head and neck region. Further optimisation of these sequences is possible mainly by increasing the scan time. However, the described parameters are optimally balanced for sufficient image signal and practical scan time for the study.

3

H&M study

The objective of this study was to determine the added predictive value of quantitative physiological MRI in head and neck PET/MR for the detection of metastatic SCCs lymph nodes.

3.1. Methods

3.1.1. Patient population

This prospective study was approved by the local institutional review board and performed according to the relevant guidelines. Between September and December 2022 patients scheduled for a standard diagnostic PET/MR exam of the head and neck region with (suspected) SCC were included. Signed informed consent was obtained prior to inclusion for all participating patients.

3.1.2. Image acquisition

Each patient received the standard diagnostic PET/MR, including a whole-body protocol and dedicated head and neck PET/MR imaging. The dedicated PET/MR included a standard diagnostic MRI protocol of the head and neck region clinically used within our institution. The whole-body PET/MR images were not used in this study and were therefore not further considered for this study.

Imaging was performed on a 3T PET/MR system (Signa PET/MR, GE Healthcare, USA; software version MP26 R02) using the 19 channel head-neck(HNU) coil.

PET protocol

Each patient was instructed to minimise exercising 24h before imaging and fasting 6h before imaging. The Radiotracer activity was determined on the subject's weight. 1.7 $MBq * subject\ weight[Kg]$ of ^{18}F-FDG was injected 60 minutes before acquisition. After injection of the radiotracer each patient rested for 45 min before the PET/MR scan. Whole-body PET/MR imaging was started 60 minutes post-injection, followed by the dedicated head and neck PET/MR images. The dedicated PET image was acquired for 10 minutes. Default Dixon-based attenuation correction (AC)-method provided by the vendor was used for MR-based attenuation correction. A Bayesian penalised likelihood reconstruction algorithm (Q.clear, GE Healthcare) was used to reconstruct the PET ^{18}F-FDG images. The reconstruction used a β-value of 150, 256x256 matrix and 60 cm FOV.

MRI protocol

The standard diagnostic MRI scan protocol of the head and neck region that was acquired simultaneously with the dedicated PET acquisition included anatomical T_1w, T_2w images and T_1w images after injection of a gadolinium (Gd)-based contrast agent. The T_1w acquisition was an axial fast spin echo (FSE) sequence with a slice thickness of 3.0mm. The T_2w image used the same slice thickness of 3.0mm, but an axial fast relaxation fast spin echo (FRFSE) sequence. The T_1w Gd image was equal to the T_1w sequence pre-contrast. A FSE iterative decomposition of water and fat with echo asymmetry and least-squares estimation (IDEAL) sequences was used for the coronal fat separated T_1w Gd image.

The physiological images were acquired after the anatomical T_2w image. DWI-IVIM acquisitions were acquired with scan parameters as determined by the MRI optimisation (see Table 2.3). The T_1w images with FA 2 and 8 (see Table 2.5) were acquired for the T_1 mapping and followed by the B_1 map before contrast injection. Gadobutrol contrast agent (Gadovist, Bayer Healthcare Pharmaceuticals) was injected with a MR injection system (MEDRAD, Bayer Radiology). After a delay of 15 sec the injection was activated and the dynamic DCE-MRI was acquired with scan parameters described in Table 2.5. The total acquisition time of the T_1 mapping and DCE-MRI took 5 minutes and 67 seconds without the time for the B_1 map.

Table 3.1. Overview of head-neck MRI protocol.

Type	Orientation	Sequence	Remarks
T_1w image	Axial	FSE	slice thickness: 3.0mm
T_2w image	Axial	FRFSE	slice thickness: 3.0mm
DWI-IVIM*	Axial	SE-EPI	b-values: 0, 10-820
DWI-IVIM pepolar*	Axial	SE-EPI	b-value: 10
T_1 **map***	Axial		FA: 2
T_1 **map***	Axial		FA: 8
B_1 **map***	Axial		
DCE-MRI*	Axial	DISCO Flex	Temporal resolution: 3.3sec
T_1w Gd image	Axial	FSE	slice thickness: 3.0mm
T_1w Gd image	Coronal	IDEAL	slice thickness: 3.5mm

* nonstandard physiological MRI sequences of this study protocol.

3.1.3. Lymph node selection

Head and neck lymph nodes identified by an experienced radiologist or nuclear medicine physician were included for processing and analysis. Metastatic lymph nodes were determined based on the pathology results of a FNAC or neck dissection. Pathology of FNAC lymph nodes could be linked to an individual lymph node on the PET/MR imaging with high certainty. Pathology of neck dissection lymph nodes were only considered if there was a high certainty it could be linked to specific nodes identified on the PET/MR images.

Based on the report of the radiologist and nuclear medicine physician each lymph node was characterised as non-suspect, suspect or pathological. In case the radiologist and nuclear medicine physician disagreed on the lymph node status, the conservative option was chosen. For example, if a lymph node was non-suspect according to the radiologist, but the nuclear medicine physician described the node as suspect, the node was labelled as suspect.

3.1.4. Processing

Each PET/MR dataset was processed individually. A dedicated set of processing steps was used for each type of image acquisition visible as the pillars in Figure 3.1. The PET ^{18}F-FDG, DWI-IVIM and DCE-MRI pillars result in descriptive quantitative physiological parameters. An axial short axis diameter was determined as additional parameter on the T_1w image.

T_1w image

Delineation of the selected lymph nodes was performed by one observer using the software program 3D Slicer (`https://slicer.org`) [50], and verified by one experienced neuroradiologist. The T_1w and T_2w images were used to determine the boundaries of the node. The T_1w image was used to define the true location of the lymph node if a difference in position existed between the T_1w and T_2w images. Masks of only the lymph node region of interests (ROIs) were used for processing to minimise the amount of data that was needed to be calculated and saved. From all lymph node ROIs of one subject, one binary mask was created. The volume of each lymph nodes in the mask was enlarged for context of the surroundings of the lymph node after processing.

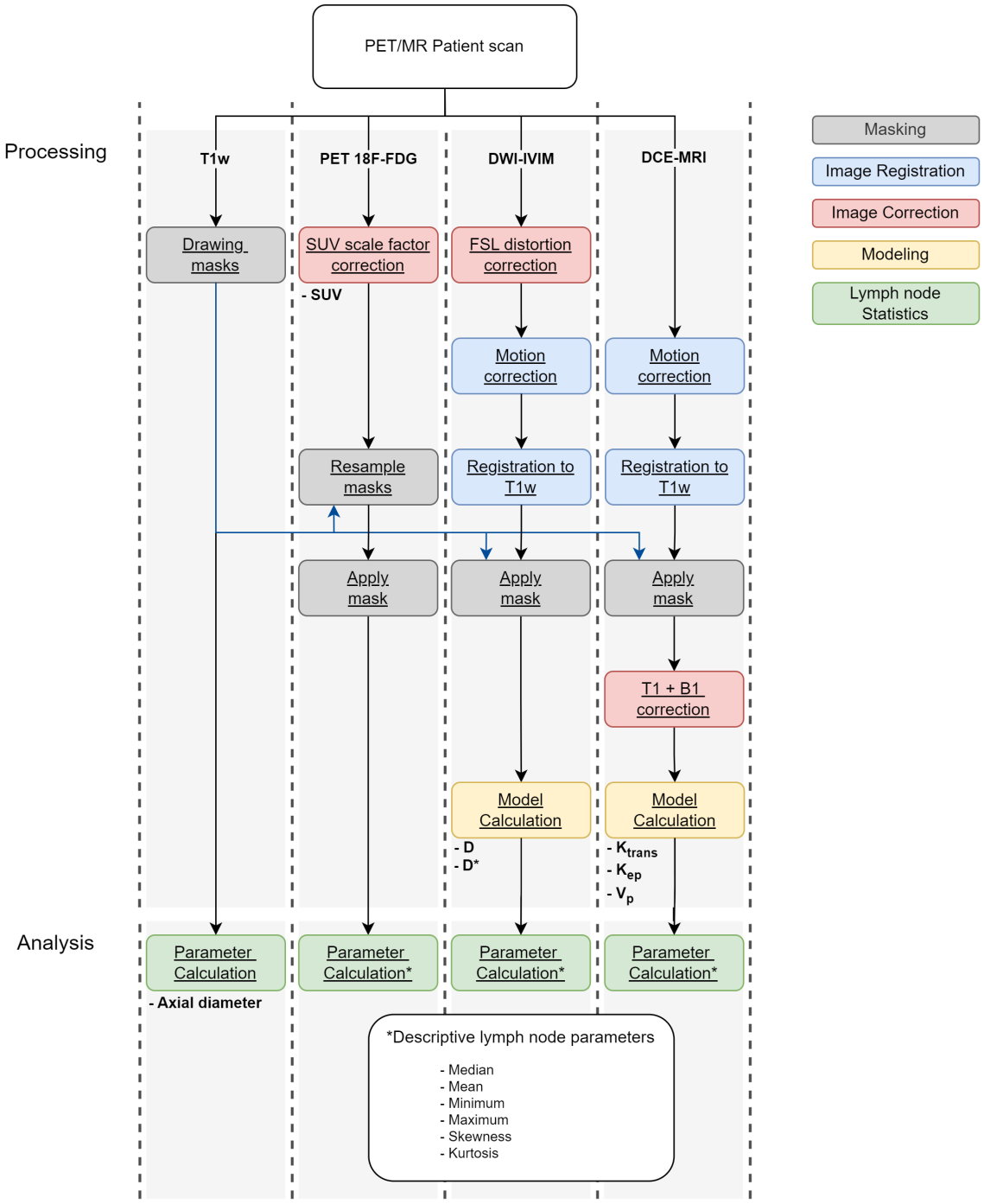

Figure 3.1. Schematic overview of the image processing pipeline.

PET ^{18}F-FDG SUV

DICOM header data was used to calculate the SUV scale factor required to determine the ^{18}F-FDG voxel-wise SUV values. Subject weight, total radionuclide dose, radionuclide half-life, injection time and PET start time were manually or automatically added to the DICOM header during PET/MR acquisition. The $SUV_{scalefactor}$ is described by Equation 3.1, Equation 3.2, and Equation 3.3, where the ^{18}F-FDG half-life is $6.59x10^3$ seconds.

$$SUV_{scale\ factor} = \frac{Patient\ Weight * 1000}{Decay\ Correction * Total\ Radionuclide\ Dose} \tag{3.1}$$

$$Decay\ Correction = 0.5^{\frac{\Delta Decay\ Time}{^{18}F-FDG\ half-life}} \tag{3.2}$$

$$\Delta Decay\ Time = Acquisition\ Start\ Time - Injection\ Time \tag{3.3}$$

No registration of the PET images to the T1w images was performed because during the 10 minutes of PET acquisition small movements are combined in the final PET image. Therefore, the resulting lymph nodes are too blurry and too small for a registration to be useful. To determine the ^{18}F-FDG SUV voxels that were included within the lymph nodes resampling of the T1w lymph node masks to the ^{18}F-FDG SUV matrix was performed by a K-Nearest Neighbour (KNN) interpolator (see Figure 3.2). The resulting resampled image is a representation of the binary mask at the resolution of the ^{18}F-FDG SUV image.

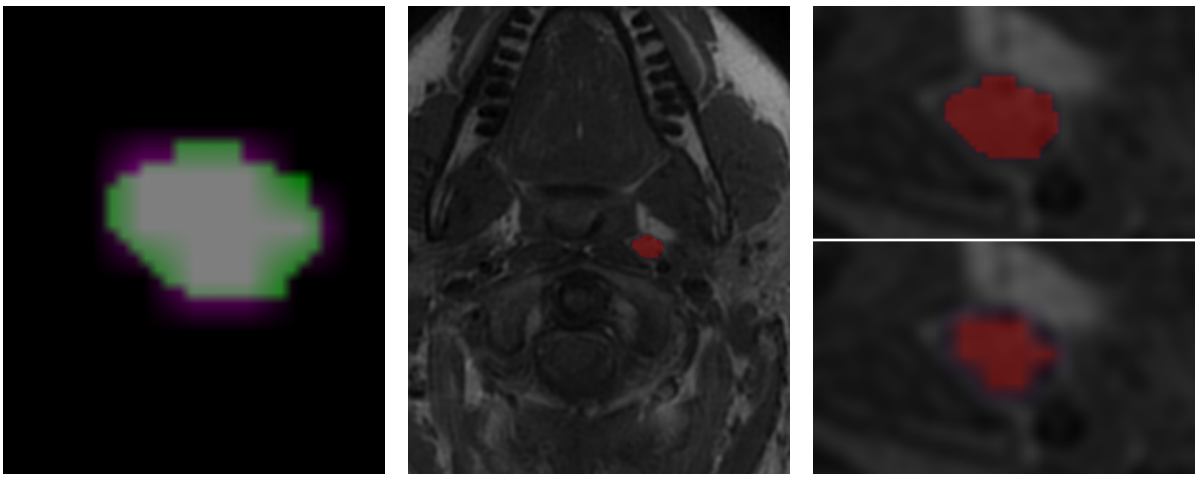

(a) (b) (c)

Figure 3.2. Resampling of lymph node mask with KNN method. *a)* Original lymph node mask (green) overlayed on resampled lymph node mask (purple). *b)* Original lymph node mask (red) visualised on T_1w image. *c)* Original lymph node mask (upper) compared to resampled lymph node mask (lower) visualised on T_1w images.

DWI-IVIM parameters

To reduce the geometric deformations in the DWI-IVIM imaging the susceptibility induced distortion correction method from FSL was used (see Figure 3.3) as described in the MRI optimisation. The acquired DWI and DWI pepolar pair was provided to the FSL topup module (`https://fsl.fmrib.ox.ac.uk/fsl/fslwiki/topup`) [44]. The phase encoding direction and total readout time for each correction were retrieved from the DICOM header provided by the PET/MR system.

The distortion correction performed by FSL also reduces motion between the DWI-IVIM phases. However, as the main purpose of the FSL is to remove geometric distortion, some residual motion can still be present in the FSL corrected imaging. An example of the FSL geometric distortion corrections

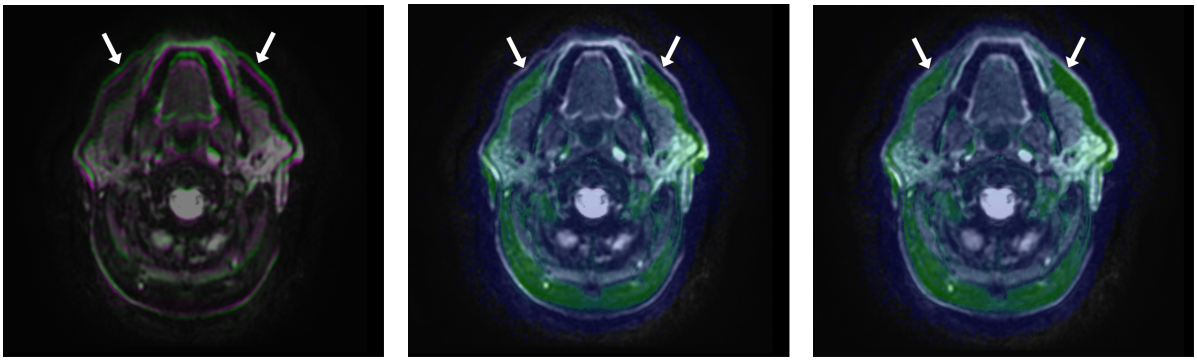

(a) (b) (c)

Figure 3.3. Result of the geometric correction with the FSL method. *a)* DWI of the neck with b-value 10 before (green) and after (purple) geometric correction. Geometric deformation is mainly visible in the anterior/posterior (A/P) direction because of the A/P phase encoding direction. *b)* DWI neck image before geometric correction (grey-scale) compared with the T_1w image (blue/green-scale). The arrows show a clear mismatch between the DWI and the T_1w image. *c)* DWI neck image after geometric correction (grey-scale) compared with the T_1w image (blue/green-scale). The mismatch near the arrows is clearly reduced by the FSL distortion correction method.

is shown in Figure 3.3. To further minimise the subject motion between phases, a group-wise affine registration was performed. This four resolutions registration was performed using Elastix (`https://elastix.lumc.nl/`) using an adaptive stochastic gradient descent optimiser and a B-spline interpolator [51, 52].

A rigid registration of the DWI-IVIM with the T_1w image was performed to reduce the differences in positioning of the DWI-IVIM and lymph node masks. The DWI-IVIM are registered with a three resolutions registration using an adaptive stochastic gradient descent optimiser and B-spline interpolator. The output DWI-IVIM images have been sampled by the interpolator to the T_1w fixed image matrix. No further resampling was needed to apply the lymph node mask on the registered DWI-IVIM image.

A voxel-wise fit was performed on each DWI voxel of the lymph node mask. Equation 3.4 describes the fit performed, where D_{tissue} is the diffusion rate of the tissue and D^* the pseudodiffusion [53, 54, 55]. Further details on the DWI-IVIM technique are described in Appendix A.

$$S/S_0 = f exp[-b(D^* + D_{blood})] + (1-f)exp(-bD_{tissue}) \tag{3.4}$$

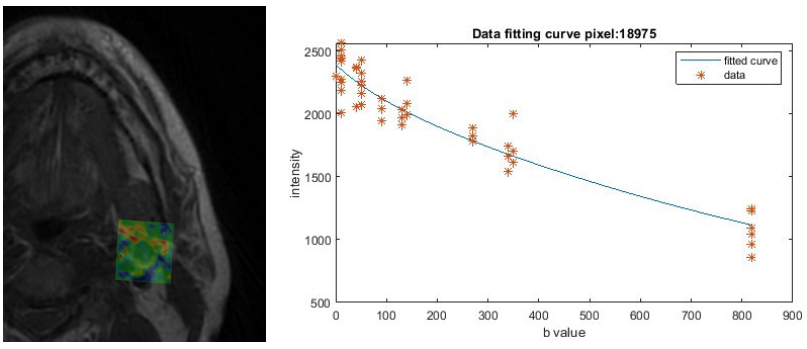

(a) (b)

Figure 3.4. Example of DWI-IVIM model fit. *a)* DWI-IVIM model outcome values of parameter D for lymph node mask. *b)* Plot of DWI signal intensity of a single voxel for all b-values with associated DWI-IVIM model fit.

Quality control is performed for each acquisition. This included a visual inspection of the image and the calculation of the temporal SNR according to Equation 3.5.

$$SNR_n = \frac{spatial\ mean\ pixel\ value\ on\ signal\ image}{spatial\ mean\ pixel\ value\ on\ temporal\ noise\ image} \tag{3.5}$$

$signal\ image$ = temporal average of pixel values within T_1w lymph node masks.
$temporal\ noise\ image$ = temporal standard deviation of pixel values within T_1w lymph node masks.

DCE-MRI parameters
Ample of time for the subject to move is available during the acquisition of the DCE-MRI images. Therefore, the DCE-MRI processing pillar uses the identical group-wise affine registration and rigid registration with the T_1w as used by the DWI-IVIM processing (see Figure 3.6.A). The T_1 maps and DCE-MRI where registered as one four-dimensional image.

After both registrations, the lymph node mask was applied before T_1 and B_1 corrections. The acquired T_1 and B_1 maps were used to determine accurate T_1 values of the neck region before contrast injection. The addition of the B_1 map decreases the influence of the MRI coil inhomogeneities during acquisition of the T_1 maps and DCE-MRI.

For calculation of the AIF, the population based AIF as described by Parker et al. [56] was used (see Figure 3.5). A mask of the vertebral artery was provided to determine a general inflow time and contrast signal intensity.

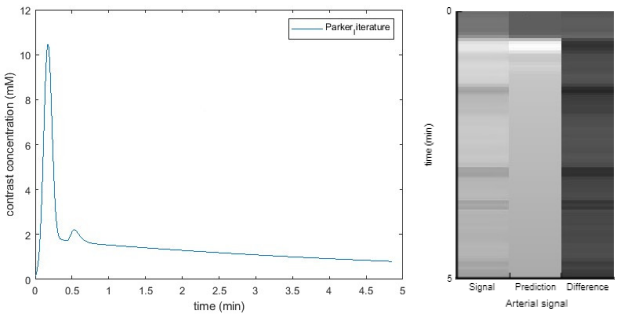

(a) **(b)**

Figure 3.5. Example of AIF calculation. *a)* population based AIF time-intensity curve. *b)* Pixel intensity of vertebral artery during dynamic imaging. Three columns depicting the measured signal, predicted value of population based AIF and the difference in signal intensity between the measured and predicted values.

Voxel-wise fit of the DCE-MRI was performed with the extended Tofts pharmacokinetic model described in Equation 3.6 [57]. Outcome parameters consist of the permeability measures K^{trans} and K_{ep}, along the volume fraction v_p (see Figure 3.6).

$$C(t) = v_p C_a(t) + K^{trans} e^{-tK_{ep}} * C_a(t) \tag{3.6}$$

The temporal SNR calculated by Equation 3.5 was used for quality control of the DCE-MRI acquisition.

3.1.5. Analysis

The physiological quantitative parameter values were calculated voxel-wise per selected lymph node. Descriptive parameters were calculated for each lymph node ROI. These include the median, mean, maximum, minimum, skewness, and kurtosis for the ^{18}F-FDG SUV, DWI-IVIM and DCE-MRI parameters per lymph node (see Figure 3.1).

All statistical analysis were performed in SPSS 28.0 (IBM, USA). This included a check for normality and multiple comparisons. The comparison between the malignant and non-malignant lymph nodes was carried out by a Mann-Whitney U test (not normally distributed data). Furthermore, a comparison

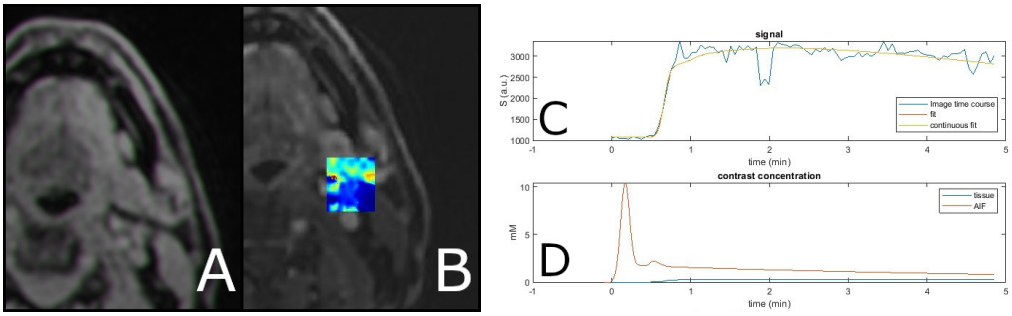

(a) (b)

Figure 3.6. Example of DCE-MRI pharmacokinetic model fit. *A)* Small transformation of the neck after group-wise rigid motion correction. Green (original image) glow on right edges and purple (transposed image) glow on left egdes show minimal translation of the image. *B)* Pharmacokinetic model outcome parameter K^{trans} of lymph node mask. *C)* Signal intensity over time of single pixel (blue) and associated pharmacokinetic model fit (yellow). *D)* Contrast concentration of single pixel over time (blue) compared to population based AIF (orange).

was performed between the pathology outcome and the reported results based on the PET/MR. A Mann-Whitney U test was used to compare the suspected and non-suspected lymph nodes without malignancy. Finally, lymph nodes with unknown pathology were visually compared to lymph nodes without malignancy to determine possible trends.

3.2. Results

In total 14 subjects were scanned with the additional physiological MRI sequences, of which ten were included for processing analysis (see Table 3.2). Four subjects were excluded because the DWI-IVIM acquisition was performed incorrectly in three cases and in one case the acquisition failed, resulting in incorrect or insufficient signal. The temporal SNR of the DWI-IVIM had a median of 6.14 (range: 5.00 - 7.41). The median temporal SNR for DCE-MRI was 2.95×10^1 (range: 1.84×10^1 - 3.63×10^1).

In the ten included subjects, 41 lymph nodes were detected on the PET/MR images (see Table 3.3). Pathology was performed on 13 of the 41 lymph nodes. In ten lymph nodes no malignancy was detected and in three lymph nodes SCC was identified. The samples for pathology were acquired by cytology in six lymph nodes and neck dissection in the other seven lymph nodes.

Table 3.2. Summary of the n=10 included subjects. Provided age, gender, and primary tumour location. Subject 06 had no SCC tumour.

Subject	Age	Gender	Primary tumour location	Number of lymph nodes	DWI-IVIM SNR	DCE-MRI SNR
01	59	Male	Tongue	2	5.47	2.96×10^1
02	61	Male	Unknown primary	6	6.82	2.48×10^1
03	29	Female	Tongue	6	5.12	3.08×10^1
04	55	Female	Oropharynx	2	7.41	3.60×10^1
05	58	Male	Unknown primary	4	†	1.84×10^1
06	20	Female	N/A	5	6.14	3.63×10^1
07	83	Male	Oropharynx	3	5.00	2.05×10^1
08	73	Male	Oropharynx	7	6.98	2.95×10^1
09	85	Male	Lymphoma	5	6.84	2.46×10^1
10	69	Male	Oropharynx	1	5.57	3.45×10^1

†Unavailable because of a technical issue.

Table 3.3. Summary of n=41 included lymph nodes.

Number of lymph nodes	41
Short axis (mm)	10.4 (8.8)
Pathology performed	13
malignant	*3*
non-malignant	*10*

3.2.1. Quantitative PET/MR measurements

Figure 3.7 provides an example of the qualitative parameter maps of the ^{18}F-FDG, DWI-IVIM and DCE-MRI parameter from which the descriptive parameters of each lymph node have been calculated.

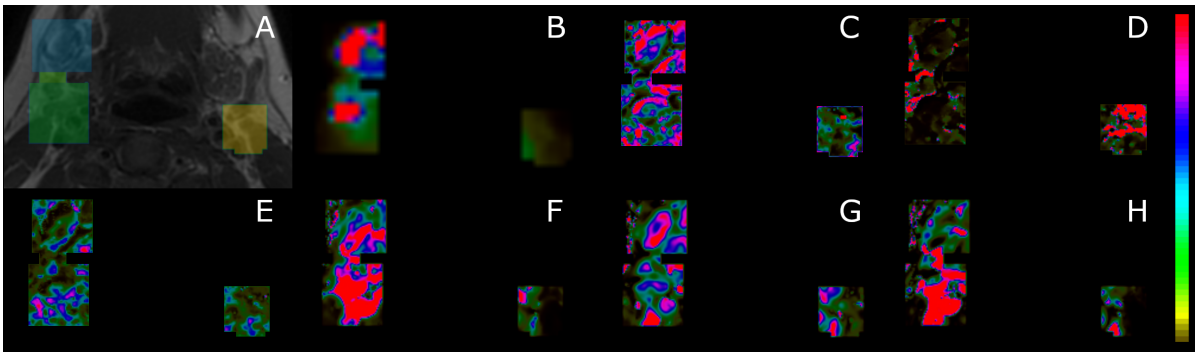

Figure 3.7. Example data of a 29-year-old female subject. *a)* T_1w image showing the lymph node masks which include the additional voxels surrounding the lymph nodes. *b-h)* Images of the quantitative parameter data of the lymph nodes and surrounding areas. The parameter images in order are, *b)* ^{18}F-FDG SUV, *c)* DWI-IVIM D (mm^2/s), *d)* DWI-IVIM D^* (mm^2/s), *e)* DWI-IVIM f, *f)* DCE-MRI K^{trans} (min^{-1}), *g)* DCE-MRI K_{ep} (min^{-1}), *h)* DCE-MRI V_p.

Multiple parameters differed significantly between the n=3 metastatic and n=10 non-metastatic lymph nodes. 12 of the 43 analysed parameters were significantly different with a p-value cut-off of 0.05 (see Table 3.4). In Figure 3.8 box-plots are show for this subgroup of parameters that showed a significant difference. A complete overview of all analysed parameters can be found in Appendix B - Supplementary Tables and Figures.

Table 3.4. Quantitative parameter correlations with pathology.

	Normal	**n=10**		**Metastatic**	**n=3**
Parameter	Median	Range	Median	Range	P-value ‡
Short axis (mm)	6.20	5.23 - 7.15	27.00	18.70 - 29.10	**0.007***
DWI-IVIM D_{max} (mm^2/s)	1.30×10^{-3}	1.20×10^{-3} - 2.00×10^{-3}	1.38×10^{-2}	3.80×10^{-3} - 2.00×10^{-2}	**0.028***
DWI-IVIM $D^*_{skewness}$	4.85	3.42 - 6.10	7.72	6.88 - 8.83	**0.049***
DWI-IVIM $D^*_{kurtosis}$	2.41×10^{1}	1.24×10^{1} - 4.38×10^{1}	9.46×10^{1}	8.20×10^{1} - 9.98×10^{1}	**0.049***
^{18}F-FDG SUV_{median}	2.35	1.62 - 3.96	4.99	4.08 - 7.91	**0.028***
^{18}F-FDG SUV_{mean}	2.62	1.91 - 4.46	5.82	4.70 - 8.94	**0.007***
^{18}F-FDG SUV_{max}	4.61	3.05 - 9.64	1.86×10^{1}	1.78×10^{1} - 3.01×10^{1}	**0.007***
DCE-MRI K^{trans}_{median} (min^{-1})	2.03×10^{-1}	1.74×10^{-1} - 7.93×10^{-1}	7.14×10^{-2}	4.61×10^{-2} - 1.30×10^{-1}	**0.014***
DCE-MRI K^{trans}_{mean} (min^{-1})	2.37×10^{-1}	1.89×10^{-1} - 7.68×10^{-1}	9.20×10^{-2}	6.78×10^{-2} - 1.50×10^{-1}	**0.028***
DCE-MRI K^{trans}_{min} (min^{-1})	3.00×10^{-2}	1.59×10^{-2} - 1.09×10^{-1}	2.22×10^{-14}	0.00 - 1.00×10^{-2}	**0.014***
DCE-MRI K_{ep-max} (min^{-1})	1.99	1.61 - 2.00	2.00	2.00 - 2.00	**0.014***
DCE-MRI $K_{ep-skewness}$	-1.74×10^{-1}	-4.85×10^{-1} - 2.79×10^{-1}	4.00×10^{-1}	1.88×10^{-1} - 8.60×10^{-1}	**0.049***

‡Mann-Whitney U test

3.2.2. PET/MR image findings

Of the 13 lymph nodes with pathology, all metastatic lymph nodes (n=3) were correctly identified by the radiologists and nuclear medicine physicians (see Table 3.5). Four lymph nodes were described as pathological based on the standard PET/MR images, however no pathology was performed on those

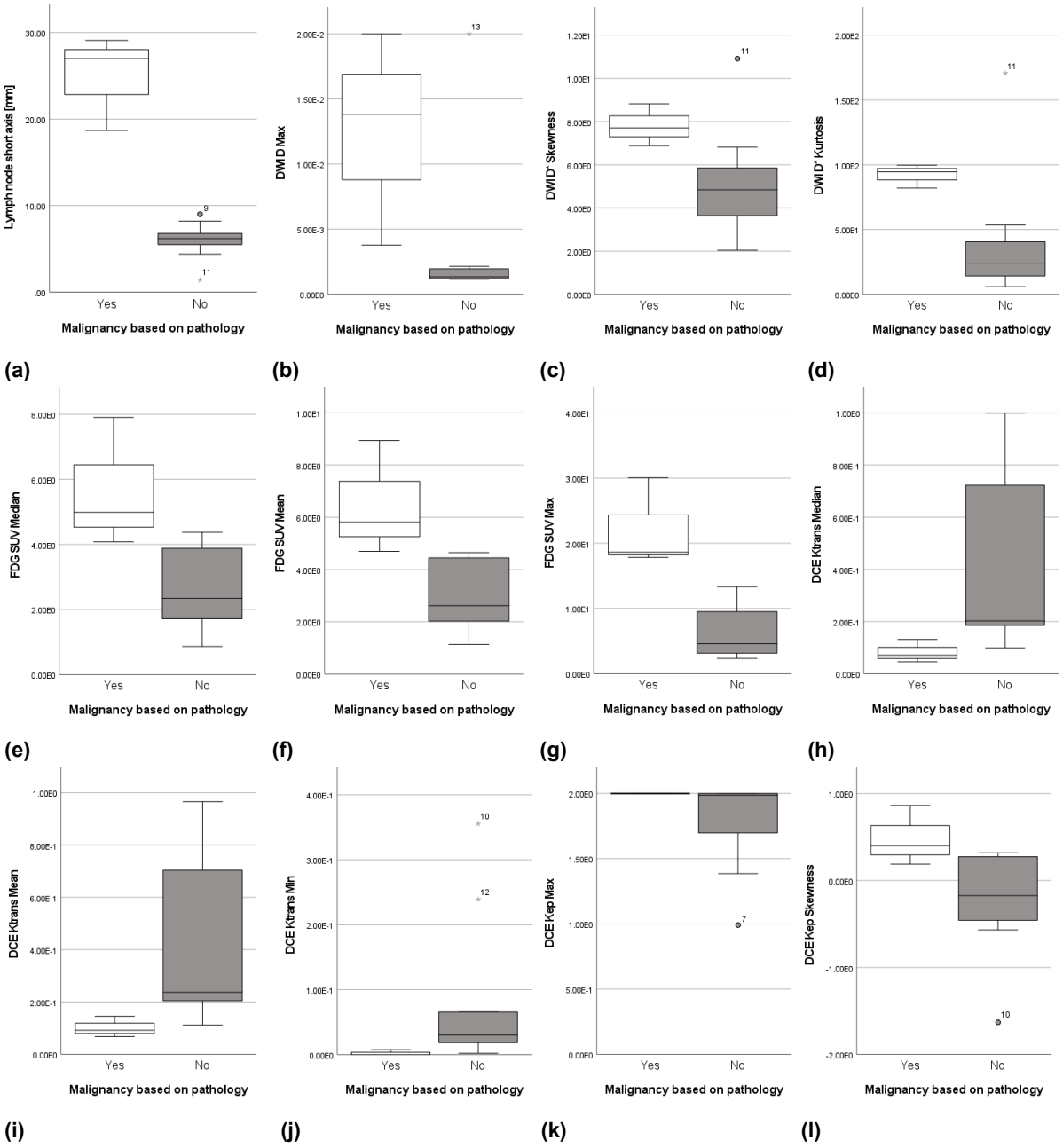

Figure 3.8. Box-plots of lymph nodes with pathology comparing the significant quantitative parameters between malignant and non-malignant lymph nodes. The quantitative parameters include: *a)* Short axis diameter (mm), *b)* DWI-IVIM D_{max} (mm^2/s), *c)* DWI-IVIM $D^*_{skewness}$, *d)* DWI-IVIM $D{*}_{kurtosis}$, *e)* ^{18}F-FDG SUV_{median}, *f)* ^{18}F-FDG SUV_{mean}, *g)* ^{18}F-FDG SUV_{max}, *h)* DCE-MRI K^{trans}_{median} (min^{-1}), *i)* DCE-MRI K^{trans}_{mean} (min^{-1}), *j)* DCE-MRI K^{trans}_{min} (min^{-1}), *k)* DCE-MRI K_{ep-max} (min^{-1}) and *l)* DCE-MRI $K_{ep-skewness}$.

lymph nodes. Four of the ten non-malignant lymph nodes were scored as non-suspected lymph nodes. The remaining six scored as suspected lymph nodes based on the standard PET/MR images.

Table 3.5. Lymph node status determined by pathology compared to the PET/MR reported results.

	Pathological	Suspect	Non-suspect	Total
malignant	3	0	0	3
Unknown	4	11	13	28
non-malignant	0	6	4	10
Total	7	17	17	41

Figure 3.9 shows the results of the non-malignant lymph nodes splitted in the suspected and non-suspected group. Of the parameter groups which were significantly different between malignant and non-malignant lymph nodes, only DCE-MRI K^{trans}_{median} and K^{trans}_{mean} showed a significant difference between the suspected and non-suspected non-malignant lymph nodes.

3.2.3. Classification by multiparametric PET/MR

Most quantitative parameter values of the lymph nodes without pathology lay within the same range of the lymph nodes without malignancy (see Figure 3.10). However, three individual lymph nodes slightly diverged from the non-malignant lymph nodes for the values of ^{18}F-FDG SUV, DWI-IVIM D^*, DCE-MRI K^{trans} and K_{ep}. Figure 3.11 shows example images of two of the diverging lymph nodes compared to an average non-malignant lymph node.

3.3. Discussion

PET/MR imaging of lymph nodes were performed and quantitative parameters could be calculated from those images. Significant differences in multiple quantitative parameters were found between malignant and non-malignant lymph nodes. Six of the ten non-malignant lymph nodes were suspected for malignancy based on the standard PET/MR images. Three lymph nodes without pathology with deviating quantitative values might indicate parameters useful to increasing the PET/MR specificity in detecting lymph node metastasis.

For 12 of 43 analysed parameters non-malignant and malignant lymph nodes were significantly different. The quantitative parameters correlating with malignancy were in line with previous literature as described in Appendix A. The already intensively researched correlation of ^{18}F-FDG SUV with malignancy was observed in the current study. Further confirmation of the correlation of DWI-IVIM D, DWI-IVIM D^*, DCE-MRI K^{trans} and DCE-MRI K_{ep} with malignancy were found. For ^{18}F-FDG SUV and DCE-MRI K^{trans}, the median and mean descriptive parameters were both significant as they describe relatively similar outcomes.

As shown by Table 3.5 all malignant nodes were described as pathological based on the standard PET/MR imaging. These lymph nodes were large in size and showed obvious signs of necrosis (see Figure 3.12.A). Furthermore, ^{18}F-FDG uptake is also increased at or on the edge of these metastatic lymph nodes. These lymph nodes can be described malignant with high certainty based on the images that are standard performed. Therefore, the term 'Pathological lymph node' is used to describe these lymph nodes by radiologist, even though no pathology has been performed. DWI-IVIM and DCE-MRI images and quantitative parameters are in these cases unnecessary imaging to determine malignancy for these lymph nodes. There is only limited added value in using DWI-IVIM and DCE-MRI for detection of metastasis in large necrotic lymph nodes compared to using T_1w, T_1w MRI and ^{18}F-FDG PET images.

However, there is also a substantial amount of lymph nodes that were suspected for malignancy based on the current standard PET/MR images. Table 3.5 describes 17 of 41 lymph nodes to be suspect. These lymph nodes do not show similar obvious features of metastasis as seen with the pathological lymph nodes, i.e., large size, necrosis and strong increase in ^{18}F-FDG uptake (see Figure 3.12.I). Lymph nodes were described as suspect if they were slightly enlarged in size, had moderate increase

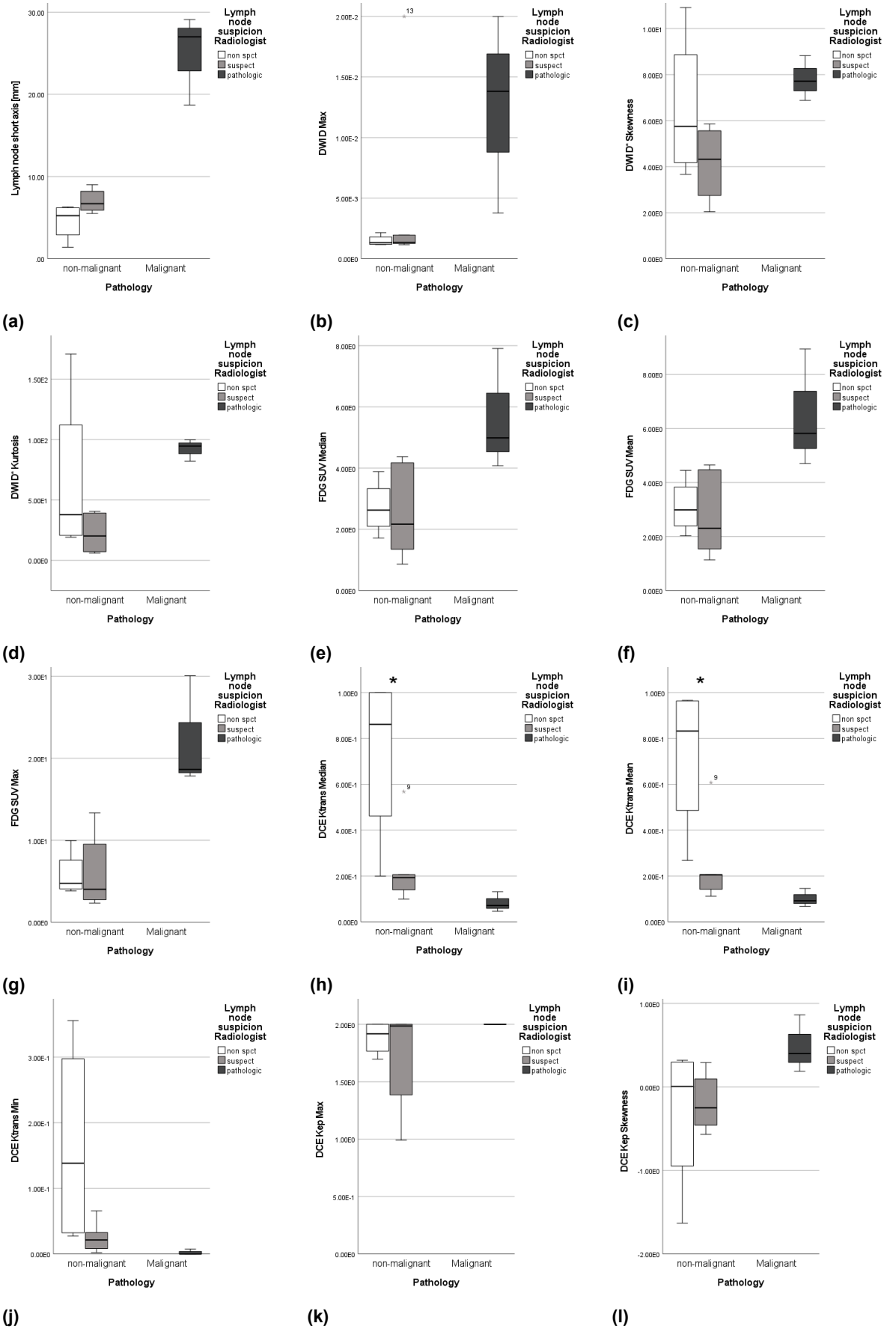

Figure 3.9. Box-plots showing suspected and non-suspected lymph nodes of the non-malignant lymph nodes. The malignant lymph nodes are provided as reference. The quantitative parameters include: *a)* Short axis diameter (mm), *b)* DWI-IVIM D_{max} (mm^2/s), *c)* DWI-IVIM $D^*_{skewness}$, *d)* DWI-IVIM $D*_{kurtosis}$, *e)* ^{18}F-FDG SUV_{median}, *f)* ^{18}F-FDG SUV_{mean}, *g)* ^{18}F-FDG SVU_{max}, *h)* DCE-MRI K^{trans}_{median} (min^{-1}), *i)* DCE-MRI K^{trans}_{mean} (min^{-1}), *j)* DCE-MRI K^{trans}_{min} (min^{-1}), *k)* DCE-MRI K_{ep-max} (min^{-1}) and *l)* DCE-MRI $K_{ep-skewness}$. * Mann-Whitney U test significant at p-value 0.05.

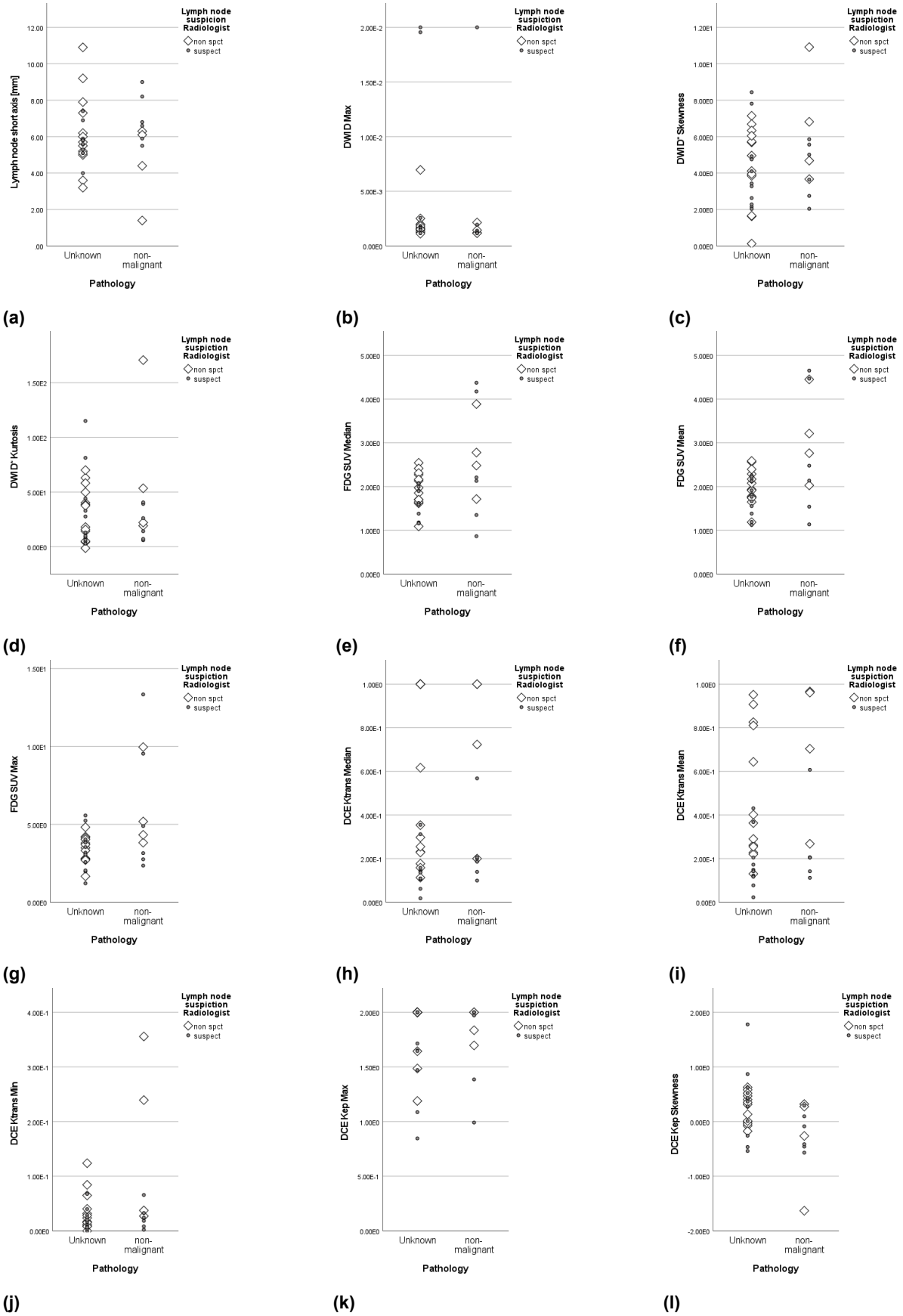

Figure 3.10. Scatterplots comparing the lymph nodes without pathology to the lymph nodes without malignancy. The quantitative parameters include: *a)* Short axis diameter (mm), *b)* DWI-IVIM D_{max} (mm^2/s), *c)* DWI-IVIM $D^*_{skewness}$, *d)* DWI-IVIM $D*_{kurtosis}$, *e)* ^{18}F-FDG SUV_{median}, *f)* ^{18}F-FDG SUV_{mean}, *g)* ^{18}F-FDG SUV_{max}, *h)* DCE-MRI K^{trans}_{median} (min^{-1}), *i)* DCE-MRI K^{trans}_{mean} (min^{-1}), *j)* DCE-MRI K^{trans}_{min} (min^{-1}), *k)* DCE-MRI K_{ep-max} (min^{-1}) and *l)* DCE-MRI $K_{ep-skewness}$. Diverging lymph nodes without pathology were described for DWI-IVIM $D^*_{kurtosis}$, ^{18}F-FDG SUV_{max}, DCE-MRI K^{trans}_{median}, DCE-MRI K^{trans}_{mean} and DCE-MRI $K_{ep-skewness}$.

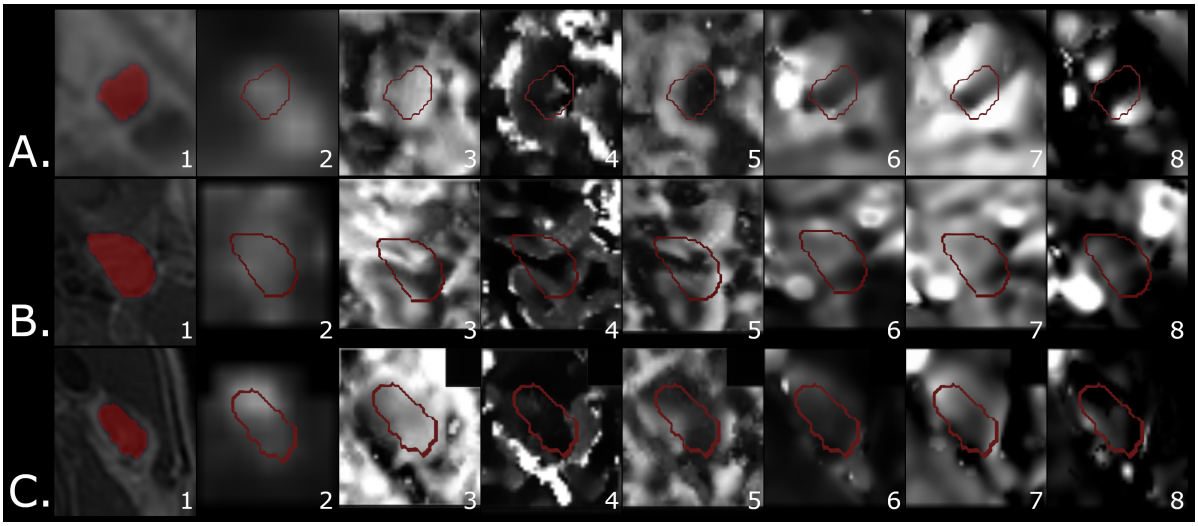

Figure 3.11. Multiparametric images of three lymph nodes. *A)* Example of an average non-metastatic lymph node *B)* Lymph node without pathology with a divergence in ^{18}F-FDG SUV_{max}, DCE-MRI K^{trans}_{median}, DCE-MRI K^{trans}_{mean} and DCE-MRI $K_{ep-skewness}$. *C)* Lymph node without pathology with a divergence in DWI-IVIM $D^{*}_{kurtosis}$ and ^{18}F-FDG SUV_{max}. Images *1-8* are respectively: *1)* T$_1$w, *2)* ^{18}F-FDG SUV, *3)* DWI-IVIM D (mm^2/s), *4)* DWI-IVIM $D*$ (mm^2/s), *5)* DWI-IVIM f, *6)* DCE-MRI K^{trans} (min^{-1}), *7)* DCE-MRI K_{ep} (min^{-1}) and *8)* DCE-MRI V_p.

in ^{18}F-FDG uptake, did not show a fatty hilum or a combination of those features.

Only for K^{trans}_{median} and K^{trans}_{mean} a distinction could be made between suspected and non-suspected lymph nodes in the non-malignant group. Unfortunately, with the small sample size conclusions should be drawn carefully. Still, this finding could indicate that adding the DCE-MRI K^{trans} to the standard diagnostic PET/MR might aid the radiologist in the identification of a suspect lymph node. A potential suspected lymph node could be remarked as non-suspect if it shows a relatively high DCE-MRI K^{trans} value. Possibly increasing the specificity for the detection of malignant lymph nodes.

This trend is further observation in the lymph nodes without pathology diverging in quantitative parameter value from non-malignant lymph nodes. A visual difference appears to be present in Figure 3.11 between the DCE-MRI K^{trans} of lymph node B and the average non-malignant lymph node A. Although, we could not say if these lymph nodes were metastatic, it is an interesting trend. A opposite trend was found for DWI-IVIM $D^{*}_{skewness}$, where lymph node C. showed a lower value compared the non-malignant lymph nodes include. While metastatic lymph nodes show a higher value compared to non-malignant lymph nodes. Still, the lack of metastatic lymph nodes described as suspect prevent any conclusion to be made for correlating the parameters with malignancy.

Four of the lymph nodes without pathology have been described as pathological based on the stand PET/MR images. These lymph node showed the typical signs of metastatic lymph nodes, large of size, necrotic and increased ^{18}F-FDG uptake. No pathology was performed on these lymph nodes because a similar nearby lymph node was used for pathology or there was limited doubt about the lymph node metastatic status and verification would not chance the treatment plan.

For the introduction of DWI-IVIM and DCE-MRI quantitative parameters into clinical practice several problems need to be overcome. Calculations of the DWI-IVIM and DCE-MRI parameters were quite computational heavy. DWI-IVIM took an average of 2-3 hours, and DCE-MRI 10-14 hours for each subject depending on the size and amount of lymph nodes, on a dedicated research workstation. Furthermore, the current processing pipeline is relatively complex and requires detailed knowledge of the used programs and performed methods, requiring manual input at several points during the analysis. Further automation of the analysis is necessary before the quantitative data could become clinically viable.

This study had some limitations. First, because of time constrains the planed database size of 25

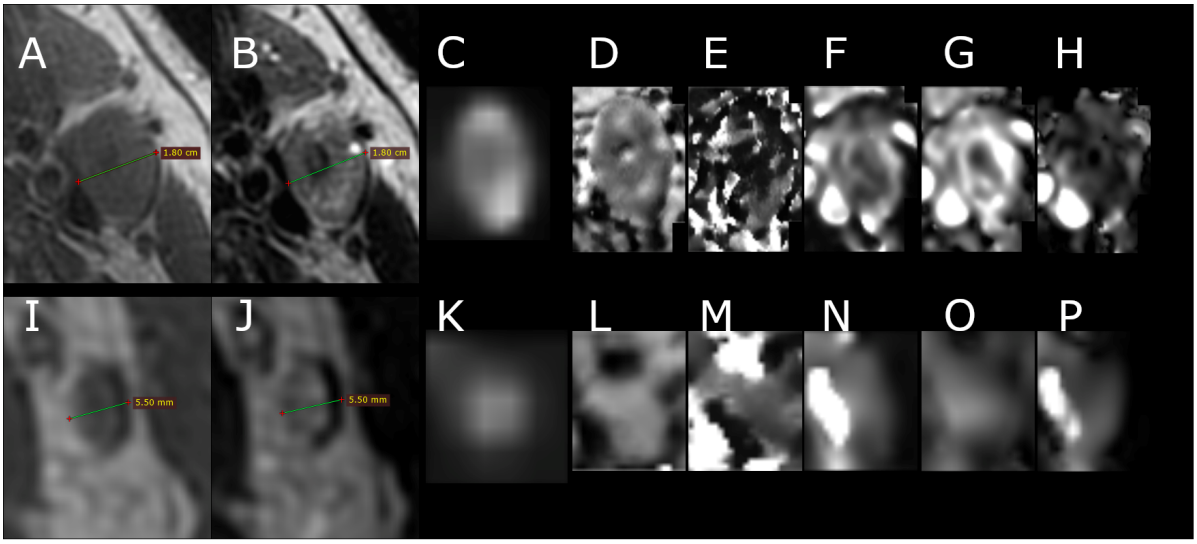

Figure 3.12. Multiparametric images of two lymph nodes. *A-H)* Large metastatic lymph node with necrosis, described as pathologic by radiologist based on the ^{18}F-FDG PET, T_1w and T_2w images. *I-P)* Enlarged non-malignant lymph node without necrosis, described as suspected by radiologist. Images in order, T_1w, T_2w, ^{18}F-FDG SUV, DWI-IVIM D, DWI-IVIM $D*$, DCE-MRI K^{trans}, DCE-MRI K_{ep} and DCE-MRI V_p.

subjects was limited to only ten subjects with 41 lymph nodes. Of the included nodes, no suspected lymph node turned out to be malignant. All six lymph nodes with pathology that were suspected, had no malignancy. Thus, a model comparing suspected lymph nodes with malignancy to suspected lymph nodes without malignancy could not be made. Furthermore, the extensive list of Mann-Whitney U tests should have required a Bonferroni multiple testing correction or only a subset of the quantitative parameters should have been evaluated.

Second, to evaluate the various PET/MR quantitative parameters for each lymph node, masking was used. These masks were drawn manually on the T_1w images. Although the process of drawing has been reviewed, inaccuracies in the lymph node masks could be present. Furthermore, the spatial resolution and slice thickness of the T_1w images different from the physiological MRI and ^{18}F-FDG PET images. To determine which voxels of quantitative parameter images fall within the lymph node mask, resampling was performed. For ^{18}F-FDG PET a resampling of the lymph node mask was performed with a KNN interpolator. The DWI and DWI-IVIM were registered to the T_1w and therefore also to the lymph node masks.

The ^{18}F-FDG PET KNN interpolation is not perfect, as visible in Figure 3.2.a. The lower resolution of the ^{18}F-FDG PET results in voxels partially covered by the original T_1w lymph node mask. The KNN selects a ^{18}F-FDG PET voxel when more than half is covered by the original lymph node mask. However, with the small masks the impact on the node area is significant, potentially losing valuable lymph node data. For the DWI-IVIM and DCE-MRI the alteration of the resolution has less effect. Both are up-sampled with a b-spline interpolator to the resolution of the T_1w. The additional voxels in the mask provide no additional information, but no data is lost either during the registration.

Third limitation is the result of the non-rigidity of lymph nodes and their location in mainly fat and other soft tissue. These small highly movable targets in the complex and flexible neck will change their position slightly even within this one-hour exam. The rigid image registration was able to reduce larger movements of the neck. Non rigid movement of the lymph nodes were not compensated. Swallowing, coughing, or speaking changed the location of the lymph node compared to rigid components of the neck. Therefore, masking of the lymph node was not always perfect. Slight mismatching of the mask has sometimes occurred between the T_1w mask and ^{18}F-FDG, DWI-IVIM and DCE-MRI.

Finally, pathology was on indicated based on the treatment plan and not for the study. Thus a subset of subjects received cytology or neck dissection. Therefore, only 13 of the included lymph nodes had a

pathological outcome. Based on prior analysis about 46% of the subject would be receiving pathology. Of the ten included subject, four received pathology. Thus, 40% of the subjects, which is in line with the predicted amount. Unfortunately, only one or two lymph nodes per subject were tested per subject. For the subjects receiving neck dissection, the pathological outcome could only be included if all lymph nodes proved non-malignant. Correct correlation between tested lymph nodes from the dissection and lymph nodes on the image could not be determined. The presumption was made that all lymph nodes per level, visible on imaging, will be tested in the group of lymph nodes acquired during neck dissection. When all nodes of a lymph node level were negative, the lymph nodes visible on imaging of the same level have been described as negative. This method is sub-optimal because a positive correlation between PET/MR and the neck dissection could not be made. With cytology it is possible to correlate the PET/MR images with the echo used for FNAC.

To conclude, this pilot study provides a methodology to determine quantitative PET/MR parameter for the head and neck region. Correlations between lymph node malignancy and quantitative parameters DWI-IVIM D, DWI-IVIM D^*, ^{18}F-FDG SUV, DCE-MRI K^{trans} and DCE-MRI K_{ep} were found. Although to increase the predictive value of the PET/MR detection of metastatic SCCs lymph nodes the quantitative physiological MRI parameters should mainly aid the specificity of the detection. Possible trends for differentiating suspected from non-malignant lymph nodes were found for DCE-MRI K^{trans}. However, a larger database of analysed lymph nodes is required to determine more concrete correlations. Fortunately, an identical study with a larger population will follow soon.

Bibliography

1. International Agency for Research on Cancer. Global Cancer Observatory. 2020. Available from: https://gco.iarc.fr/
2. Gatta G et al. Prognoses and improvement for head and neck cancers diagnosed in Europe in early 2000s: The EUROCARE-5 population-based study. European Journal of Cancer 2015 Oct; 51:2130–43. DOI: 10.1016/j.ejca.2015.07.043. Available from: https://linkinghub.elsevier.com/retrieve/pii/S0959804915007492
3. Chow LQ. Head and Neck Cancer. New England Journal of Medicine 2020 Jan; 382. Ed. by Longo DL:60–72. DOI: 10.1056/NEJMra1715715. Available from: http://www.nejm.org/doi/10.1056/NEJMra1715715
4. Braakhuis B, Brakenhoff R, and René Leemans C. Treatment choice for locally advanced head and neck cancers on the basis of risk factors: biological risk factors. Annals of Oncology 2012 Sep; 23:x173–x177. DOI: 10.1093/annonc/mds299. Available from: https://linkinghub.elsevier.com/retrieve/pii/S0923753419417523
5. Lubov J, Labbé M, Sioufi K, Morand GB, Hier MP, Khanna M, Sultanem K, and Mlynarek AM. Prognostic factors of head and neck cutaneous squamous cell carcinoma: a systematic review. Journal of Otolaryngology - Head & Neck Surgery 2021 Dec; 50:54. DOI: 10.1186/s40463-021-00529-7. Available from: https://journalotohns.biomedcentral.com/articles/10.1186/s40463-021-00529-7
6. Marcus C, Sheikhbahaei S, Shivamurthy VKN, Avey G, and Subramaniam RM. PET Imaging for Head and Neck Cancers. Radiologic Clinics of North America 2021 Sep; 59:773–88. DOI: 10.1016/j.rcl.2021.05.005. Available from: https://linkinghub.elsevier.com/retrieve/pii/S003383892100066X
7. Gao S, Li S, Yang X, and Tang Q. 18FDG PET-CT for distant metastases in patients with recurrent head and neck cancer after definitive treatment. A meta-analysis. Oral Oncology 2014 Mar; 50:163–7. DOI: 10.1016/j.oraloncology.2013.12.002. Available from: https://linkinghub.elsevier.com/retrieve/pii/S1368837513007689
8. Pijl JP, Nienhuis PH, Kwee TC, Glaudemans AW, Slart RH, and Gormsen LC. Limitations and Pitfalls of FDG-PET/CT in Infection and Inflammation. Seminars in Nuclear Medicine 2021 Nov; 51:633–45. DOI: 10.1053/j.semnuclmed.2021.06.008. Available from: https://linkinghub.elsevier.com/retrieve/pii/S0001299821000404
9. Chikamatsu K, Kamada H, Ninomiya H, Takahashi K, Sakurai T, Oriuchi N, and Furuya N. A preliminary study on sentinel lymph node biopsy: feasibility and predictive ability in oral cavity cancer. Annals of Nuclear Medicine 2004 May; 18:257–62. DOI: 10.1007/BF02985008. Available from: http://link.springer.com/10.1007/BF02985008
10. Civantos FJ, Zitsch RP, Schuller DE, Agrawal A, Smith RB, Nason R, Petruzelli G, Gourin CG, Wong RJ, Ferris RL, El Naggar A, Ridge JA, Paniello RC, Owzar K, McCall L, Chepeha DB, Yarbrough WG, and Myers JN. Sentinel Lymph Node Biopsy Accurately Stages the Regional Lymph Nodes for T1-T2 Oral Squamous Cell Carcinomas: Results of a Prospective Multi-Institutional Trial. Journal of Clinical Oncology 2010 Mar; 28:1395–400. DOI: 10.1200/JCO.2008.20.8777. Available from: https://ascopubs.org/doi/10.1200/JCO.2008.20.8777
11. Stoeckli SJ and Broglie MA. Sentinel node biopsy for early oral carcinoma. Current Opinion in Otolaryngology & Head & Neck Surgery 2012 Apr; 20:103–8. DOI: 10.1097/MOO.0b013e32834ef6d3. Available from: https://journals.lww.com/00020840-201204000-00005
12. Alvarez Amézaga J, Barbier Herrero L, Pijoan del Barrio JI, Martín Rodríguez JC, Romo Simón L, Genolla Subirats J, Rios Altolaguirre G, Ríos A de los, Arteagoitia Calvo I, Landa Llona S, Arruti González JA, López Cedrún J, and Santamaría Zuazua J. Diagnostic efficacy of sentinel node biopsy in oral squamous cell carcinoma. Cohort study and meta-analysis. Medicina oral,

patologia oral y cirugia bucal 2007 May; 12:235–43. Available from: http://www.ncbi.nlm.nih.gov/pubmed/17468723

13. Kim DH, Kim Y, Kim SW, and Hwang SH. Usefulness of Sentinel Lymph Node Biopsy for Oral Cancer: A Systematic Review and Meta□Analysis. The Laryngoscope 2021 Feb; 131:E459–E465. DOI: 10.1002/lary.28728. Available from: https://onlinelibrary.wiley.com/doi/10.1002/lary.28728
14. Peck M, Moffat D, Latham B, and Badrick T. Review of diagnostic error in anatomical pathology and the role and value of second opinions in error prevention. Journal of Clinical Pathology 2018 Nov; 71:995–1000. DOI: 10.1136/JCLINPATH-2018-205226. Available from: https://jcp.bmj.com/content/71/11/995%20https://jcp.bmj.com/content/71/11/995.abstract
15. Deschler Daniel G, Moore Michael G, and Smith Richard V. Quick Reference Guide to TNM Staging of Head and Neck Cancer and Neck Dissection Classification. American Academy of Otolaryngology-Head and Neck Surgery Foundation 2014
16. Poon CS and Stenson KM. Overview of the diagnosis and staging of head and neck cancer - UpToDate. 2022. Available from: https://www.uptodate.com/contents/overview-of-the-diagnosis-and-staging-of-head-and-neck-cancer
17. Tandon S, Shahab R, Benton JI, Ghosh SK, Sheard J, and Jones TM. Fine-needle aspiration cytology in a regional head and neck cancer center: Comparison with a systematic review and meta-analysis. Head & Neck 2008 Sep; 30. Ed. by Eisele DW:1246–52. DOI: 10.1002/hed.20849. Available from: https://onlinelibrary.wiley.com/doi/10.1002/hed.20849
18. Costantino A, Mercante G, D'Ascoli E, Ferreli F, Di Tommaso L, Franzese C, Giannitto C, Casale M, Spriano G, and De Virgilio A. Accuracy of fine-needle aspiration cytology in detecting cervical node metastasis after radiotherapy: Systematic review and meta-analysis. Head & neck 2021 Mar; 43:987–96. DOI: 10.1002/hed.26536. Available from: https://onlinelibrary.wiley.com/doi/10.1002/hed.26536
19. Shah KS and Ethunandan M. Tumour seeding after fine-needle aspiration and core biopsy of the head and neck - a systematic review. British Journal of Oral and Maxillofacial Surgery 2016 Apr; 54:260–5. DOI: 10.1016/J.BJOMS.2016.01.004
20. Ryan JL, Aaron VD, and Sims JB. PET/MRI vs PET/CT in Head and Neck Imaging: When, Why, and How? Seminars in Ultrasound, CT and MRI 2019 Oct; 40:376–90. DOI: 10.1053/J.SULT.2019.07.002
21. Cavaliere C, Romeo V, Aiello M, Mesolella M, Iorio B, Barbuto L, Cantone E, Nicolai E, and Covello M. Multiparametric evaluation by simultaneous PET-MRI examination in patients with histologically proven laryngeal cancer. European Journal of Radiology 2017 Mar; 88:47–55. DOI: 10.1016/j.ejrad.2016.12.034. Available from: https://linkinghub.elsevier.com/retrieve/pii/S0720048X16304284
22. Covello M, Cavaliere C, Aiello M, Cianelli M, Mesolella M, Iorio B, Rossi A, and Nicolai E. Simultaneous PET/MR head–neck cancer imaging: Preliminary clinical experience and multiparametric evaluation. European Journal of Radiology 2015 Jul; 84:1269–76. DOI: 10.1016/j.ejrad.2015.04.010. Available from: https://linkinghub.elsevier.com/retrieve/pii/S0720048X15001849
23. Chan SC, Yeh CH, Yen TC, Ng SH, Chang JTC, Lin CY, Yen-Ming T, Fan KH, Huang BS, Hsu CL, Chang KP, Wang HM, and Liao CT. Clinical utility of simultaneous whole-body 18F-FDG PET/MRI as a single-step imaging modality in the staging of primary nasopharyngeal carcinoma. European Journal of Nuclear Medicine and Molecular Imaging 2018 Jul; 45:1297–308. DOI: 10.1007/s00259-018-3986-3. Available from: https://link.springer.com/article/10.1007/s00259-018-3986-3
24. Sakamoto J, Imaizumi A, Sasaki Y, Kamio T, Wakoh M, Otonari-Yamamoto M, and Sano T. Comparison of accuracy of intravoxel incoherent motion and apparent diffusion coefficient techniques for predicting malignancy of head and neck tumors using half-Fourier single-shot turbo spin-echo diffusion-weighted imaging. Magnetic Resonance Imaging 2014 Sep; 32:860–6. DOI: 10.1016/j.mri.2014.05.002. Available from: https://linkinghub.elsevier.com/retrieve/pii/S0730725X1400174X

25. Xu XQ, Choi YJ, Sung YS, Yoon RG, Jang SW, Park JE, Heo YJ, Baek JH, and Lee JH. Intravoxel Incoherent Motion MR Imaging in the Head and Neck: Correlation with Dynamic Contrast-Enhanced MR Imaging and Diffusion-Weighted Imaging. Korean Journal of Radiology 2016 Oct; 17:641. DOI: 10.3348/kjr.2016.17.5.641. Available from: https://www.kjronline.org/DOIx.php?id=10.3348/kjr.2016.17.5.641
26. Ai QY, King AD, Chan JSM, Chen W, Chan KCA, Woo JKS, Zee BCY, Chan ATC, Poon DMC, Ma BBY, Hui EP, Ahuja AT, Vlantis AC, and Yuan J. Distinguishing early-stage nasopharyngeal carcinoma from benign hyperplasia using intravoxel incoherent motion diffusion-weighted MRI. European Radiology 2019 Oct; 29:5627–34. DOI: 10.1007/s00330-019-06133-8. Available from: http://link.springer.com/10.1007/s00330-019-06133-8
27. Bisdas S, Seitz O, Middendorp M, Chambron-Pinho N, Bisdas T, Vogl TJ, Hammerstingl R, Ernemann U, and Mack MG. An exploratory pilot study into the association between microcirculatory parameters derived by MRI-based pharmacokinetic analysis and glucose utilization estimated by PET-CT imaging in head and neck cancer. European Radiology 2010 Oct; 20:2358–66. DOI: 10.1007/s00330-010-1803-x. Available from: http://link.springer.com/10.1007/s00330-010-1803-x
28. Treutlein C, Stollberg A, Scherl C, Agaimy A, Ellmann S, Iro H, Lell M, Uder M, and Bäuerle T. Diagnostic value of 3D dynamic contrast-enhanced magnetic resonance imaging in lymph node metastases of head and neck tumors: a correlation study with histology. Acta Radiologica Open 2020 Aug; 9:205846012095196. DOI: 10.1177/2058460120951966. Available from: http://journals.sagepub.com/doi/10.1177/2058460120951966
29. Zheng D, Chen Y, Chen Y, Xu L, Chen W, Yao Y, Du Z, Deng X, and Chan Q. Dynamic contrast-enhanced MRI of nasopharyngeal carcinoma: A preliminary study of the correlations between quantitative parameters and clinical stage. Journal of Magnetic Resonance Imaging 2014 Apr; 39:940–8. DOI: 10.1002/jmri.24249. Available from: https://onlinelibrary.wiley.com/doi/10.1002/jmri.24249
30. Tshering Vogel DW, Zbaeren P, Geretschlaeger A, Vermathen P, De Keyzer F, and Thoeny HC. Diffusion-weighted MR imaging including bi-exponential fitting for the detection of recurrent or residual tumour after (chemo)radiotherapy for laryngeal and hypopharyngeal cancers. European Radiology 2013 Feb; 23:562–9. DOI: 10.1007/s00330-012-2596-x. Available from: http://link.springer.com/10.1007/s00330-012-2596-x
31. Becker M, Varoquaux AD, Combescure C, Rager O, Pusztaszeri M, Burkhardt K, Delattre BMA, Dulguerov P, Dulguerov N, Katirtzidou E, Caparrotti F, Ratib O, Zaidi H, and Becker CD. Local recurrence of squamous cell carcinoma of the head and neck after radio(chemo)therapy: Diagnostic performance of FDG-PET/MRI with diffusion-weighted sequences. European Radiology 2018 Feb; 28:651–63. DOI: 10.1007/s00330-017-4999-1. Available from: https://link.springer.com/article/10.1007/s00330-017-4999-1
32. Ng SH, Lin CY, Chan SC, Lin YC, Yen TC, Liao CT, Chang JTC, Ko SF, Wang HM, Chang CJ, and Wang JJ. Clinical Utility of Multimodality Imaging with Dynamic Contrast-Enhanced MRI, Diffusion-Weighted MRI, and 18F-FDG PET/CT for the Prediction of Neck Control in Oropharyngeal or Hypopharyngeal Squamous Cell Carcinoma Treated with Chemoradiation. PLoS ONE 2014 Dec; 9. Ed. by Khong PL:e115933. DOI: 10.1371/journal.pone.0115933. Available from: https://journals.plos.org/plosone/article?id=10.1371/journal.pone.0115933
33. Shukla-Dave A, Lee NY, Jansen JF, Thaler HT, Stambuk HE, Fury MG, Patel SG, Moreira AL, Sherman E, Karimi S, Wang Y, Kraus D, Shah JP, Pfister DG, and Koutcher JA. Dynamic Contrast-Enhanced Magnetic Resonance Imaging as a Predictor of Outcome in Head-and-Neck Squamous Cell Carcinoma Patients With Nodal Metastases. International Journal of Radiation Oncology*Biology*Physics 2012 Apr; 82:1837–44. DOI: 10.1016/j.ijrobp.2011.03.006. Available from: https://linkinghub.elsevier.com/retrieve/pii/S0360301611004597
34. Shinohara RT, Sweeney EM, Goldsmith J, Shiee N, Mateen FJ, Calabresi PA, Jarso S, Pham DL, Reich DS, and Crainiceanu CM. Statistical normalization techniques for magnetic resonance imaging. NeuroImage: Clinical 2014 Jan; 6:9–19. DOI: 10.1016/J.NICL.2014.08.008
35. QIBA MR Biomarker Committee. MR Diffusion-Weighted Imaging. Quantitative Imaging Biomarkers Alliance 2019 Dec. Available from: https://qibawiki.rsna.org/index.php/Profiles

36. Deng F, Foley R, and Bell D. Cervical lymph node metastasis (radiologic criteria). Radiopaedia.org 2019 Feb. DOI: 10.53347/RID-66437. Available from: http://radiopaedia.org/articles/66437
37. Van Den Brekel MW, Stel HV, Castelijns JA, Nauta JJ, Van Der Waal I, Valk J, Meyer CJ, and Snow GB. Cervical lymph node metastasis: Assessment of radiologic criteria. Radiology 1990; 177:379–84. DOI: 10.1148/RADIOLOGY.177.2.2217772
38. Lang P, Wendland MF, Saeed M, Gindele A, Rosenau W, Mathur A, Gooding CA, and Genant HK. Osteogenic sarcoma: noninvasive in vivo assessment of tumor necrosis with diffusion-weighted MR imaging. Radiology 1998 Jan; 206:227–35. DOI: 10.1148/radiology.206.1.9423677. Available from: http://pubs.rsna.org/doi/10.1148/radiology.206.1.9423677
39. Catenaccio E, Mu W, Kaplan A, Fleysher R, Kim N, Bachrach T, Zughaft Sears M, Jaspan O, Caccese J, Kim M, Wagshul M, Stewart WF, Lipton RB, and Lipton ML. Characterization of Neck Strength in Healthy Young Adults. PM & R : the journal of injury, function, and rehabilitation 2017 Sep; 9:884. DOI: 10.1016/J.PMRJ.2017.01.005. Available from: /pmc/articles/PMC5545075/%20/pmc/articles/PMC5545075/?report=abstract%20https://www.ncbi.nlm.nih.gov/pmc/articles/PMC5545075/
40. Haouimi A and Yeung J. Signal-to-noise ratio (MRI). Radiopaedia.org 2011 Jun. DOI: 10.53347/RID-14045
41. Glover GH and Pelc NJ. Method for correcting image distortion due to gradient nonuniformity. 1986. Available from: https://patents.google.com/patent/US4591789A/en?oq=US4591789
42. Bammer R, Markl M, Barnett A, Acar B, Alley MT, Pelc NJ, Glover GH, and Moseley ME. Analysis and generalized correction of the effect of spatial gradient field distortions in diffusion-weighted imaging. Magnetic Resonance in Medicine 2003 Sep; 50:560–9. DOI: 10.1002/MRM.10545. Available from: https://onlinelibrary.wiley.com/doi/full/10.1002/mrm.10545%20https://onlinelibrary.wiley.com/doi/abs/10.1002/mrm.10545%20https://onlinelibrary.wiley.com/doi/10.1002/mrm.10545
43. Andersson JL, Skare S, and Ashburner J. How to correct susceptibility distortions in spin-echo echo-planar images: application to diffusion tensor imaging. NeuroImage 2003 Oct; 20:870–88. DOI: 10.1016/S1053-8119(03)00336-7
44. Smith SM, Jenkinson M, Woolrich MW, Beckmann CF, Behrens TE, Johansen-Berg H, Bannister PR, De Luca M, Drobnjak I, Flitney DE, Niazy RK, Saunders J, Vickers J, Zhang Y, De Stefano N, Brady JM, and Matthews PM. Advances in functional and structural MR image analysis and implementation as FSL. NeuroImage 2004 Jan; 23:S208–S219. DOI: 10.1016/J.NEUROIMAGE.2004.07.051
45. Saranathan M, Rettmann DW, Hargreaves BA, Clarke SE, and Vasanawala SS. DIfferential subsampling with cartesian ordering (DISCO): A high spatio-temporal resolution dixon imaging sequence for multiphasic contrast enhanced abdominal imaging. Journal of Magnetic Resonance Imaging 2012 Jun; 35:1484–92. DOI: 10.1002/jmri.23602. Available from: https://onlinelibrary.wiley.com/doi/10.1002/jmri.23602
46. QIBA MR Biomarker Committee. MR DCE Quantification. Quantitative Imaging Biomarkers Alliance 2012 Aug. Available from: https://qibawiki.rsna.org/index.php/Profiles
47. Crescenzi R, Donahue PM, Braxton VG, Scott AO, Mahany HB, Lants SK, and Donahue MJ. 3.0T relaxation time measurements of human lymph nodes in adults with and without lymphatic insufficiency: implications for magnetic resonance lymphatic imaging. NMR in biomedicine 2018 Dec; 31:e4009. DOI: 10.1002/NBM.4009. Available from: /pmc/articles/PMC6263822/%20/pmc/articles/PMC6263822/?report=abstract%20https://www.ncbi.nlm.nih.gov/pmc/articles/PMC6263822/
48. Wagner-Manslau C, Lukas P, Herzog M, Kau R, and Beckers K. MRI and proton-NMR relaxation times in diagnosis and therapeutic monitoring of squamous cell carcinoma. European Radiology 1994 4:4 1994; 4:314–23. DOI: 10.1007/BF00599063. Available from: https://link-springer-com.eur.idm.oclc.org/article/10.1007/BF00599063
49. Koopman T, Martens RM, Lavini C, Yaqub M, Castelijns JA, Boellaard R, and Marcus JT. Repeatability of arterial input functions and kinetic parameters in muscle obtained by dynamic contrast enhanced MR imaging of the head and neck. Magnetic Resonance Imaging 2020 May;

68:1–8. DOI: 10.1016/j.mri.2020.01.010. Available from: https://linkinghub.elsevier.com/retrieve/pii/S0730725X19305880

50. Fedorov A, Beichel R, Kalpathy-Cramer J, Finet J, Fillion-Robin JC, Pujol S, Bauer C, Jennings D, Fennessy F, Sonka M, Buatti J, Aylward S, Miller JV, Pieper S, and Kikinis R. 3D Slicer as an image computing platform for the Quantitative Imaging Network. Magnetic Resonance Imaging 2012 Nov; 30:1323–41. DOI: 10.1016/j.mri.2012.05.001
51. Klein S, Staring M, Murphy K, Viergever M, and Pluim J. elastix: A Toolbox for Intensity-Based Medical Image Registration. IEEE Transactions on Medical Imaging 2010 Jan; 29:196–205. DOI: 10.1109/TMI.2009.2035616
52. Shamonin D, Bron E, Lelieveldt B, Smits M, Klein S, and Staring M. Fast Parallel Image Registration on CPU and GPU for Diagnostic Classification of Alzheimer's Disease. Frontiers in Neuroinformatics 2014; 7. DOI: 10.3389/fninf.2013.00050. Available from: https://www.frontiersin.org/articles/10.3389/fninf.2013.00050
53. Le Bihan D. What can we see with IVIM MRI? NeuroImage 2019 Feb; 187:56–67. DOI: 10.1016/j.neuroimage.2017.12.062. Available from: https://linkinghub.elsevier.com/retrieve/pii/S1053811917310868
54. Koh DM, Collins DJ, and Orton MR. Intravoxel Incoherent Motion in Body Diffusion-Weighted MRI: Reality and Challenges. American Journal of Roentgenology 2011 Jun; 196:1351–61. DOI: 10.2214/AJR.10.5515. Available from: http://www.ajronline.org/doi/10.2214/AJR.10.5515
55. Szubert-Franczak AE, Naduk-Ostrowska M, Pasicz K, Podgórska J, Skrzyński W, and Cieszanowski A. Intravoxel incoherent motion magnetic resonance imaging: basic principles and clinical applications. Polish Journal of Radiology 2020; 85:624–35. DOI: 10.5114/pjr.2020.101476. Available from: https://www.termedia.pl/doi/10.5114/pjr.2020.101476
56. Parker GJ, Roberts C, Macdonald A, Buonaccorsi GA, Cheung S, Buckley DL, Jackson A, Watson Y, Davies K, and Jayson GC. Experimentally-derived functional form for a population-averaged high-temporal-resolution arterial input function for dynamic contrast-enhanced MRI. Magnetic Resonance in Medicine 2006 Nov; 56:993–1000. DOI: 10.1002/mrm.21066. Available from: https://onlinelibrary.wiley.com/doi/10.1002/mrm.21066
57. Tofts PS, Brix G, Buckley DL, Evelhoch JL, Henderson E, Knopp MV, Larsson HB, Lee TY, Mayr NA, Parker GJ, Port RE, Taylor J, and Weisskoff RM. Estimating kinetic parameters from dynamic contrast-enhanced t1-weighted MRI of a diffusable tracer: Standardized quantities and symbols. Journal of Magnetic Resonance Imaging 1999 Sep; 10:223–32. DOI: 10.1002/(SICI)1522-2586(199909)10:3<223::AID-JMRI2>3.0.CO;2-S. Available from: https://onlinelibrary.wiley.com/doi/10.1002/(SICI)1522-2586(199909)10:3%3C223::AID-JMRI2%3E3.0.CO;2-S

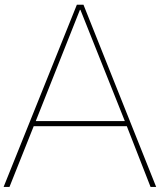

PET and multiparametric MRI for Head and Neck Cancer, Literature review

Positron Emission Tomography and Multiparametric Magnetic Resonance Imaging for Head and Neck Cancer

Literature Review

by

E.H.M. Kemper

Leiden-Delft-Erasmus Alliance | Erasmus Medical Center

Student number: 4548221
Date: July 6, 2022

Universiteit Leiden The Netherlands

TU Delft Delft University of Technology

Erasmus University Rotterdam

Erasmus MC University Medical Center Rotterdam

Abstract

Positron emission tomography with magnetic resonance imaging (PET-MRI) is increasingly used as a non-invasive diagnostic tool for characterisation and staging of head and neck tumours. The MR imaging is mainly used as anatomical reference for the PET imaging. Additional physiological MRI sequences might aid in the diagnosis for the head and neck tumour. Therefore, the aim of this review is to describe the clinical potential of physiological MRI sequences for characterisation and staging in PET-MR imaging of head and neck tumours based on the current literature.

18F-fluorodeoxy-D-glucose ((18)F-FDG) PET has a high sensitivity for detection of nodal or distant metastasis. However, characterisation or staging of the primary tumour has been shown to be difficult with (18)F-FDG due to the non-specificity of metabolic uptake with the characterisation or staging of tumours. Diffusion weighted imaging (DWI) and dynamic contrast enhanced (DCE)-MRI were better able to differentiate malignancy from inflammation compared to (18)F-FDG PET. Staging of the primary tumour with DWI and DCE-MRI has been studied and provided inconstant results for the correlations between the DWI and DCE-MRI and T-stage of the tumour. Tumour location and keratinization grade were required to increase the correlation between physiological MRI and tumour T-stage. In combined DWI, DCE-MRI and (18)F-FDG models, for each individual modality, specific parameters improved the overall performance of the model for detection, characterisation, and staging.

Thus, the DWI, DCE-MRI and (18)F-FDG parameters provide complementary information concerning the characterisation and staging of head and neck cancers. A multiparametric model combining DWI, DCE-MRI and (18)F-FDG PET parameters will most likely improve the accuracy of characterisation and staging of head and neck cancers compared to each individual physiological MRI or PET parameter.

Introduction

Worldwide 900.000 new cases of head and neck cancer and 450.000 deaths are described annually [1]. Within Europe head and neck cancer accounts for approximately 4 percent of all new cancer cases [2]. The head and neck region include multiple vital functions. Therefore, head and neck cancer has a high impact on the quality of life (QOL) of patients. Facial deformation due to the presence or absence of the tumour can result in a long-lasting need for physical and mental support. Furthermore, trouble swallowing, breathing, or speaking results in stress and a reduction in QOL. Early detection and complex multidisciplinary treatments can reduce the impact of the head and neck cancer. Thereby reducing the impact on the QOL and length of rehabilitation. [3]

The risk for head and neck cancer is highly related to lifestyle and the anatomical location. Major risk factors associated with head and neck cancer include smoking, alcohol consumption, human papillomavirus (HPV), and Epstein-Barr virus (EBV) infection [4].

To better predict the course of the tumour, head and neck cancer is divided into subcategories based on their anatomical location. A head and neck cancer can be located in the oral cavity, nasopharynx, oropharynx, hypopharynx, larynx, nasal cavity, paranasal sinuses, or salivary glands (Figure A.1a). For each subcategory, the number of new cases in 2020 are provided in Table A.1.

Table A.1. Incidence of head and neck cancers in 2020.

	Europe [7]	Worldwide [1]
Oral cavity	39.766	377.713
Nasopharynx	3.778	133.354
Oropharynx	18.926	98.412
Hypopharynx	11.243	84.254
Larynx	24.633	184.615
Nasal cavity and paranasal sinuses	-	-
Salivary glands	6.187	53.583

Besides the anatomical location, head and neck cancer can also be differentiated by the histopathological origin. These include squamous cell carcinomas (SCC), verrucous carcinoma, adenocarcinoma, adenoid cystic carcinoma, and mucoepidermoid carcinoma. SCC accounts for 90% to 95% of head and neck cancers [8]. This tumour type can be further categorised into three differentiations based on the amount of keratinization: well differentiated (> 75% keratinization), moderately differentiated (25-75% keratinization), and poorly differentiated (<25% keratinization).

The American Joint Committee on Cancer (AJCC) staging classification is used to define the tumour stage [9]. The staging consists of a T-, N-, and M-stage describing the extend of the primary tumour, involvement of regional lymph nodes, and presence of distant metastasis, respectively. The TNM stage descriptions are specified for each anatomical location. Each cancer can be placed in one of the stage groups 0, I, II, III, or IV. Figure A.1b shows the level system to describe the location of lymph nodes involved with the head and neck cancer. [6] Currently, two-thirds of head and neck cancers are at clinical presentation in an advanced TNM stage (III/IV). These patients often already have regional metastatic lymph nodes. [9]

Recently, Wunschel et al. [10] determined that Union for International Cancer Control (UICC) cancer staging and AJCC pathology based (p)T-staging were most significant predictors of overall survival and tumour recurrence followed by depth of invasion, metastatic lymph node presence and keratinization grade. The TNM staging combined with the tumour type and anatomical location determines the choice of treatment such as, chemotherapy, radiotherapy, surgery or a combination of these treatment options.

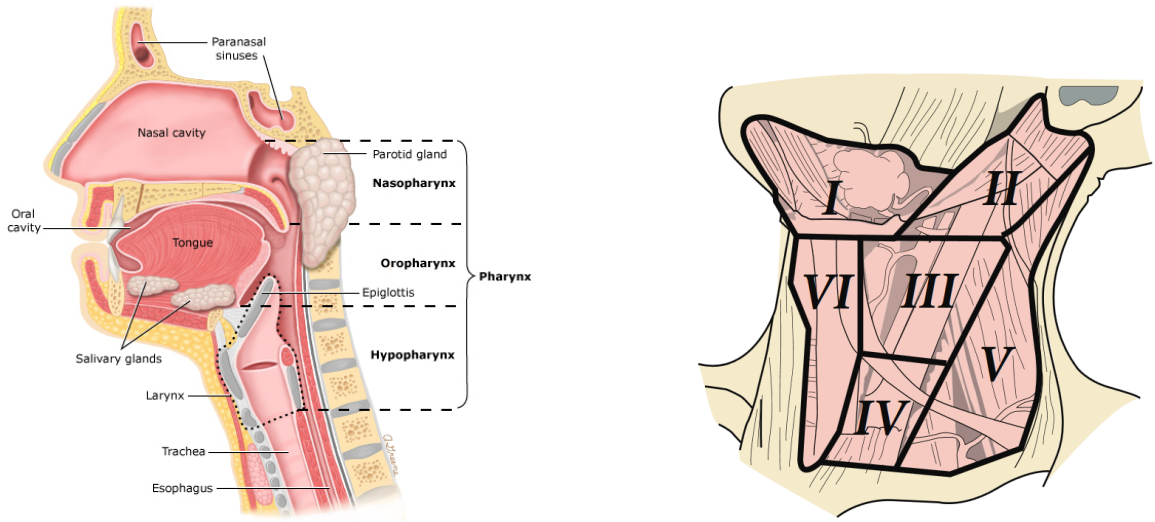

(a) (b)

Figure A.1. Anatomical categorisations in head and neck cancers. *(a)* Subcategories based on the anatomical location of the tumour. Adapted from: Overview of the diagnosis and staging of head and neck cancer (2022). UpToDate ®[5]. *(b)* The level system for describing the location of lymph nodes in the neck: Level I, submental and submandibular group; Level II, upper jugular group; Level III, middle jugular group; Level IV, lower jugular group; Level V, posterior triangle group; Level VI, anterior compartment. Adapted from: Deschler Daniel G, Moore Michael G, and Smith Richard V [6]

Diagnosis and staging are mainly determined by biopsy and imaging. The diagnosis for cancer is often determined by biopsy of the lesion. Imaging can show the presence and extent of a primary tumour or possible metastasis. Positron emission tomography (PET) with integrated computed tomography (CT) is the established imaging modality for detection and staging of head and neck cancer. Hybrid PET-magnetic resonance imaging (MRI) is an alternative for PET-CT. When the lesions are located close to the surface of the body, also panendoscopy is sometimes used.

For imaging of head and neck cancers the radioactive tracer 18F-fluorodeoxy-D-glucose ((18)F-FDG) is mainly used. (18)F-FDG uptake relates to the glucose metabolism of tissues. In head and neck cancers (18)F-FDG PET is performed for detection of nodal and distant metastatic disease, optimising guided radiation therapy for tumour control and treatment response, and detection of occult primary tumours, second primary tumours or cancers of unknown primary. Generally, increased (18)F-FDG uptake correlates with an increased metabolism which in turn is highly indicative of malignant activity. [11, 12]

The CT is added to the PET to correlate increased uptake of the PET to anatomical locations visible on the CT images. The high spatial resolution and anatomical information provided by the CT combined with the high sensitivity of PET to increased metabolic activity improves the accuracy of the combined PET-CT for detecting primary lesion and local or distant metastasis compared to standalone PET or CT. [13]

MRI is able to image anatomical structures with a higher spatial resolution than CT. The better soft tissue contrast of structural MRI compared to the CT is useful in the complex soft tissues of the head and neck. The fusion of PET and MRI has proven to provide similar or increased accuracy of lesion detection compared to PET-CT. [14, 15, 16]

Currently, in PET-MRI for head and neck tumour imaging structural MR images are commonly acquired to support the findings of the (18)F-FDG PET. However, MRI sequences which image physiological processes are only limited implemented in the daily practice of European clinics, even though it might further improve the PET-MRI characterisation and staging of head and neck cancers [17]. Significant correlations have been found between (18)F-FDG PET parameters and those derived from physiolog-

ical MRI sequences [18, 19, 20]. Also, multiple studies have been performed to relate physiological MRI parameters with the characterisation and staging of head and neck cancers. Thus far, results reported in the literature differ widely. However, review studies providing a comparison of results or general overview of physiological MRI performed thus far in the characterisation and staging head and neck cancers are limited.

Therefore, the aim of this review is to describe the clinical potential of physiological MRI sequences for characterisation and staging in PET-MR imaging of head and neck tumours based on the current literature. The focus will be on the most frequently used physiological MRI techniques in this specific patient population. A description of the physiological MRI sequences will be provided. A through search will be performed in Medline to retrieve clinical trails describing the characterisation and staging capability of (18)F-FDG PET and physiological MRI for head and neck tumours. The performance of each imaging modality will be summarised and compared to one another. Relevant physiological MRI parameters and combined models that have been applied for characterisation and staging will be provided.

Imaging of head and neck cancer

PET (18)F-FDG

The use of (18)F-FDG PET for characterisation and staging in head and neck cancer has been extensively investigated. A multitude of systematic research and meta-analysis have described the advantages and limitations of (18)F-FDG PET.

The high sensitivity of (18)F-FDG PET to detect an increased metabolic uptake have been shown to increase the diagnostic accuracy for staging of head and neck cancer. The TNM-stage of head and neck cancers significantly improved to correlate with clinical and histological findings when using (18)F-FDG PET in addition to CT or ultrasound imaging [21, 22]. Furthermore, (18)F-FDG PET increased the incidence of distant metastases and second primary tumours with 18.7%, revealing important findings for treatment decision making [23].

The main limitations of (18)F-FDG PET include the lower spatial resolution and the variable physiological FDG uptake in the dense and complex anatomic structures of the head and neck or inflammatory lesions that can obscure the tumour tissue [12, 24]. The non-specificity of an elevated (18)F-FDG uptake for malignancy can be described as the main reason for these limitations. Although malignant tumours have often an increased metabolic activity, several other process which increase metabolic activity and thereby (18)F-FDG uptake exist [25]. Therefore, (18)F-FDG uptake is also unable to differentiate benign from malignant tumours [26]. The addition of volumetric information of tumours in order to calculate (18)F-FDG volumetric imaging biomarkers has been suggested to improve the prediction of the clinical outcome in head and neck SCC patients compared to the SUVmax of the tumour [27].

Anatomical localisation with CT is used to determine the physiological origin of the FDG uptake. These PET/CTs can be achieved with a low dose CT protocol which minimises the radiation exposure to the patient. However, for most head and neck cancers a diagnostic CT is part of the diagnostic work-up. Therefore, most CT imaging performed in a PET-CT for head and neck cancer are diagnostic. These diagnostic CTs are of higher image quality compared to low-dose CTs and are to be used for diagnostic characterisation of pathologic processes. They provide additional information concerning the extent of local tumour spread, tumour stage and characterisation [13]. Additionally, a high quality diagnostic CT is of increased importance in head and neck imaging for good fusion, due to the complex anatomy, to provide accurate correlation between the (18)F-FDG and CT image. [25].

(18)F-FDG PET is highly sensitivity in detection of nodal and distant metastasis [28, 22]. Major improvement has been found for per-neck-level detection of local lymph node metastasis with a sensitivity increase of 21% when using (18)F-FDG PET/CT over conventional Imaging (CT, MRI, and CT/MRI) [29]. Furthermore, the use of (18)F-FDG PET/CT or MRI have been shown to lead to a significant change in the N classification of head and neck tumours compared to ultrasound fine needle aspiration cytology, especially in advanced nodal disease (>N2a) [23, 21].

The lower spatial resolution of (18)F-FDG PET does limit the sensitivity for detection of smaller nodal or distant metastasis. lymph nodes <3mm have been shown to increase the number of false negatives significantly. Thus, a N0 neck cannot be adequately evaluated by 18F-FDG PET, owing to its rather low negative predictive value (NPV) (about 80%) [27]. (18)F-FDG PET image acquisition is recommended for evaluation of the head and neck cancer prior to performing image guided biopsy and (18)F-FDG PET-CT is recommended for surgical treatment planning and follow-up. [28, 30, 31]

PET-MRI resulted in an equal or higher accuracy in characterisation and staging of head and neck cancers compared to PET-CT. The reduced radiation exposure of PET-MRI compared to PET-CT has increased the interest and use of PET-MRI in daily practice. Although, high cost and reduced patient capacity due to longer imaging times have limit the number of PET-MRI systems in clinical use. Therefore, PET-CT is still the standard PET imaging method in most clinics. [14, 15, 16]

physiological MRI

Specific combinations of RF pulses and magnetic gradients can result in an MR image representing physiological effects within the body. In the development of the MRI, multiple of these physiological MRI sequences have been discovered. Their value has been evaluated in several clinical disciplines with varying success. Also, in head and neck imaging common physiological MRI have been investigated for their functionality.

Research into the clinical application of physiological MRI sequences for head and neck cancer is still limited. Thus far, most research in physiological MRI sequences has been for brain and neurological imaging. Applications of physiological MRI in head and neck cancers are mostly pilots and small-scale trails. Diffusion weighted imaging (DWI) and dynamic contrast enhanced (DCE)-MRI have been investigated most extensively. Therefore, this review will focus on describing the clinical potential of DWI and DCE-MRI.

DWI

DWI is an MRI technique that uses the diffusion of water molecules within a tissue to generate contrast in MR images. This diffusion is caused by the Brownian motion of molecules. However, their diffusion might be hindered depending on their surroundings. For example, other molecules or cell walls and can limit the diffusion. [20, 32]. A higher cellularity results in the restriction of water movement. Therefore, less diffusion and a higher DWI signal. Low level of cellularity results in an increased water movement. Thus, more diffusion and a reduced DWI signal. Often cancers have a higher cellularity. Therefore, their DWI signal is increased compared to the surrounding tissue. Necrotic tissue often has a lower cellularity, lowering its DWI signal.

Imaging technique

DWI sequences consist of an excitation pulse, diffusion dephasing gradient, 180 rephasing pulse and diffusion rephasing gradient followed by the signal read-out. The combined diffusion dephasing and rephasing gradients induce no dephasing for stationary water molecules. The echo generated after the 180 rephasing pulse will have a maximum intensity if the water molecules have remained stationary. However, movement of the water molecules during and in between the diffusion gradients will cause the water molecules to experience more dephasing and generate a reduced echo after 180 rephasing pulse. DWI values are the signal intensities measured from the 180 rephasing echo. Thus, a lower signal intensity of a diffusion weighted image indicates a higher diffusion rate. [32]

A commonly used technique to acquire a diffusion weighted image is single-shot spin-echo echo planar imaging (SS-SE-EPI). EPI refers to the use of a frequency- and phase-encoding gradients to generate a high number of echoes from a single excitation pulse. The encoding follows a zig-zag pattern to fill the k-space with data from each echo. Single-shot refers to the use of a single excitation pulse to fill the whole k-space with data. Spin-echo describes the use of a 180 refocusing pulse to generate an echo.

The applied strength and timing of the diffusion gradients is described by the b-value. A higher b-value increases the strength and/or time the gradient is applied. A b-value of 0 refers to no gradient applied. The diffusion effect within a tissue is depended on the applied gradient. The relation between diffusion and b-value is mostly linear but differs between tissues. The apparent diffusion coefficient (ADC) describes the linear relation between the diffusion and b-values. The ADC is determined by at least two, but often three, b-values between 0 and 1000 sec/mm^2. This can be done voxel-wise, generating an ADC map. [33, 34, 35] Movement of water caused by microcirculation in the tissue is of similar magnitude as the diffusion of water within the tissue. Therefore, the DWI captures both the microcirculation and diffusion. Combined diffusion and microcirculation effects within a tissue can be modelled using Intravoxel incoherent motion (IVIM) with a bi-exponential decay model (Figure A.2). This model provides the diffusion attenuation D and the pseudodiffusion attenuation D^*. D^* represents the pseudodiffusion effects caused by blood flow of the microcirculation in the capillary. The faster water movement of the microcirculation compared to tissue diffusion results in a faster decay of the MRI signal. Therefore, the microcirculation only significantly effects the DWI signal at low b-values. The fraction of D to D^* is given by f. [36, 37, 38]

$$S/S_0 = f exp[-b(D^* + D_{blood})] + (1-f) exp(-bD_{tissue}) \tag{A.1}$$

Although IVIM appears to determine the diffusion of water molecules in tissue more accurately, other issues are described [37]. Equation A.1 assumes a gaussian diffusion of the water molecules, however it is determined not to be the case. To model the deviation a kurtosis coefficient K can be added to the model, Diffusion kurtosis imaging (DKI). The deviation increases with an increasing b-value as shown in Figure A.2. Furthermore, base level noise can cause overestimation of the non-gaussian

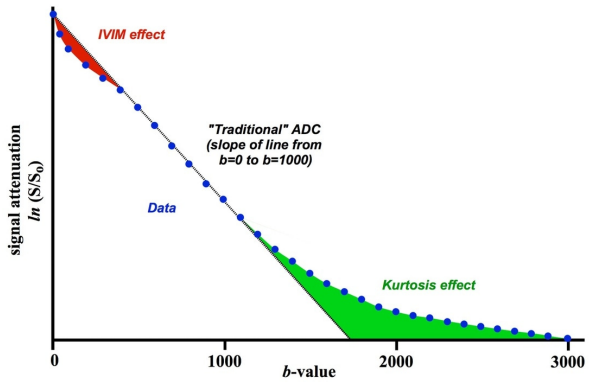

Figure A.2. Deviation of the expected MR signal in DWI from a mono-exponential model. At low b-values IVIM effects due to microscopic perfusion must be considered (red), while at high b-values kurtosis effects must be considered (green). Adapted from: *IVIM Imaging - What is intravoxel incoherent motion (IVIM)? Is this the same as diffusion?* [39]

deviation at low signals. A correction can be applied. These additional parameters can be described as Equation A.2. IVIM and DKI should provide a more accurate measurement of the actual diffusion within the tissue.

$$S/S_O = \{[f exp(-bD^*) + (1-f) exp[-bD + (bD)^2 K/6]]^2 + NCF\}^{1/2} \quad \text{(A.2)}$$

K = Kurtosis diffusion model, NCF = noise correction factor

Clinical evaluation

Multiple trails have been performed to relate clinical outcomes with DWI and diffusion parameters. Correlations with diffusion parameters have been studied for the detection of lesions in specific head and neck regions, differentiation of tumour grade for both the primary tumour and lymph nodes, N-staging of lymph nodes, detection of HPV-status, detection of hypoxia, and detection of necrotic centres of lesions.

Detection

Detection of malignancies is the first step in staging and characterisation of tumours. Staging and characterisation with diffusion imaging becomes unlikely when tumours are indistinguishable from normal tissue within the diffusion imaging. For the detection of primary tumours, DWI and IVIM have shown the ability for a good differentiation between normal muscle tissue and malignancies. Tshering Vogel et al. [40] have been able to detect seventeen out of eighteen patients with a tumour based on combined conventional MRI and DWI. The tumour of the remaining one patient did not show diffusion restriction, and therefore did not provide contrast with the surrounding normal muscle tissue. ADC_{mean}, D and D^* parameters have been shown to be able to differentiate benign from malignant tumours [41, 14, 15, 42, 43].

Only Sakamoto et al. [44] were unable to differentiate benign from malignant tumours using DWI parameters. ADC may be able to differentiate lymphomas from carcinomas. However, there is a high possibility that this difference is mainly based on the presence or absence of necrosis in malignant and benign lesions, respectively. Variability of D^* measured by Xu et al. [42] could have been the result of imaging at different cardiac phases [45]. Therefore, distinguishing benign from malignant tumours based on D^* may result in a lower accuracy compared to other diffusion measures.

Tumour recurrence has been detected using DWI despite increased inflammation surrounding the treated region. ADC, f and D have been shown to differentiate recurring tumour from surrounding tissues [40, 46]. The best performance has been achieved using ADC_{mean} (AUC 0.83-0.85), which was similar to the SUV_{mean} (AUC 0.85) [46]. DWI has been described as an excellent method to detect

recurrence of head and neck tumours.

Characterisation

In the nasopharynx and oropharynx regions, DWI and IVIM parameters have been shown to differentiate carcinomas from lymphomas [47, 48]. Interestingly, Yu et al. [47] have been able to differentiate (non-keratinized) nasopharyngeal carcinomas (NPC) from lymphomas using ADC and fxD^*, while Ichikawa et al. [48] have not been able to show this using the ADC. NPCs are often described separately due to their distinct epidemiology and treatment [49, 50, 51]. Ichikawa et al. [48] have shown significantly different ADC values between keratinized oropharynx carcinomas and lymphomas. Keratinized oropharynx carcinomas showed necrosis, which highly influences ADC values [51, 52]. Necrosis in metastatic nodes has also been shown to significantly alter ADC values compared to non necrotic metastatic nodes. [53] Furthermore, f is highly linked to the echo time (TE) and repetition time (TR). [54]

Lymphoma is believed to be composed of condensed tumour cells with little cytoplasm, scarce amounts of stroma and necrosis, in contrast to NPC. For DWI this results in lower D and ADC values [47]. NPC usually presents with abundant vessels and hyperperfusion, therefore resulting in higher perfusion linked D^* values. Lymphomas are associated with poor perfusion.

A selection of articles have described the ability to differentiate tumours by keratinization grade with ADC [55, 56, 48]. Primary tumours have been differentiated with ADC values between low (1 or 2) and high keratinization grade (3 or 4). However, Leifels et al. [57] and Fruehwald-Pallamar et al. [58] have found no difference between low and high keratinization grade. Nakajo et al. [59] and Ichikawa et al. [48] have measured ADC to differentiate the primary tumours between grade 1 and 2 and did not find a significant difference. No obvious reasons were stated for the inconsistent keratinization grading with ADC. Tumour location might have influenced the results, since a wide variate of tumour locations have been used in these studies. A more probable explanation might have been found by Ichikawa et al. [48]. They made a distinction between tumours with a homogeneous or heterogeneous T2-weighted signal intensity. Only the low keratinization grade tumours with T2w homogeneity had a significantly lower ADC value than high keratinization grade tumours with T2w homogeneous. Low keratinization grade tumours with T2 heterogeneity had no significantly lower ADC values compared to high keratinization grades with T2w heterogeneity. The tumours with T2w heterogeneity were pathologically confirmed to be caused by tumour necrosis. Most articles avoided necrotic areas during tumour delineation [55, 56, 48, 58]. Notably, Leifels et al. [57] did not specify the presence of necrotic areas, which could have decreased the ADC differences between keratinization grades. Thus, these results indicate that ADC might be able to differentiate tumour keratinization grade if necrosis of the tumour is taken into account.

HPV status of head and neck tumours influences diffusion parameters of the tumour [60, 61, 62]. HPV-negative tumours have shown significant higher diffusion (ADC_{mean}, D) and lower microcirculation (f, D^*) values compared to HPV-positive tumours. These differences have been detected in primary tumours and lymph nodes [60, 62, 61]. Contrary, Chawla et al. [63] have found no significant differences of DWI parameters between HPV-status. Chawla et al. [63] have included a high number of HPV-negative tumours not located in the oropharynx compared to the other described studies. HPV-positive SCC are commonly located in the oropharynx. Therefore, the diffusion parameters of Chawla et al. [63] could be influenced by factors associated with anatomical position rather than HPV-status, blurring the correlation of HPV-status with diffusion parameters.

Staging

The development of the primary tumour is mainly described by UICC T-stage. A higher T-stage is related to an increased aggression of the tumour. T-stages are mainly described by the interactions of the tumour with the surrounding structures. These changes during the development of a tumour can be reflected by changes in the diffusion and microcirculation of the tumour. Significant differences between DWI parameters according to the tumour T-stage were inconsistent between studies. Multiple studies have found no significant difference for ADC between T-stages [55, 56, 57, 59, 64]. While other studies have correlated the ADC to tumour stages [60, 65, 66, 67]. Large studies from Tang et al. [66] and Zhang et al. [67] have compared low (T1, T2) with high (T3, T4) tumour stage and found a difference for ADC_{mean} and tumour infiltration using DWI. Martens et al. [60] have not found a significant

difference between T-stages using ADC_{mean}, however, ADC gross tumour volume (ADC_{GTV}), D, f and D^* were significantly different between T-stages. A possible cause of these different findings between studies is the heterogeneous inclusion of tumour histopathological subcategory. The tumours included by Zhang et al. [67] were mostly NPCs. Tang et al. [66] only included oral tongue SCC lesions. Both were able to differentiate T-stage with diffusion parameters. While the recent studies of Dang et al. [55] and Freihat et al. [56] have included multiple head and neck subcategories and could not differentiate the T-stage with diffusion parameters. Concluding, the T-staging of tumours based on DWI parameters provided various results. It is probable that T-staging can be achieved, but the tumour location and keratinization grade should be taken into account.

The evaluation of local lymph nodes for malignancy with DWI can be performed by direct delineation of a suspected lymph node or by predicting the N-stage based on the diffusion values of the primary tumour. No significant increase in the detection of lymph nodes have been found when including DWI to an (18)F-FDG PET with conventional MRI. [68] However, a higher sensitivity for subcentimetric node detection has been found for DWI compared with only conventional MRI [69]. The prediction of the N-stage of the primary tumour by ADC has shown mixed results. The majority of studies have not been able to correlate ADC to N-stage. [57, 65, 56, 59] Holzapfel et al. [70] and Martens et al. [60] have correlated ADC to the N-stage of the tumour. Ren, Yuan, and Tao [71] have correlated histogram parameters of the ADC to the tumour N-stage. Detection of local malignant lymph nodes and distant metastasis with at least a diameter of 5 mm is possible due to the difference in diffusion parameter values between malignant and normal muscle tissue. However, predicting N-stage based on the diffusion parameters of the primary tumour has been shown to be difficult.

DCE-MRI

Perfusion MRI enables the measurement of the movement of blood within the body. Perfusion MRI provides an indication of the permeability for blood to enter and exit tissues. To measure this permeability, contrast is injected into the bloodstream. Dynamic MR images can be acquired during gadolinium (Gd) based MRI contrast injection into the patient. Imaging of the T1 shortening caused by Gd-based contrast agent is called DCE-MRI. DCE-MRI provides time-intensity curves per voxel. From these time-intensity curves (semi-) quantitative perfusion and permeability parameters can be derived.

Image technique

A DCE-MRI sequence dynamically acquires T1w images during injection of a Gd-based contrast agent. Each T1w scan during the dynamic acquisition takes only a few seconds. The DCE-MRI sequence can result in more than 40 T1w images over a span of 5 or more minutes. Within the period imaged by DCE-MRI, the Gd-based contrast agent arrives (wash-in), saturates (peak enhancement) and leaves (wash-out) the tissue as shown in Figure A.3a. Semi-quantitative perfusion parameters for tissues can be derived from the time intensity curve. Commonly calculated semi-quantitative parameters include:

- Wash-in rate (WiR), Wash-out rate (WoR)
- Peak enhancement ratio (PER)
- (Initial) area under the contrast curve ($(i)AUC$)
- Time to peak (TTP)

Several additional imaging sequences are required for a quantitative analysis of perfusion parameters. A pre-contrast T1-map is required to determine a base line signal intensity of the tissue. Measurement of the arterial input function (AIF) is required for nearly all quantitative parameter calculations. The AIF measures the contrast concentration in a major artery. Thereby, the proportion of contrast intravascular versus extravascular can be calculated. [72, 73] Pharmacokinetic modelling is a commonly used quantitative analysis for permeability mapping. It models the exchange between compartments in tissue (Figure A.3b). The main calculated parameters are:

- K_{trans}, a transfer constant for the passage of contrast from plasma to the extravascular-extracellular space (EES). K_{trans} should represent the combined effect of plasma blood flow, permeability and capillary surface area.
- K_{ep}, refers to the constant for the passage of plasma from EES to the blood plasma.
- V_p, the volume of the blood plasma.
- V_e, the volume of the EES.

The provided list is incomplete. Additional parameters can determine based on the DCE-MRI acquisitions. These describe measures such as tracer concentration, total blood volume, and perfusion and permeability of different structures.

Temporal resolution of the DCE-MRI acquisition describes the scan time of each individual T1w image volume during the dynamic imaging. A higher temporal resolution decreases motion blur of the image and increases the accuracy of the quantitative analysis, however at the cost of spatial resolution and a decrease in signal-to-noise ratio. Ideal temporal resolutions described for head and neck imaging are less than 5 seconds per image [72]. The dynamic acquisition is recommended for at least 7 min in case AIF is based on a predefined model. In case the AIF needs to be measured, acquisition up to 10 min might be needed to achieve adequate return from the EES. These recommendations are based on DCE imaging of the brain. Typical DCE-MRI acquisitions for head and neck are 5-8 min. [74, 73, 72] Additional non-weighted T1w imaging could be obtained to determine B1 maps for field in-homogeneity correction. [72]

Clinical evaluation

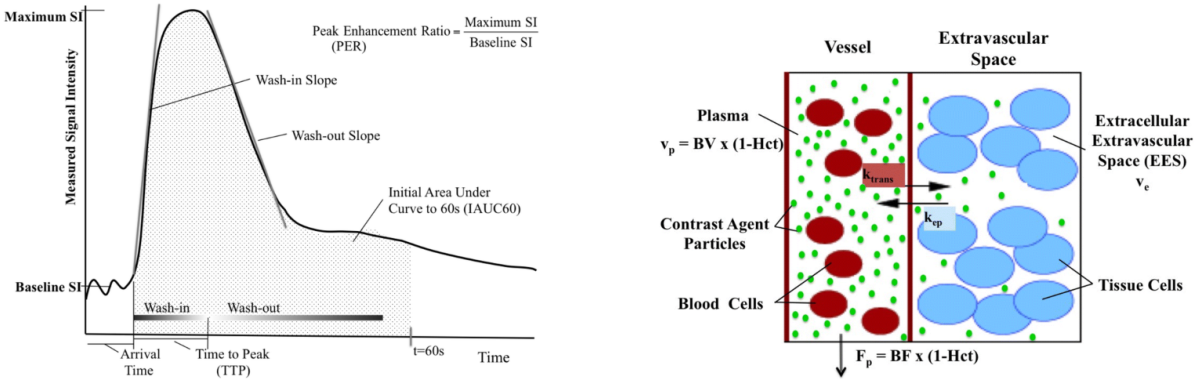

Figure A.3. ***(a)*** **Example of a DCE-MRI time-intensity curve. Multiple semi-quantitative parameters that can be derived from the time-intensity curve have been depicted.** ***(b)*** **Illustration of the principal perfusion and permeability mapping parameters. Perfusion mapping evaluates the quantity of blood within a given volume of tissue (blood volume — BV) and the volumetric flow rate of blood (BF). Permeability mapping relates the exchange of Gd-based contrast agent between the blood plasma, that has a volume v_p, and the extravascular-extracellular space (EES) having volume v_e. A transfer constant k_{trans} describes the passage from plasma to EES, while the constant k_ep controls the reverse process. Adapted from: Petralia et al. [72]**

Detection

The detection of malignant tumour with DCE-MRI has been investigated by multiple studies. Furukawa et al. [75] have been able to differentiate tumour from normal muscle tissue using semi-quantitative parameters such as TTP. Quantitative parameters K_{trans}, K_{ep}, V_e and $iAUC$ have been shown to be higher in tumour compared to normal muscle tissue [14, 15, 76, 77, 78]. Only Xu et al. [42] have not found significantly different DCE-MRI parameters for tumour compared to normal muscle tissue. A study by Cheng et al. [79] has been able to differentiate benign from malignant lesion using parameters derived from the DCE-MRI histograms of the tumour. Furthermore, several studies were able to predict tumour recurrence after treatment with DCE-MRI parameters V_e and $K_{trans-skewness}$. [80, 81, 81] Thus, the differentiation between malignant and normal muscle tissue appears highly possible with multiple calculated DCE-MRI parameters.

Characterisation

DCE-MRI parameters have been investigated to differentiate keratinization grade, several histopathological tumour types, and HPV-status. All studies differentiating keratinization grade with DCE-MRI parameter came to similar conclusions. For low compared to high keratinization grade no difference have been determined based on any (semi-)quantitative DCE-MRI parameter. [55, 57, 65]

Differentiation of histopathological tumour type using DCE-MRI parameters has been performed for lymphomas, SCC and undifferentiated (UD) carcinomas. Based on DCE-MRI parameter the perfusion of these tumour types was significantly different in specific cases. SCCs have been distinguished from lymphomas by DCE-MRI parameters K_{trans}, V_e or the maximum contrast intensity (IC_{max}) [82, 83]. However, Lee et al. [84] have also measured K_{trans} and V_e and found no significant differences between SCCs and lymphomas. They could only differentiate UD carcinomas from SCC and lymphomas. The primary tumours included in the described studies had various anatomical locations. As discussed previously in the review, NPCs are known to be histopathologically different from other SCCs. Most tumours included by Park et al. [82] were SCCs originating in the tonsils, the remaining originated from the tongue. Lee et al. [84] have included NPCs, SCCs and lymphomas mostly located in the hypopharynx, tonsil, or oral cavity. Thus, Lee et al. [84] have differentiated NPCs from SCC and lymphomas with DCE-MRI parameter which is less surprising but a useful observation. However, this does not explain the different observations for differentiating SCC and lymphomas with DCE-MRI parameters. Park et al. [82] had noticed a higher heterogeneity of V_e tumour values in their SCC group with relative similar anatomical origin compared to lymphomas. The heterogeneity described by $V_{e-kurtosis}$ was

more discriminative between SCC and lymphomas compare to V_e. Lee et al. [84] have measured the heterogeneity of the semi-quantitative AUC parameter but have not calculated the $AUC_{kurtosis}$ parameter. However, visually the AUC heterogeneity of the lymphomas appears more leptokurtic compared to the SCC. Therefore, both studies show a possibility to differentiate lymphomas from SCC by calculation of the perfusion kurtosis parameter.

Between HPV-negative and HPV-positive tumours $V_{e-kurtosis}$ has been found to be different [85]. Other studies have not found a significant difference for any (semi-)quantitative DCE-MRI parameter to differentiate HPV-negative from HPV-positive tumours. [60, 61, 62, 63] Therefore, HPV-status is unlikely to affect the DCE-MRI parameters.

Staging

The inconsistency in correlating T-stage with DWI parameters continuous for the correlation with DCE-MRI parameters. Multiple clinical trials have been performed to distinguish high T-stage tumours from low T-stage tumours based on a significantly higher tissue permeability. Three studies [65, 57, 55] have been unable to measure a significant difference, while others have found a significant difference in DCE-MRI parameters [60, 86, 78] However, the specific parameters that were found to be significantly different were inconsistent. Liu et al. [86] have measured significant differences between low and high T-stage NPCs with semi-quantitative DCE-MRI parameters PER or PER related parameters. One study [78] have found significant correlation between T-stage and the DCE-MRI parameters K_{ep} and V_e. And another study [60] has found DCE gross tumour volume (DCE_{GTV}) was significantly different between T-stages. Also, the depth of tumour invasion measured on DCE-MRI has been shown to significantly correlate with T-stage for oral and tongue SCC [66].

Important to note is that Martens et al. [60] included patients with HNSCC in oropharynx and hypopharynx, while Zheng et al. [78] and Liu et al. [86] only included NPC. Therefore, two distinct types of carcinomas have been compared. Furthermore, different HPV statuses were included which is shown to influences the staging for DWI parameters. Nevertheless, it is not likely this will influence the staging for DCE-MRI as thus far no correlation has been found between DCE-MRI and HPV status.

Additional inconsistencies in studies results have been found in tumour staging for the prediction of N-stage by measuring DCE-MRI parameters of the primary tumour. Liu et al. [86] determined no correlation exists between semi-quantitative DCE parameters and N-stage but quantitative DCE-MRI parameters K_{ep} has been correlated to tumour N-stage by several studies [57, 78, 87]. Although, Martens et al. [60] and Bülbül et al. [65] have not found that correlation. Martens et al. [60] have found a correlation for V_e with tumour N-stage. N-stage determined by the DCE-MRI parameters of a measurable lymph node show a better correlation compared to the indirect measurement of the primary tumour. The semi-quantitative DCE-MRI parameters TTP, WiR, relative enhancement (RE), $RE_{maximum}$ and the quantitative DCE-MRI parameter DCE_{GTV} have been correlated to malignant or benign lymph nodes. [88, 60] K_{trans} of the primary tumour has been found predicable for M-stage. [78] Thus far, staging with DCE-MRI has been highly contradicting. However, DCE-MRI parameters can provide useful information for TNM staging.

Multiparametric MRI

Multiparametric MRI refers to the combined use of parameters derived from multiple MRI sequences. The parameters should provide an ideal combination of data to determine a given clinical evaluation. It is possible to include all MRI sequences that individually contribute to an increased performance for characterisation and staging of head and neck tumours. However, this would be inefficient if the MRI sequence does not provide addition information compared to other MRI sequences or (18)F-FDG PET. Therefore, it is of interest to determine correlations between MRI and PET parameters in the characterisation and staging of head and neck cancers. Furthermore, individual MRI parameters are assessed in combined models to determine if and how much a parameter contributes to a higher performance of the overall model.

Correlation between MRI and PET parameters

Individual physiological parameters of DWI and DCE-MRI have been correlated to PET parameters and to each other. Correlations between parameters provide insights in the overlap of information measured by the different parameters. PET parameters that have been used for the correlation include SUV and parameters describing tumour size based on (18)F-FDG PET uptake, such as metabolic tumour volume (MTV) and total lesion glycolysis (TLG).

DCE-MRI vs DWI

Theoretically, ADC and D^* only partially describe the perfusion of a tissue. Correlations between the perfusion imaging of DCE-MRI and diffusion imaging might exist if the perfusion effect measured with ADC or D^* are significant. V_e has been correlated with ADC [65, 57, 89]. Furthermore, Covello et al. [15] and Cavaliere et al. [14] have correlated ADC_{mean} with $K_{trans-mean}$ within tumours and therefore linked a high cell density (low ADC) with an increased permeability of the tumour due to neoangiogenesis (high K_{trans}). Thus far no correlations have been found between DCE-MRI and IVIM parameters. [90]

DCE-MRI vs PET

Correlations have been found between $iAUC$ and V_e with SUV [65, 76]. Furthermore, K_{trans} has been correlated with SUV in the primary tumour by Bülbül et al. [65] and Gawlitza et al. [91] and in lymph nodes by Vidiri et al. [85]. Only Surov et al. [92] have correlated K_{ep} with SUV_{max} and Leifels et al. [57] and Han et al. [89] have found no correlation between DCE-MRI parameters and SUV. Vidiri et al. [85] remarked that the discrepancies in these results might be caused by the differences in tumour homogeneity and grade. They stated that their research is similar to that of Bisdas et al. [76] but unlike Bisdas et al. [76] they were unable to correlate V_e with SUV. Therefore, still limited evidence exists that correlates DCE-MRI and PET parameters.

DWI vs PET

The correlation of ADC parameters with SUV has been studied more extensively compared to other physiological MRI parameters. However only two studies [59, 65] have been able to correlate ADC_{mean} with SUV_{max} while most other studies did not find a correlation [46, 57, 58, 64, 91, 94, 95, 96, 97, 93]. On a voxel-wise level, ADC and SUV values have been correlated [94, 95, 98, 99]. Furthermore, Han et al. [89] have correlated TLG to ADC_{min} and more recently Zhang et al. [93] have correlated MTV with ADC_{mean}. Thus, contextual information of the tumour, such as tumour volume, seems to be necessary to correlated DWI to PET. Additionally, geometric distortions in DWI imaging have been shown to significantly impact the correlations between DWI and PET. Correct preparation and correction of the DWI and PET is required to achieve correct interpretation of the DWI and PET correlation [100].

Multiparametric models

All previously described correlations of physiological MRI parameters were based on the individual parameters. A selection of multiple parameters can provide detailed and unique descriptors for the detection, characterisation and staging of tumours.

Detection

Detection of lesions with DWI has been studied using multiparametric models. According to Sakamoto et al. [41] the combined D, D^* model resulted in the highest detection of malignancy compared to benign lesions. The combined D, D^* model resulted in a higher diagnostic ability than ADC alone. A combined $ADC_{kurtosis-mean}$, ADC_{mean} and time intensity curve model improved diagnostic accuracy for differentiating benign from malignant lesions compared to the parameters individually [79]. Kim et al. [101] have shown that the combination of SUV and ADC could predicted post treatment failure most accurate. Only MTV as an individual parameter could do this similarly well.

Characterisation

The accuracy for predicting low from high keratinization grade tumours has been improved by the combined regression model of Dang et al. [55]. The highest individual parameter of ADC_{mean} had an AUC of 0.64, where the combined SUV, ADC, and $K_{ep-mean}$ model increased the AUC to 0.84.

Staging

So far multiparametric models for T-staging head and neck tumour could not be found. An ADC_{10th}, $ADC_{uniformity}$, and $WiR_{skewness}$ model has been shown to predict occult lymph node metastases based on the primary tumour with a higher accuracy than the independent DWI or DCE-MRI parameters [71]. Treutlein et al. [77] has determined that lymph node diameter is the best individual predictor for malignancy in small lymph nodes. A multiparametric model of anatomical and DCE-MRI parameters did increase predictability for lymph node malignancy.

All described multiparametric models have shown to improve the performance of individual parameters, indicating most modalities provide complementary information concerning characterisation and staging of head and neck cancers.

Discussion

The aim of this review was to describe the clinical potential of physiological MRI sequences for staging and characterisation of head and neck tumours. Results from studies using DWI and DCE-MRI for detection, characterisation and staging purposes were summarised. The performance of the quantitative parameters in differentiating the tumours often provided inconsistent results between studies. Still, several correlations have shown substantial evidence.

Detection of lesions can be done with a high accuracy using both DWI and DCE-MRI imaging. ADC_{mean}, D, D^*, K_{trans}, K_{ep}, V_e and $iAUC$ all could be used for tumour detection. The tumours could be differentiated from normal muscle tissue and benign tumours. The main limitation that has been described was the minimal size of the lesion required for the detection. Furthermore, tumour recurrence could be predicted by DWI despite increased inflammation surrounding the region of treatment, which is beneficial for the differentiation of inflammation and malignancies detected by (18)F-FDG.

Thus far, research performed with large homogeneous groups of SCC is lacking for characterisation and staging. The smaller study populations of the described articles have correlated multiple physiological MRI parameters to tumour characterisation and staging but provide limited evidence. For example, T-stage could be detected by several studies, but no consensus has been found. Possible culprits include heterogeneity of tumour location, histopathological subcategories, and keratinization grade. DCE-MRI parameters have been correlated to T-stage, but unfortunately the parameters were not similar between studies.

Both N- and M-staging showed even less correlations with DCE-MRI or DWI. DCE-MRI and DWI parameters of the primary tumour are minimally altered in tumours with a high N- or M-stages compared to a low N- or M-stage. Determination of N- or M-stage can be done more accurately by the detection of the individual malignant lymph nodes or distance metastasis rather than predictions based on the primary tumour. Still, this remains difficult due to the smaller size of both lymph nodes and metastasis. Furthermore, the signal of metastatic lymph nodes adjacent to the primary tumour can be obscured by the signal of the primary tumour.

Studies determining the effects of HPV-status on the tumour DWI and DCE-MRI values have provided consequent results. HPV-status has been shown to significantly alter DWI. Contrary, HPV-positive and HPV-negative lesions have not shown differences using DCE-MRI. HPV-positive SCC were often oropharyngeal SCC. Differentiation of keratinization grade can be done with a moderate performance using ADC. DCE-MRI did not correlate to the keratinization grade.

The differentiation between lymphomas, SCC and NPCs and T- and N-staging of head and neck cancer with DWI and DCE-MRI parameters have provided contradicting results. The studies described limited reasons for the discrepancies between their and other studies. A reason often described is the heterogeneity of head and neck tumour subcategories included in the study. Some subcategories of head and neck cancer show quite different epidemiology and characteristics. Studies performing characterising and staging of tumours based on the subcategories NPCs, SCC and lymphomas appear to be able to better differentiate the head and neck tumours from their surroundings. Heterogeneity of the tumour tissue also influences the characterisation and staging capabilities of physiological MRI. Correlations between T2w heterogeneity of the tumour tissue and the predictive value of DWI has been determined. Physiological explanations for the DWI alterations that have been described included necrosis, inflammation, and to some extent tumour keratinization.

Overall, several correlations between physiological MRI and tumour characterisation and staging have been described. However, the value of each detected correlation is difficult to determine. The studies were inconsistent in their methodology and presentation of results. Standardising the research methodology would be beneficial for comparing research. The writing of a standardised method to measure the performance of physiological MRI in characterisation and staging of head and neck cancers is out

of the scope of this review. Nevertheless, recommendations for further research can be made about the sequences that should be acquired, and which parameters should be calculated.

When both ADC values and IVIM parameters were measured, D closely correlated to ADC. Furthermore, D^* often provided additional information which improved overall performance of detection, characterisation, and staging. ADC is a useful measurement on its own but additional IVIM parameters are of increased value and should be preferred. Between the semi-quantitative and quantitative measurements of DCE-MRI, quantitative measurements are preferred. The semi-quantitative $iAUC$ parameters has shown correlation to tumour detection, but so did quantitative parameters K_{trans}, K_{ep} and V_e. These three quantitative parameters most often correlated with characterisation and staging and are better comparable between patients compared to semi-quantitative measures.

No physiological MRI parameter provided identical information to (18)F-FDG PET. Furthermore, SUV values have shown to increase the accuracy of combined PET-MRI models for characterisation or staging of head and neck tumours [55, 101]. Also, the SUV parameters can help to reduce the complexity of the correlations between physiological MRI and the characterisation and staging of head and neck tumour. Therefore, a multiparametric model for tumour characterisation and staging should include physiological MRI and (18)F-FDG PET.

Additionally, the use of parameters derived from physiological MRI tumour histograms increased the performance of the tumours characterisation, staging and differentiation [71, 79, 81, 82, 85, 87]. Therefore, these histogram parameters are more likely to correlate physiological MRI with tumour characterisation and staging. Also, anatomical information acquired with conventional MRI have shown to provide valuable information about the size and shape of a potential tumour. These tumour characteristics have been related to the tumour stage. For example, T2w has a high accuracy in detection of lymph node metastases [102].

Each imaging sequence in a combined (18)F-FDG PET, anatomical and physiological MRI model seems to hold complementary information for the characterisation and staging of head and neck tumours. Thus, a multiparametric model can increase the performance of models lacking (18)F-FDG PET, anatomical or physiological MR imaging.

Specific parameters derived from physiological MRI appear more predictive than others. Compared to ADC, IVIM parameters D and D^* were more predictive in a multiparametric model for detection of malignant lymph nodes [41]. Moreover, ADC provide overlapping information with several other DCE-MRI and PET parameters while IVIM parameters provided complementary information to that of DCE-MRI and PET. Therefore, IVIM parameters D and D^* have a higher potential to be of added value in a multiparametric model for tumour characterisation or staging compared to ADC. DCE-MRI parameter K_{ep} has been correlated to T- and N-stage and has been shown to differentiate malignant from benign tumours. Furthermore, K_{ep} was not correlated with other parameters, indicating limited informational overlap. Increased performance of the combined model to differentiate tumour grades provide additional evidence to select K_{ep} in an multiparametric model over other DCE parameters [55]. K_{trans} and V_e have shown correlations for tumour characterisation and staging. However, V_e is also correlated with other parameters such as ADC and SUV. Therefore, V_e provides less distinctive information.

Concluding, physiological MRI can improve characterisation and staging of head and neck cancer. However, no single sequence could provide better performance than (18)F-FDG PET with conventional MRI. Based on the findings in current literature, DWI and DCE-MRI parameters provide complementary information concerning the characterisation and staging of head and neck cancers. A multiparametric model combining DWI, DCE-MRI and (18)F-FDG PET parameters will most likely improve the accuracy of characterisation and staging of head and neck cancers compared to each individual physiological MRI or PET parameter.

Bibliography

1. International Agency for Research on Cancer. Global Cancer Observatory. 2020. Available from: https://gco.iarc.fr/
2. Gatta G et al. Prognoses and improvement for head and neck cancers diagnosed in Europe in early 2000s: The EUROCARE-5 population-based study. European Journal of Cancer 2015 Oct; 51:2130–43. DOI: 10.1016/j.ejca.2015.07.043. Available from: https://linkinghub.elsevier.com/retrieve/pii/S0959804915007492
3. Nelke K, Pawlak W, Gerber H, and Leszczyszyn J. Head and Neck Cancer Patients' Quality of Life. Advances in Clinical and Experimental Medicine 2014 Nov; 23:1019–27. DOI: 10.17219/acem/37361. Available from: http://www.advances.umed.wroc.pl/en/article/2014/23/6/1019/
4. Cohen N, Fedewa S, and Chen AY. Epidemiology and Demographics of the Head and Neck Cancer Population. Oral and maxillofacial surgery clinics of North America 2018 Nov; 30:381–95. DOI: 10.1016/j.coms.2018.06.001. Available from: https://linkinghub.elsevier.com/retrieve/pii/S1042369918300530
5. Poon CS and Stenson KM. Overview of the diagnosis and staging of head and neck cancer - UpToDate. 2022. Available from: https://www.uptodate.com/contents/overview-of-the-diagnosis-and-staging-of-head-and-neck-cancer
6. Deschler Daniel G, Moore Michael G, and Smith Richard V. Quick Reference Guide to TNM Staging of Head and Neck Cancer and Neck Dissection Classification. American Academy of Otolaryngology-Head and Neck Surgery Foundation 2014
7. European Cancer Information System. Incidence and mortality estimates 2020. 2020. Available from: https://ecis.jrc.ec.europa.eu/index.php
8. Skarsgard DP, Groome PA, Mackillop WJ, Zhou S, Rothwell D, Dixon PF, O'Sullivan B, Hall SF, and Holowaty EJ. Cancers of the upper aerodigestive tract in Ontario, Canada, and the United States. Cancer 2000 Apr; 88:1728–38. DOI: 10.1002/(SICI)1097-0142(20000401)88:7<1728::AID-CNCR29>3.0.CO;2-7. Available from: https://onlinelibrary.wiley.com/doi/10.1002/(SICI)1097-0142(20000401)88:7%3C1728::AID-CNCR29%3E3.0.CO;2-7
9. Argiris A, Karamouzis MV, Raben D, and Ferris RL. Head and neck cancer. Lancet (London, England) 2008 May; 371:1695–709. DOI: 10.1016/S0140-6736(08)60728-X. Available from: https://linkinghub.elsevier.com/retrieve/pii/S014067360860728X
10. Wunschel M, Neumeier M, Utpatel K, Reichert TE, Ettl T, and Spanier G. Staging more important than grading? Evaluation of malignancy grading, depth of invasion, and resection margins in oral squamous cell carcinoma. Clinical Oral Investigations 2021 Mar; 25:1169–82. DOI: 10.1007/s00784-020-03421-2. Available from: https://link.springer.com/10.1007/s00784-020-03421-2
11. Hohenstein NA, Chan JW, Wu SY, Tahir P, and Yom SS. Diagnosis, Staging, Radiation Treatment Response Assessment, and Outcome Prognostication of Head and Neck Cancers Using PET Imaging: A Systematic Review. PET clinics 2020 Jan; 15:65–75. DOI: 10.1016/j.cpet.2019.08.010. Available from: https://linkinghub.elsevier.com/retrieve/pii/S155685981930080X
12. Castaldi P, Leccisotti L, Bussu F, Micciché F, and Rufini V. Role of (18)F-FDG PET-CT in head and neck squamous cell carcinoma. Acta otorhinolaryngologica Italica : organo ufficiale della Societa italiana di otorinolaringologia e chirurgia cervico-facciale 2013 Feb; 33:1–8. Available from: http://www.ncbi.nlm.nih.gov/pubmed/23620633
13. Ryan JL, Aaron VD, and Sims JB. PET/MRI vs PET/CT in Head and Neck Imaging: When, Why, and How? Seminars in Ultrasound, CT and MRI 2019 Oct; 40:376–90. DOI: 10.1053/J.SULT.2019.07.002

14. Cavaliere C, Romeo V, Aiello M, Mesolella M, Iorio B, Barbuto L, Cantone E, Nicolai E, and Covello M. Multiparametric evaluation by simultaneous PET-MRI examination in patients with histologically proven laryngeal cancer. European Journal of Radiology 2017 Mar; 88:47–55. DOI: 10.1016/j.ejrad.2016.12.034. Available from: https://linkinghub.elsevier.com/retrieve/pii/S0720048X16304284
15. Covello M, Cavaliere C, Aiello M, Cianelli M, Mesolella M, Iorio B, Rossi A, and Nicolai E. Simultaneous PET/MR head–neck cancer imaging: Preliminary clinical experience and multiparametric evaluation. European Journal of Radiology 2015 Jul; 84:1269–76. DOI: 10.1016/j.ejrad.2015.04.010. Available from: https://linkinghub.elsevier.com/retrieve/pii/S0720048X15001849
16. Chan SC, Yeh CH, Yen TC, Ng SH, Chang JTC, Lin CY, Yen-Ming T, Fan KH, Huang BS, Hsu CL, Chang KP, Wang HM, and Liao CT. Clinical utility of simultaneous whole-body 18F-FDG PET/MRI as a single-step imaging modality in the staging of primary nasopharyngeal carcinoma. European Journal of Nuclear Medicine and Molecular Imaging 2018 Jul; 45:1297–308. DOI: 10.1007/s00259-018-3986-3. Available from: https://link.springer.com/article/10.1007/s00259-018-3986-3
17. Manfrini E, Smits M, Thust S, Geiger S, Bendella Z, Petr J, Solymosi L, and Keil VC. From research to clinical practice: a European neuroradiological survey on quantitative advanced MRI implementation. European Radiology 2021 Aug; 31:6334–41. DOI: 10.1007/s00330-020-07582-2. Available from: https://link.springer.com/10.1007/s00330-020-07582-2
18. Huellner MW. PET/MR in Head and Neck Cancer – An Update. Seminars in Nuclear Medicine 2021 Jan; 51:26–38. DOI: 10.1053/j.semnuclmed.2020.07.006. Available from: https://linkinghub.elsevier.com/retrieve/pii/S0001299820300775
19. Jansen JF, Parra C, Lu Y, and Shukla-Dave A. Evaluation of Head and Neck Tumors with Functional MR Imaging. Magnetic Resonance Imaging Clinics of North America 2016 Feb; 24:123–33. DOI: 10.1016/j.mric.2015.08.011. Available from: https://linkinghub.elsevier.com/retrieve/pii/S1064968915001099
20. Nooij RP, Hof JJ, Laar PJ van, and Hoorn A van der. Functional MRI for Treatment Evaluation in Patients with Head and Neck Squamous Cell Carcinoma: A Review of the Literature from a Radiologist Perspective. Current Radiology Reports 2018 Jan; 6:2. DOI: 10.1007/s40134-018-0262-z. Available from: http://link.springer.com/10.1007/s40134-018-0262-z
21. Pedraza S, Ruiz-Alonso A, Hernández-Martínez AC, Cabello E, Lora D, and Pérez-Regadera JF. 18F-FDG PET/CT in staging and delineation of radiotherapy volume for head and neck cancer. Revista Española de Medicina Nuclear e Imagen Molecular (English Edition) 2019 May; 38:154–9. DOI: 10.1016/j.remnie.2018.08.003. Available from: https://linkinghub.elsevier.com/retrieve/pii/S225380891830079X
22. Gao S, Li S, Yang X, and Tang Q. 18FDG PET-CT for distant metastases in patients with recurrent head and neck cancer after definitive treatment. A meta-analysis. Oral Oncology 2014 Mar; 50:163–7. DOI: 10.1016/j.oraloncology.2013.12.002. Available from: https://linkinghub.elsevier.com/retrieve/pii/S1368837513007689
23. Stadler TM, Morand GB, Rupp NJ, Hüllner MW, and Broglie MA. FDG-PET-CT/MRI in head and neck squamous cell carcinoma: Impact on pretherapeutic N classification, detection of distant metastases, and second primary tumors. Head & neck 2021 Jul; 43:2058–68. DOI: 10.1002/hed.26668. Available from: https://onlinelibrary.wiley.com/doi/10.1002/hed.26668
24. McCollum AD, Burrell SC, Haddad RI, Norris CM, Tishler RB, Case MA, Posner MR, and Van den Abbeele AD. Positron emission tomography with 18F-fluorodeoxyglucose to predict pathologic response after induction chemotherapy and definitive chemoradiotherapy in head and neck cancer. Head & neck 2004 Oct; 26:890–6. DOI: 10.1002/hed.20080. Available from: https://onlinelibrary.wiley.com/doi/10.1002/hed.20080
25. Pijl JP, Nienhuis PH, Kwee TC, Glaudemans AW, Slart RH, and Gormsen LC. Limitations and Pitfalls of FDG-PET/CT in Infection and Inflammation. Seminars in Nuclear Medicine 2021 Nov; 51:633–45. DOI: 10.1053/j.semnuclmed.2021.06.008. Available from: https://linkinghub.elsevier.com/retrieve/pii/S0001299821000404

26. Kwee TC, Cheng G, Lam MG, Basu S, and Alavi A. SUVmax of 2.5 should not be embraced as a magic threshold for separating benign from malignant lesions. European Journal of Nuclear Medicine and Molecular Imaging 2013 40:10 2013 Jun; 40:1475–7. DOI: 10.1007/S00259-013-2484-X. Available from: https://link.springer.com/article/10.1007/s00259-013-2484-x
27. Manca G, Vanzi E, Rubello D, Giammarile F, Grassetto G, Wong KK, Perkins AC, Colletti PM, and Volterrani D. 18F-FDG PET/CT quantification in head and neck squamous cell cancer: principles, technical issues and clinical applications. European Journal of Nuclear Medicine and Molecular Imaging 2016 Jul; 43:1360–75. DOI: 10.1007/s00259-015-3294-0. Available from: http://link.springer.com/10.1007/s00259-015-3294-0
28. Marcus C, Sheikhbahaei S, Shivamurthy VKN, Avey G, and Subramaniam RM. PET Imaging for Head and Neck Cancers. Radiologic Clinics of North America 2021 Sep; 59:773–88. DOI: 10.1016/j.rcl.2021.05.005. Available from: https://linkinghub.elsevier.com/retrieve/pii/S003383892100066X
29. Sun R, Tang X, Yang Y, and Zhang C. 18FDG-PET/CT for the detection of regional nodal metastasis in patients with head and neck cancer: A meta-analysis. Oral Oncology 2015 Apr; 51:314–20. DOI: 10.1016/j.oraloncology.2015.01.004. Available from: https://linkinghub.elsevier.com/retrieve/pii/S1368837515000056
30. Sheikhbahaei S, Marcus C, and Subramaniam RM. 18F FDG PET/CT and Head and Neck Cancer: Patient Management and Outcomes. PET clinics 2015 Apr; 10:125–45. DOI: 10.1016/j.cpet.2014.12.001. Available from: https://linkinghub.elsevier.com/retrieve/pii/S1556859814001333
31. Sanli Y, Zukotynski K, Mittra E, Chen DL, Nadel H, Niederkohr RD, and Subramaniam RM. Update 2018: 18F-FDG PET/CT and PET/MRI in Head and Neck Cancer. Clinical nuclear medicine 2018 Dec; 43:e439–e452. DOI: 10.1097/RLU.0000000000002247. Available from: https://journals.lww.com/00003072-201812000-00020
32. Connolly M and Srinivasan A. Diffusion-Weighted Imaging in Head and Neck Cancer: Technique, Limitations, and Applications. Magnetic Resonance Imaging Clinics of North America 2018 Feb; 26:121–33. DOI: 10.1016/j.mric.2017.08.011. Available from: https://linkinghub.elsevier.com/retrieve/pii/S1064968917300995
33. Chilla GS, Tan CH, Xu C, and Poh CL. Diffusion weighted magnetic resonance imaging and its recent trend-a survey. Quantitative imaging in medicine and surgery 2015 Jun; 5:407–22. DOI: 10.3978/j.issn.2223-4292.2015.03.01. Available from: https://qims.amegroups.com/article/view/5938/7029
34. Malayeri AA, El Khouli RH, Zaheer A, Jacobs MA, Corona-Villalobos CP, Kamel IR, and Macura KJ. Principles and Applications of Diffusion-weighted Imaging in Cancer Detection, Staging, and Treatment Follow-up. RadioGraphics 2011 Oct; 31:1773–91. DOI: 10.1148/rg.316115515. Available from: http://pubs.rsna.org/doi/10.1148/rg.316115515
35. Park MY and Byun JY. Understanding the mathematics involved in calculating apparent diffusion coefficient maps. American Journal of Roentgenology 2012 Dec; 199. DOI: 10.2214/AJR.12.9231
36. Le Bihan D. What can we see with IVIM MRI? NeuroImage 2019 Feb; 187:56–67. DOI: 10.1016/j.neuroimage.2017.12.062. Available from: https://linkinghub.elsevier.com/retrieve/pii/S1053811917310868
37. Koh DM, Collins DJ, and Orton MR. Intravoxel Incoherent Motion in Body Diffusion-Weighted MRI: Reality and Challenges. American Journal of Roentgenology 2011 Jun; 196:1351–61. DOI: 10.2214/AJR.10.5515. Available from: http://www.ajronline.org/doi/10.2214/AJR.10.5515
38. Szubert-Franczak AE, Naduk-Ostrowska M, Pasicz K, Podgórska J, Skrzyński W, and Cieszanowski A. Intravoxel incoherent motion magnetic resonance imaging: basic principles and clinical applications. Polish Journal of Radiology 2020; 85:624–35. DOI: 10.5114/pjr.2020.101476. Available from: https://www.termedia.pl/doi/10.5114/pjr.2020.101476
39. IVIM Imaging - What is intravoxel incoherent motion (IVIM)? Is this the same as diffusion? Available from: https://mriquestions.com/ivim.html
40. Tshering Vogel DW, Zbaeren P, Geretschlaeger A, Vermathen P, De Keyzer F, and Thoeny HC. Diffusion-weighted MR imaging including bi-exponential fitting for the detection of recurrent or

residual tumour after (chemo)radiotherapy for laryngeal and hypopharyngeal cancers. European Radiology 2013 Feb; 23:562–9. DOI: 10.1007/s00330-012-2596-x. Available from: http://link.springer.com/10.1007/s00330-012-2596-x

41. Sakamoto J, Imaizumi A, Sasaki Y, Kamio T, Wakoh M, Otonari-Yamamoto M, and Sano T. Comparison of accuracy of intravoxel incoherent motion and apparent diffusion coefficient techniques for predicting malignancy of head and neck tumors using half-Fourier single-shot turbo spin-echo diffusion-weighted imaging. Magnetic Resonance Imaging 2014 Sep; 32:860–6. DOI: 10.1016/j.mri.2014.05.002. Available from: https://linkinghub.elsevier.com/retrieve/pii/S0730725X1400174X
42. Xu XQ, Choi YJ, Sung YS, Yoon RG, Jang SW, Park JE, Heo YJ, Baek JH, and Lee JH. Intravoxel Incoherent Motion MR Imaging in the Head and Neck: Correlation with Dynamic Contrast-Enhanced MR Imaging and Diffusion-Weighted Imaging. Korean Journal of Radiology 2016 Oct; 17:641. DOI: 10.3348/kjr.2016.17.5.641. Available from: https://www.kjronline.org/DOIx.php?id=10.3348/kjr.2016.17.5.641
43. Ai QY, King AD, Chan JSM, Chen W, Chan KCA, Woo JKS, Zee BCY, Chan ATC, Poon DMC, Ma BBY, Hui EP, Ahuja AT, Vlantis AC, and Yuan J. Distinguishing early-stage nasopharyngeal carcinoma from benign hyperplasia using intravoxel incoherent motion diffusion-weighted MRI. European Radiology 2019 Oct; 29:5627–34. DOI: 10.1007/s00330-019-06133-8. Available from: http://link.springer.com/10.1007/s00330-019-06133-8
44. Sakamoto J, Yoshino N, Okochi K, Imaizumi A, Tetsumura A, Kurohara K, and Kurabayashi T. Tissue characterization of head and neck lesions using diffusion-weighted MR imaging with SPLICE. European Journal of Radiology 2009 Feb; 69:260–8. DOI: 10.1016/j.ejrad.2007.10.008. Available from: https://linkinghub.elsevier.com/retrieve/pii/S0720048X07005268
45. Federau C, Hagmann P, Maeder P, Müller M, Meuli R, Stuber M, and O'Brien K. Dependence of Brain Intravoxel Incoherent Motion Perfusion Parameters on the Cardiac Cycle. PLoS ONE 2013 Aug; 8. Ed. by Hendrikse J:e72856. DOI: 10.1371/journal.pone.0072856. Available from: https://dx.plos.org/10.1371/journal.pone.0072856
46. Becker M, Varoquaux AD, Combescure C, Rager O, Pusztaszeri M, Burkhardt K, Delattre BMA, Dulguerov P, Dulguerov N, Katirtzidou E, Caparrotti F, Ratib O, Zaidi H, and Becker CD. Local recurrence of squamous cell carcinoma of the head and neck after radio(chemo)therapy: Diagnostic performance of FDG-PET/MRI with diffusion-weighted sequences. European Radiology 2018 Feb; 28:651–63. DOI: 10.1007/s00330-017-4999-1. Available from: https://link.springer.com/article/10.1007/s00330-017-4999-1
47. Yu XP, Hou J, Li FP, Wang H, Hu PS, Bi F, and Wang W. Intravoxel Incoherent Motion Diffusion Weighted Magnetic Resonance Imaging for Differentiation Between Nasopharyngeal Carcinoma and Lymphoma at the Primary Site. Journal of Computer Assisted Tomography 2016; 40:413–8. DOI: 10.1097/RCT.0000000000000391. Available from: http://journals.lww.com/00004728-201605000-00015
48. Ichikawa Y, Sumi M, Sasaki M, Sumi T, and Nakamura T. Efficacy of Diffusion-Weighted Imaging for the Differentiation between Lymphomas and Carcinomas of the Nasopharynx and Oropharynx: Correlations of Apparent Diffusion Coefficients and Histologic Features. American Journal of Neuroradiology 2012 Apr; 33:761–6. DOI: 10.3174/ajnr.A2834. Available from: http://www.ajnr.org/lookup/doi/10.3174/ajnr.A2834
49. Sumi M and Nakamura T. Diagnostic importance of focal defects in the apparent diffusion coefficient-based differentiation between lymphoma and squamous cell carcinoma nodes in the neck. European Radiology 2009 Apr; 19:975–81. DOI: 10.1007/s00330-008-1217-1. Available from: http://link.springer.com/10.1007/s00330-008-1217-1
50. King AD, Ahuja AT, Yeung DKW, Fong DKY, Lee YYP, Lei KIK, and Tse GMK. Malignant Cervical Lymphadenopathy: Diagnostic Accuracy of Diffusion-weighted MR Imaging. Radiology 2007 Dec; 245:806–13. DOI: 10.1148/radiol.2451061804. Available from: http://pubs.rsna.org/doi/10.1148/radiol.2451061804
51. Lang P, Wendland MF, Saeed M, Gindele A, Rosenau W, Mathur A, Gooding CA, and Genant HK. Osteogenic sarcoma: noninvasive in vivo assessment of tumor necrosis with diffusion-weighted MR imaging. Radiology 1998 Jan; 206:227–35. DOI: 10.1148/radiology.206.

1.9423677. Available from: http://pubs.rsna.org/doi/10.1148/radiology.206.1.9423677

52. Lyng H, Haraldseth O, and Rofstad EK. Measurement of cell density and necrotic fraction in human melanoma xenografts by diffusion weighted magnetic resonance imaging. Magnetic Resonance in Medicine 2000 Jun; 43:828–36. DOI: 10.1002/1522-2594(200006)43:6<828::AID-MRM8>3.0.CO;2-P. Available from: https://onlinelibrary.wiley.com/doi/10.1002/1522-2594(200006)43:6%3C828::AID-MRM8%3E3.0.CO;2-P
53. Zhang Y, Chen J, Shen J, Zhong J, Ye R, and Liang B. Apparent diffusion coefficient values of necrotic and solid portion of lymph nodes: Differential diagnostic value in cervical lymphadenopathy. Clinical Radiology 2013 Mar; 68:224–31. DOI: 10.1016/j.crad.2011.04.002. Available from: https://linkinghub.elsevier.com/retrieve/pii/S0009926011001619
54. Lemke A, Laun FB, Simon D, Stieltjes B, and Schad LR. An in vivo verification of the intravoxel incoherent motion effect in diffusion-weighted imaging of the abdomen. Magnetic Resonance in Medicine 2010 Dec; 64:1580–5. DOI: 10.1002/mrm.22565. Available from: https://onlinelibrary.wiley.com/doi/10.1002/mrm.22565
55. Dang H, Chen Y, Zhang Z, Shi X, Chen X, Zhu X, Hou B, Xing H, Xue H, and Jin Z. Application of integrated positron emission tomography/magnetic resonance imaging in evaluating the prognostic factors of head and neck squamous cell carcinoma with positron emission tomography, diffusion-weighted imaging, dynamic contrast enhancement and combined model. Dento maxillo facial radiology 2020 Jul; 49:20190488. DOI: 10.1259/dmfr.20190488. Available from: https://www.birpublications.org/doi/10.1259/dmfr.20190488
56. Freihat O, Zoltán T, Pinter T, Kedves A, Sipos D, Repa I, Kovács Á, and Zsolt C. Correlation between Tissue Cellularity and Metabolism Represented by Diffusion-Weighted Imaging (DWI) and 18F-FDG PET/MRI in Head and Neck Cancer (HNC). Cancers 2022 Feb; 14:847. DOI: 10.3390/cancers14030847. Available from: https://www.mdpi.com/2072-6694/14/3/847
57. Leifels L, Purz S, Stumpp P, Schob S, Meyer HJ, Kahn T, Sabri O, and Surov A. Associations between 18 F-FDG-PET, DWI, and DCE Parameters in Patients with Head and Neck Squamous Cell Carcinoma Depend on Tumor Grading. Contrast Media & Molecular Imaging 2017; 2017:1–8. DOI: 10.1155/2017/5369625. Available from: https://www.hindawi.com/journals/cmmi/2017/5369625/
58. Fruehwald-Pallamar J, Czerny C, Mayerhoefer ME, Halpern BS, Eder-Czembirek C, Brunner M, Schuetz M, Weber M, Fruehwald L, and Herneth AM. Functional imaging in head and neck squamous cell carcinoma: correlation of PET/CT and diffusion-weighted imaging at 3 Tesla. European Journal of Nuclear Medicine and Molecular Imaging 2011 Jun; 38:1009–19. DOI: 10.1007/s00259-010-1718-4. Available from: http://link.springer.com/10.1007/s00259-010-1718-4
59. Nakajo M, Nakajo M, Kajiya Y, Tani A, Kamiyama T, Yonekura R, Fukukura Y, Matsuzaki T, Nishimoto K, Nomoto M, and Koriyama C. FDG PET/CT and Diffusion-Weighted Imaging of Head and Neck Squamous Cell Carcinoma: Comparison of Prognostic Significance Between Primary Tumor Standardized Uptake Value and Apparent Diffusion Coefficient. Clinical Nuclear Medicine 2012 May; 37:475–80. DOI: 10.1097/RLU.0b013e318248524a. Available from: https://journals.lww.com/00003072-201205000-00008
60. Martens RM, Koopman T, Lavini C, Ali M, Peeters CFW, Noij DP, Zwezerijnen G, Marcus JT, Vergeer MR, Leemans CR, Bree R de, Graaf P de, Boellaard R, and Castelijns JA. Multiparametric functional MRI and 18F-FDG-PET for survival prediction in patients with head and neck squamous cell carcinoma treated with (chemo)radiation. European Radiology 2021 Feb; 31:616–28. DOI: 10.1007/s00330-020-07163-3. Available from: https://link.springer.com/10.1007/s00330-020-07163-3
61. Han M, Lee S, Lee D, Kim S, and Choi J. Correlation of human papilloma virus status with quantitative perfusion/diffusion/metabolic imaging parameters in the oral cavity and oropharyngeal squamous cell carcinoma: comparison of primary tumour sites and metastatic lymph nodes. Clinical Radiology 2018 Aug; 73:21–757. DOI: 10.1016/j.crad.2018.04.005. Available from: https://linkinghub.elsevier.com/retrieve/pii/S0009926018301648
62. Piludu F, Marzi S, Gangemi E, Farneti A, Marucci L, Venuti A, Benevolo M, Pichi B, Pellini R, Sperati F, Covello R, Sanguineti G, and Vidiri A. Multiparametric MRI Evaluation of Oropharyn-

geal Squamous Cell Carcinoma. A Mono-Institutional Study. Journal of Clinical Medicine 2021 Aug; 10:3865. DOI: 10.3390/jcm10173865. Available from: https://www.mdpi.com/2077-0383/10/17/3865

63. Chawla S, Kim SG, Loevner LA, Wang S, Mohan S, Lin A, and Poptani H. Prediction of distant metastases in patients with squamous cell carcinoma of head and neck using DWI and DCE-MRI. Head & neck 2020 Nov; 42:3295–306. DOI: 10.1002/hed.26386. Available from: https://onlinelibrary.wiley.com/doi/10.1002/hed.26386
64. Surov A, Stumpp P, Meyer HJ, Gawlitza M, Höhn AK, Boehm A, Sabri O, Kahn T, and Purz S. Simultaneous 18F-FDG-PET/MRI: Associations between diffusion, glucose metabolism and histopathological parameters in patients with head and neck squamous cell carcinoma. Oral Oncology 2016 Jul; 58:14–20. DOI: 10.1016/j.oraloncology.2016.04.009. Available from: https://linkinghub.elsevier.com/retrieve/pii/S136883751630029X
65. Bülbül HM, Bülbül O, Sarıoğlu S, Özdoğan Ö, Doğan E, and Karabay N. Relationships Between DCE-MRI, DWI, and ¹⁸F-FDG PET/CT Parameters with Tumor Grade and Stage in Patients with Head and Neck Squamous Cell Carcinoma. Molecular Imaging and Radionuclide Therapy 2021 Oct; 30:177–86. DOI: 10.4274/mirt.galenos.2021.25633. Available from: http://cms.galenos.com.tr/Uploads/Article_49285/MIRT-30-177-En.pdf
66. Tang W, Wang Y, Yuan Y, and Tao X. Assessment of tumor depth in oral tongue squamous cell carcinoma with multiparametric MRI: correlation with pathology. European Radiology 2022 Jan; 32:254–61. DOI: 10.1007/s00330-021-08148-6. Available from: https://link.springer.com/10.1007/s00330-021-08148-6
67. Zhang Y, Liu X, Zhang Y, Li WF, Chen L, Mao YP, Shen JX, Zhang F, Peng H, Liu Q, Sun Y, and Ma J. Prognostic value of the primary lesion apparent diffusion coefficient (ADC) in nasopharyngeal carcinoma: a retrospective study of 541 cases. Scientific Reports 2015 Dec; 5:12242. DOI: 10.1038/srep12242. Available from: https://www.nature.com/articles/srep12242
68. Heusch P, Sproll C, Buchbender C, Rieser E, Terjung J, Antke C, Boeck I, Macht S, Scherer A, Antoch G, Heusner TA, and Handschel J. Diagnostic accuracy of ultrasound, 18F-FDG-PET/CT, and fused 18F-FDG-PET-MR images with DWI for the detection of cervical lymph node metastases of HNSCC. Clinical Oral Investigations 2014 Apr; 18:969–78. DOI: 10.1007/s00784-013-1050-z. Available from: https://link.springer.com/article/10.1007/s00784-013-1050-z
69. Vandecaveye V, De Keyzer F, Nuyts S, Deraedt K, Dirix P, Hamaekers P, Vander Poorten V, Delaere P, and Hermans R. Detection of head and neck squamous cell carcinoma with diffusion weighted MRI after (chemo)radiotherapy: Correlation between radiologic and histopathologic findings. International Journal of Radiation Oncology*Biology*Physics 2007 Mar; 67:960–71. DOI: 10.1016/j.ijrobp.2006.09.020. Available from: https://linkinghub.elsevier.com/retrieve/pii/S0360301606029890
70. Holzapfel K, Duetsch S, Fauser C, Eiber M, Rummeny EJ, and Gaa J. Value of diffusion-weighted MR imaging in the differentiation between benign and malignant cervical lymph nodes. European Journal of Radiology 2009 Dec; 72:381–7. DOI: 10.1016/j.ejrad.2008.09.034. Available from: https://linkinghub.elsevier.com/retrieve/pii/S0720048X08005147
71. Ren J, Yuan Y, and Tao X. Histogram analysis of diffusion-weighted imaging and dynamic contrast-enhanced MRI for predicting occult lymph node metastasis in early-stage oral tongue squamous cell carcinoma. European Radiology 2022 Apr; 32:2739–47. DOI: 10.1007/s00330-021-08310-0. Available from: https://link.springer.com/10.1007/s00330-021-08310-0
72. Petralia G, Summers PE, Agostini A, Ambrosini R, Cianci R, Cristel G, Calistri L, and Colagrande S. Dynamic contrast-enhanced MRI in oncology: how we do it. Radiologia Medica 2020 Dec; 125:1288–300. DOI: 10.1007/S11547-020-01220-Z/FIGURES/7. Available from: https://link.springer.com/article/10.1007/s11547-020-01220-z
73. Gordon Y, Partovi S, Müller-Eschner M, Amarteifio E, Bäuerle T, Weber MA, Kauczor HU, and Rengier F. Dynamic contrast-enhanced magnetic resonance imaging: fundamentals and application to the evaluation of the peripheral perfusion. Cardiovascular Diagnosis and Therapy 2014; 4:147. DOI: 10.3978/j.issn.2223-3652.2014.03.01. Available from: https://cdt.amegroups.com/article/view/3640/4521

74. Thrippleton MJ, Backes WH, Sourbron S, Ingrisch M, Osch MJ van, Dichgans M, Fazekas F, Ropele S, Frayne R, Oostenbrugge RJ van, Smith EE, and Wardlaw JM. Quantifying blood-brain barrier leakage in small vessel disease: Review and consensus recommendations. Alzheimer's & Dementia 2019 Jun; 15:840–58. DOI: 10.1016/J.JALZ.2019.01.013. Available from: https://onlinelibrary-wiley-com.eur.idm.oclc.org/doi/full/10.1016/j.jalz.2019.01.013%20https://onlinelibrary-wiley-com.eur.idm.oclc.org/doi/abs/10.1016/j.jalz.2019.01.013%20https://alz-journals-onlinelibrary-wiley-com.eur.idm.oclc.org/doi/10.1016/j.jalz.2019.01.013
75. Furukawa M, Parvathaneni U, Maravilla K, Richards TL, and Anzai Y. Dynamic contrast-enhanced MR perfusion imaging of head and neck tumors at 3 Tesla. Head & Neck 2013 Jul; 35:923–9. DOI: 10.1002/hed.23051. Available from: https://onlinelibrary.wiley.com/doi/10.1002/hed.23051
76. Bisdas S, Seitz O, Middendorp M, Chambron-Pinho N, Bisdas T, Vogl TJ, Hammerstingl R, Ernemann U, and Mack MG. An exploratory pilot study into the association between microcirculatory parameters derived by MRI-based pharmacokinetic analysis and glucose utilization estimated by PET-CT imaging in head and neck cancer. European Radiology 2010 Oct; 20:2358–66. DOI: 10.1007/s00330-010-1803-x. Available from: http://link.springer.com/10.1007/s00330-010-1803-x
77. Treutlein C, Stollberg A, Scherl C, Agaimy A, Ellmann S, Iro H, Lell M, Uder M, and Bäuerle T. Diagnostic value of 3D dynamic contrast-enhanced magnetic resonance imaging in lymph node metastases of head and neck tumors: a correlation study with histology. Acta Radiologica Open 2020 Aug; 9:205846012095196. DOI: 10.1177/2058460120951966. Available from: http://journals.sagepub.com/doi/10.1177/2058460120951966
78. Zheng D, Chen Y, Chen Y, Xu L, Chen W, Yao Y, Du Z, Deng X, and Chan Q. Dynamic contrast-enhanced MRI of nasopharyngeal carcinoma: A preliminary study of the correlations between quantitative parameters and clinical stage. Journal of Magnetic Resonance Imaging 2014 Apr; 39:940–8. DOI: 10.1002/jmri.24249. Available from: https://onlinelibrary.wiley.com/doi/10.1002/jmri.24249
79. Cheng J, Shao S, Chen W, and Zheng N. Application of Diffusion Kurtosis Imaging and Dynamic Contrast□Enhanced Magnetic Resonance Imaging in Differentiating Benign and Malignant Head and Neck Lesions. Journal of Magnetic Resonance Imaging 2022 Feb; 55:414–23. DOI: 10.1002/jmri.27885. Available from: https://onlinelibrary.wiley.com/doi/10.1002/jmri.27885
80. Ng SH, Lin CY, Chan SC, Lin YC, Yen TC, Liao CT, Chang JTC, Ko SF, Wang HM, Chang CJ, and Wang JJ. Clinical Utility of Multimodality Imaging with Dynamic Contrast-Enhanced MRI, Diffusion-Weighted MRI, and 18F-FDG PET/CT for the Prediction of Neck Control in Oropharyngeal or Hypopharyngeal Squamous Cell Carcinoma Treated with Chemoradiation. PLoS ONE 2014 Dec; 9. Ed. by Khong PL:e115933. DOI: 10.1371/journal.pone.0115933. Available from: https://journals.plos.org/plosone/article?id=10.1371/journal.pone.0115933
81. Shukla-Dave A, Lee NY, Jansen JF, Thaler HT, Stambuk HE, Fury MG, Patel SG, Moreira AL, Sherman E, Karimi S, Wang Y, Kraus D, Shah JP, Pfister DG, and Koutcher JA. Dynamic Contrast-Enhanced Magnetic Resonance Imaging as a Predictor of Outcome in Head-and-Neck Squamous Cell Carcinoma Patients With Nodal Metastases. International Journal of Radiation Oncology*Biology*Physics 2012 Apr; 82:1837–44. DOI: 10.1016/j.ijrobp.2011.03.006. Available from: https://linkinghub.elsevier.com/retrieve/pii/S0360301611004597
82. Park M, Kim J, Choi YS, Lee SK, Koh YW, Kim SH, and Choi EC. Application of Dynamic Contrast-Enhanced MRI Parameters for Differentiating Squamous Cell Carcinoma and Malignant Lymphoma of the Oropharynx. AJR. American journal of roentgenology 2016 Feb; 206:401–7. DOI: 10.2214/AJR.15.14550. Available from: http://www.ajronline.org/doi/10.2214/AJR.15.14550
83. Asaumi JI, Yanagi Y, Konouchi H, Hisatomi M, Matsuzaki H, and Kishi K. Application of dynamic contrast-enhanced MRI to differentiate malignant lymphoma from squamous cell carcinoma in the head and neck. Oral oncology 2004 Jul; 40:579–84. DOI: 10.1016/j.oraloncology.

2003.12.002. Available from: https://linkinghub.elsevier.com/retrieve/pii/S1368837503002720

84. Lee FKh, King AD, Ma BBY, and Yeung DKw. Dynamic contrast enhancement magnetic resonance imaging (DCE-MRI) for differential diagnosis in head and neck cancers. European Journal of Radiology 2012 Apr; 81:784–8. DOI: 10.1016/j.ejrad.2011.01.089. Available from: https://linkinghub.elsevier.com/retrieve/pii/S0720048X1100129X
85. Vidiri A, Gangemi E, Ruberto E, Pasqualoni R, Sciuto R, Sanguineti G, Farneti A, Benevolo M, Rollo F, Sperati F, Spasiano F, Pellini R, and Marzi S. Correlation between histogram-based DCE-MRI parameters and 18F-FDG PET values in oropharyngeal squamous cell carcinoma: Evaluation in primary tumors and metastatic nodes. PLOS ONE 2020 Mar; 15. Ed. by Bergsland N:e0229611. DOI: 10.1371/journal.pone.0229611. Available from: https://dx.plos.org/10.1371/journal.pone.0229611
86. Liu L, Hu L, Zeng Q, Peng D, Chen Z, Huang C, Liu Z, Wen Q, Zou F, and Yan L. Dynamic contrast-enhanced MRI of nasopharyngeal carcinoma: correlation of quantitative dynamic contrast-enhanced magnetic resonance imaging (DCE-MRI) parameters with hypoxia-inducible factor 1α expression and tumor grade/stage. Annals of Palliative Medicine 2021 Feb; 10:2238–53. DOI: 10.21037/apm-21-303. Available from: https://apm.amegroups.com/article/view/63519
87. Chen Yl, Li R, Chen Tw, Ou J, Zhang Xm, Chen F, Wu L, Jiang Y, Laws M, Shah K, Joseph B, and Hu J. Whole-tumour histogram analysis of pharmacokinetic parameters from dynamic contrast-enhanced MRI in resectable oesophageal squamous cell carcinoma can predict T-stage and regional lymph node metastasis. European Journal of Radiology 2019 Mar; 112:112–20. DOI: 10.1016/j.ejrad.2019.01.012. Available from: https://linkinghub.elsevier.com/retrieve/pii/S0720048X19300129
88. Cintra MB, Ricz H, Mafee MF, and Santos ACd. Magnetic resonance imaging: dynamic contrast enhancement and diffusion-weighted imaging to identify malignant cervical lymph nodes. Radiologia Brasileira 2018 Mar; 51:71–5. DOI: 10.1590/0100-3984.2017.0005. Available from: http://www.scielo.br/scielo.php?script=sci_arttext&pid=S0100-39842018000200071&lng=en&tlng=en
89. Han M, Kim SY, Lee SJ, and Choi JW. The Correlations Between MRI Perfusion, Diffusion Parameters, and 18F-FDG PET Metabolic Parameters in Primary Head-and-Neck Cancer: A Cross-Sectional Analysis in Single Institute. Medicine 2015 Nov; 94:e2141. DOI: 10.1097/MD.0000000000002141. Available from: https://journals.lww.com/00005792-201511240-00064
90. Marzi S, Piludu F, Forina C, Sanguineti G, Covello R, Spriano G, and Vidiri A. Correlation study between intravoxel incoherent motion MRI and dynamic contrast-enhanced MRI in head and neck squamous cell carcinoma: Evaluation in primary tumors and metastatic nodes. Magnetic Resonance Imaging 2017 Apr; 37:1–8. DOI: 10.1016/j.mri.2016.10.004. Available from: https://linkinghub.elsevier.com/retrieve/pii/S0730725X16301515
91. Gawlitza M, Purz S, Kubiessa K, Boehm A, Barthel H, Kluge R, Kahn T, Sabri O, and Stumpp P. In Vivo Correlation of Glucose Metabolism, Cell Density and Microcirculatory Parameters in Patients with Head and Neck Cancer: Initial Results Using Simultaneous PET/MRI. PLOS ONE 2015 Aug; 10. Ed. by Zhang Z:e0134749. DOI: 10.1371/journal.pone.0134749. Available from: https://dx.plos.org/10.1371/journal.pone.0134749
92. Surov A, Leifels L, Meyer HJ, Winter K, Sabri O, and Purz S. Associations Between Histogram Analysis DCE MRI Parameters and Complex 18F-FDG-PET Values in Head and Neck Squamous Cell Carcinoma. Anticancer Research 2018 Mar; 38. DOI: 10.21873/anticanres.12395. Available from: http://ar.iiarjournals.org/content/38/3/1637.abstract
93. Zhang L, Song T, Meng Z, Huang C, Chen X, Lu J, and Xian J. Correlation between apparent diffusion coefficients and metabolic parameters in hypopharyngeal squamous cell carcinoma: A prospective study with integrated PET/MRI. European Journal of Radiology 2020 Aug; 129:109070. DOI: 10.1016/j.ejrad.2020.109070. Available from: https://linkinghub.elsevier.com/retrieve/pii/S0720048X2030259X
94. Cao C, Yang P, Xu Y, Niu T, Hu Q, and Chen X. Feasibility of multiparametric imaging with PET/MR in nasopharyngeal carcinoma: A pilot study. Oral Oncology 2019 Jun; 93:91–5. DOI:

10.1016/j.oraloncology.2019.04.021. Available from: https://linkinghub.elsevier.com/retrieve/pii/S1368837519301332

95. Rasmussen JH, Nørgaard M, Hansen AE, Vogelius IR, Aznar MC, Johannesen HH, Costa J, Engberg AM, Kjær A, Specht L, and Fischer BM. Feasibility of Multiparametric Imaging with PET/MR in Head and Neck Squamous Cell Carcinoma. Journal of Nuclear Medicine 2017 Jan; 58:69–74. DOI: 10.2967/jnumed.116.180091. Available from: https://jnm.snmjournals.org/content/58/1/69
96. Min M, Lee MT, Lin P, Holloway L, Wijesekera D, Gooneratne D, Rai R, Xuan W, Fowler A, Forstner D, and Liney G. Assessment of serial multi-parametric functional MRI (diffusion-weighted imaging and R 2 *) with 18 F-FDG-PET in patients with head and neck cancer treated with radiation therapy. The British Journal of Radiology 2016 Feb; 89:20150530. DOI: 10.1259/bjr.20150530. Available from: http://www.birpublications.org/doi/10.1259/bjr.20150530
97. Choi SH, Paeng JC, Sohn CH, Pagsisihan JR, Kim YJ, Kim KG, Jang JY, Yun TJ, Kim JH, Han MH, and Chang KH. Correlation of 18 F-FDG Uptake with Apparent Diffusion Coefficient Ratio Measured on Standard and High b Value Diffusion MRI in Head and Neck Cancer. Journal of Nuclear Medicine 2011 Jul; 52:1056–62. DOI: 10.2967/jnumed.111.089334. Available from: https://jnm.snmjournals.org/content/52/7/1056
98. Leibfarth S, Simoncic U, Mönnich D, Welz S, Schmidt H, Schwenzer N, Zips D, and Thorwarth D. Analysis of pairwise correlations in multi-parametric PET/MR data for biological tumor characterization and treatment individualization strategies. European Journal of Nuclear Medicine and Molecular Imaging 2016 Jul; 43:1199–208. DOI: 10.1007/S00259-016-3307-7/FIGURES/5. Available from: https://link.springer.com/article/10.1007/s00259-016-3307-7
99. Zwirner K, Thorwarth D, Winter RM, Welz S, Weiss J, Schwenzer NF, Schmidt H, Fougère C la, Nikolaou K, Zips D, and Gatidis S. Voxel-wise correlation of functional imaging parameters in HNSCC patients receiving PET/MRI in an irradiation setup. Strahlentherapie und Onkologie 2018 Aug; 194:719–26. DOI: 10.1007/s00066-018-1292-4. Available from: http://link.springer.com/10.1007/s00066-018-1292-4
100. Olin A, Krogager L, Rasmussen JH, Andersen FL, Specht L, Beyer T, Kjaer A, Fischer BM, and Hansen AE. Preparing data for multiparametric PET/MR imaging: Influence of PET point spread function modelling and EPI distortion correction on the spatial correlation of [18F]FDG-PET and diffusion-weighted MRI in head and neck cancer. Physica Medica 2019 May; 61:1–7. DOI: 10.1016/J.EJMP.2019.04.006
101. Kim Yi, Cheon GJ, Kang SY, Paeng JC, Kang KW, Lee DS, and Chung JK. Prognostic value of simultaneous 18F-FDG PET/MRI using a combination of metabolo-volumetric parameters and apparent diffusion coefficient in treated head and neck cancer. EJNMMI Research 2018 Dec; 8:2. DOI: 10.1186/s13550-018-0357-9. Available from: https://ejnmmires.springeropen.com/articles/10.1186/s13550-018-0357-9
102. Cheng Y, Bai L, Shang J, Tang Y, Ling X, Guo B, Gong J, Wang L, and Xu H. Preliminary clinical results for PET/MR compared with PET/CT in patients with nasopharyngeal carcinoma. Oncology Reports 2019 Oct; 43:177–87. DOI: 10.3892/or.2019.7392. Available from: https://www.spandidos-publications.com/10.3892/or.2019.7392

B

Supplementary Tables and Figures

Table B.1. Quantitative parameter correlations with pathology.

	Normal	**N=10**		**Metastatic**	**N=3**
Parameter	Median	Range	Median	Range	P-value ‡
Short axis	6.20	5.23 - 7.15	27.00	18.70 - 29.10	**0.007***
DWI-IVIM D_{median}	6.91×10^{-4}	5.30×10^{-4} - 8.44×10^{-4}	8.72×10^{-4}	6.64×10^{-4} - 1.05×10^{-3}	0.161
DWI-IVIM D_{mean}	7.10×10^{-4}	5.28×10^{-4} - 7.96×10^{-4}	9.37×10^{-4}	7.61×10^{-4} - 1.18×10^{-3}	0.077
DWI-IVIM D_{max}	1.30×10^{-3}	1.20×10^{-3} - 2.00×10^{-3}	1.38×10^{-2}	3.80×10^{-3} - 2.00×10^{-2}	**0.028***
DWI-IVIM D_{min}	4.72×10^{-5}	2.24×10^{-5} - 1.62×10^{-4}	1.42×10^{-5}	-6.51×10^{-19} - 3.88×10^{-5}	0.161
DWI-IVIM $D_{skewness}$	1.42×10^{-1}	-5.38×10^{-1} - 7.48×10^{-1}	8.26	8.21×10^{-1} - 1.17×10^{1}	0.077
DWI-IVIM $D_{kurtosis}$	2.93×10^{-1}	-6.47×10^{-1} - 9.35×10^{-1}	1.73×10^{2}	2.33×10^{-1} - 3.44×10^{2}	0.161
DWI-IVIM D^*_{median}	1.87×10^{-2}	9.10×10^{-3} - 2.35×10^{-2}	1.33×10^{-2}	8.70×10^{-3} - 1.00×10^{-2}	0.287
DWI-IVIM D^*_{mean}	2.20×10^{-2}	1.91×10^{-2} - 4.43×10^{-2}	2.23×10^{-2}	2.10×10^{-2} - 2.00×10^{-2}	0.937
DWI-IVIM D^*_{max}	4.77×10^{-1}	2.65×10^{-1} - 5.44×10^{-1}	6.21×10^{-1}	5.62×10^{-1} - 8.00×10^{-1}	0.077
DWI-IVIM D^*_{min}	1.20×10^{-3}	3.91×10^{-4} - 2.10×10^{-3}	8.45×10^{-4}	0.00 - 1.04×10^{-3}	0.287
DWI-IVIM $D^*_{skewness}$	4.85	3.42 - 6.10	7.72	6.88 - 8.83	**0.049***
DWI-IVIM $D^*_{kurtosis}$	2.41×10^{1}	1.24×10^{1} - 4.38×10^{1}	9.46×10^{1}	8.20×10^{1} - 9.98×10^{1}	**0.049***
DWI-IVIM f_{median}	1.74×10^{-1}	8.87×10^{-2} - 2.52×10^{-1}	1.28×10^{-1}	1.08×10^{-1} - 2.10×10^{-1}	0.692
DWI-IVIM f_{mean}	2.14×10^{-1}	1.39×10^{-1} - 2.50×10^{-1}	1.77×10^{-1}	1.36×10^{-1} - 2.30×10^{-1}	0.811
DWI-IVIM f_{max}	5.87×10^{-1}	5.32×10^{-1} - 6.68×10^{-1}	7.00×10^{-1}	6.84×10^{-1} - 1.00	0.077
DWI-IVIM f_{min}	2.14×10^{-2}	1.18×10^{-2} - 2.99×10^{-2}	4.60×10^{-3}	-2.78×10^{-17} - 2.00×10^{-2}	0.112
DWI-IVIM $f_{skewness}$	9.15×10^{-1}	4.57×10^{-2} - 1.27	1.18	4.62×10^{-1} - 2.43	0.469
DWI-IVIM $f_{kurtosis}$	1.29×10^{-2}	-9.92×10^{-1} - 7.66×10^{-1}	5.44×10^{-1}	-7.40×10^{-1} - 8.68	0.371
^{18}F-FDG SUV_{median}	2.35	1.62 - 3.96	4.99	4.08 - 7.91	**0.028***
^{18}F-FDG SUV_{mean}	2.62	1.91 - 4.46	5.82	4.70 - 8.94	**0.007***
^{18}F-FDG SUV_{max}	4.61	3.05 - 9.64	1.86×10^{1}	1.78×10^{1} - 3.01×10^{1}	**0.007***
^{18}F-FDG SUV_{min}	9.17×10^{-1}	7.11×10^{-1} - 1.43	6.55×10^{-1}	1.91×10^{-1} - 8.40×10^{-1}	0.161
^{18}F-FDG $SUV_{skewness}$	5.99×10^{-1}	1.80×10^{-1} - 9.83×10^{-1}	7.54×10^{-1}	7.51×10^{-1} - 1.02	0.371
^{18}F-FDG $SUV_{kurtosis}$	-5.80×10^{-1}	-1.20 - -3.55×10^{-2}	2.29×10^{-2}	-8.10×10^{-2} - 2.29×10^{-2}	0.161
DCE-MRI K^{trans}_{median}	2.03×10^{-1}	1.74×10^{-1} - 7.93×10^{-1}	7.14×10^{-2}	4.61×10^{-2} - 1.30×10^{-1}	**0.014***
DCE-MRI K^{trans}_{mean}	2.37×10^{-1}	1.89×10^{-1} - 7.68×10^{-1}	9.20×10^{-2}	6.78×10^{-2} - 1.50×10^{-1}	**0.028***
DCE-MRI K^{trans}_{max}	1.00	5.24×10^{-1} - 1.00	9.97×10^{-1}	4.82×10^{-1} - 1.00	0.573
DCE-MRI K^{trans}_{min}	3.00×10^{-2}	1.59×10^{-2} - 1.09×10^{-1}	2.22×10^{-14}	0.00 - 1.00×10^{-2}	**0.014***
DCE-MRI $K^{trans}_{skewness}$	4.90×10^{-1}	-1.24 - 1.34	1.98	9.29×10^{-1} - 3.34	0.077
DCE-MRI $K^{trans}_{kurtosis}$	1.38	-7.42×10^{-1} - 1.81×10^{1}	8.59	3.14×10^{-1} - 2.69×10^{1}	0.287
DCE-MRI $K_{ep-median}$	9.27×10^{-1}	7.76×10^{-1} - 1.12	6.68×10^{-1}	6.24×10^{-1} - 9.80×10^{-1}	0.371
DCE-MRI $K_{ep-mean}$	9.81×10^{-1}	8.04×10^{-1} - 1.10	8.56×10^{-1}	8.52×10^{-1} - 9.80×10^{-1}	0.573
DCE-MRI K_{ep-max}	1.99	1.61 - 2.00	2.00	2.00 - 2.00	**0.014***
DCE-MRI K_{ep-min}	4.57×10^{-8}	5.39×10^{-10} - 1.69×10^{-6}	2.33×10^{-14}	0.00 - 2.57×10^{-8}	0.077
DCE-MRI $K_{ep-skewness}$	-1.74×10^{-1}	-4.85×10^{-1} - 2.79×10^{-1}	4.00×10^{-1}	1.88×10^{-1} - 8.60×10^{-1}	**0.049***
DCE-MRI $K_{ep-kurtosis}$	-3.91×10^{-1}	-1.23 - -1.81×10^{-1}	-3.49×10^{-1}	-1.39 - 0.00	1.000
DCE-MRI $V_{p-median}$	1.41×10^{-2}	1.90×10^{-3} - 1.02×10^{-1}	4.40×10^{-3}	2.30×10^{-3} - 1.00×10^{-2}	0.469
DCE-MRI V_{p-mean}	1.93×10^{-2}	6.90×10^{-3} - 9.16×10^{-2}	6.00×10^{-3}	3.80×10^{-3} - 1.00×10^{-2}	0.217
DCE-MRI V_{p-max}	2.00×10^{-1}	7.11×10^{-2} - 2.00×10^{-1}	9.48×10^{-2}	3.94×10^{-2} - 2.00×10^{-1}	0.287
DCE-MRI V_{p-min}	2.18×10^{-10}	7.30×10^{-13} - 7.34×10^{-8}	0.00	0.00 - 9.53×10^{-11}	0.112
DCE-MRI $V_{p-skewness}$	1.36	4.90×10^{-1} - 5.05	2.68	1.94 - 5.21	0.371
DCE-MRI $V_{p-kurtosis}$	2.65	1.10×10^{-1} - 4.07×10^{1}	1.44×10^{1}	6.08 - 3.94×10^{1}	0.469

‡Mann-Whitney U test